Spatiotemporal Chaos in Rayleigh-Bénard Convection

Thesis by

Keng-Hwee Chiam

In Partial Fulfillment of the Requirements

for the Degree of

Doctor of Philosophy

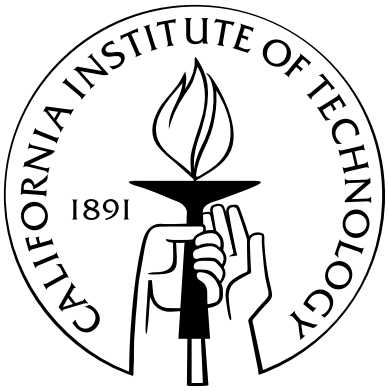

California Institute of Technology

Pasadena, California

2004

(Defended August 1, 2003)

Acknowledgements

I would like to take this opportunity to thank my advisor, Prof. Mike Cross, for his guidance and support throughout my graduate years. I have benefited immensely from his sound intuition and insightful comments. I would also like to thank Prof. Henry Greenside, Dr. Paul Fischer, and Dr. Mark Paul for the opportunity to collaborate with them. I have enjoyed working with and learning from them. I would also like to thank members of my thesis committee, Profs. Tony Leonard, Ken Libbrecht, and Dan Meiron, for answering my occasional questions and for showing interest in my work. I would also like to thank Michael Louie and Janet Scheel for useful discussions. Last but not least, I would like to thank my wife and parents for their love and patience.

Abstract

Spatiotemporal chaos, or disorder in space and chaos in time, is studied in direct numerical simulations of Rayleigh-Bénard convection. In particular, the following results pertaining to spiral defect chaos are discussed.

First, in the absence of the mean flow, spiral defect chaos is found to collapse to a stationary pattern comprising textures of stripes with angular bends. The quenched patterns are characterized by mean wave numbers that approach those uniquely selected by focus-type singularities, which, in the absence of the mean flow, lie at the zig zag instability boundary. In addition, mean flow is shown to contribute to the phenomenon of rolls terminating perpendicularly into lateral walls. In the absence of the mean flow, rolls begin to terminate into lateral walls at an oblique angle. This obliqueness increases with the Rayleigh number.

Second, the transport of passive tracers in the presence of advection by spiral defect chaos is found to be characterized by normal diffusion. The enhancement in the tracer diffusivity follows two regimes. When the molecular diffusivity of the tracer concentration is small, the enhancement is proportional to the Péclet number. When the molecular diffusivity is large, the enhancement is proportional to the square root of the Péclet number. This difference is explained in terms of the dependence of the transport on the local wave numbers. It is found that tracer concentrations with small molecular diffusivity experience enhanced longitudinal diffusion and suppressed lateral diffusion at regions of the flow occupied by defects.

Third, perturbations in spiral defect chaos are found to propagate in a localized manner. In particular, they nucleate around the defect structures in the flow. In addition, an oscillatory instability at the spiral core is discovered. Finally, the propa-

gation in pre-chaotic stripe textures is explained in terms of the diffusion of the phase variable of the stripe state.

Contents

List of Figures

Chapter 1

Introduction

1.1 Motivation

The study of chaos in systems with a few degrees of freedom is already a mature subject. For example, the chaotic behavior observed in low-dimensional dynamical systems such as the Lorenz model can be completely understood in terms of their spectra of positive Lyapunov exponents or the fractal properties of their phase space attractors [60, 87]. However, much less is known about the chaos that is observed in spatially-extended and continuous media that have many (possibly an infinite number of) degrees of freedom. Examples may be found in many fluid, chemical, and biological systems, such as the oceans and the atmosphere [62], the Belousov-Zhabotinsky reaction system [77], the chlorite-iodide-malonic acid reaction-diffusion system and its variants [78], morphogenesis in embryos of fruit flies [97], neuronal activities in brains of humans [20] and animals [67], etc.

Although the mechanisms for the generation of disorder may be specific to each individual system, universal features may exist. One such universal feature that will be the focus of this dissertation is the occurrence of spatiotemporal chaos [28, 39, 43]. It refers to the system exhibiting chaos in its temporal dynamics in localized regions, and that these localized regions then mutually interact with one another to generate spatial disorder. In other words, the system can be said to be exhibiting disorder in both space and time, and acquires a large attractor dimension (possibly diverging as the system size diverges).

In principle, one can still apply the techniques used for studying low-dimensional chaos to spatiotemporal chaos. For example, one can reconstruct from time series measurements the attractor in phase space and analyze the properties of this high-dimensional attractor. However, this approach becomes impractical as the size of the system becomes very large. Consequently, new descriptions and techniques are needed. However, because these are not yet forthcoming, many questions about spatiotemporal chaos remain unanswered. How does spatiotemporal chaos start to appear in a continuous system with infinitely many degrees of freedom? How does spatiotemporal chaos develop as parameters of the system are changed? What is the nature of the transitions between different states (both from a stationary state to spatiotemporal chaos and between different kinds of spatiotemporal chaos)? What are the most appropriate statistical measures to characterize spatiotemporal chaos?

This dissertation describes the research done to answer some aspects of these questions pertaining to spatiotemporal chaos. However, rather than study each system exhibiting spatiotemporal chaos individually, a simple idealized model that captures the essential physics is studied. In this dissertation, this model is a fluid that is being thermally driven far from equilibrium to give rise to convection [10]. In certain parameter regimes, the fluid gives rise to a kind of spatiotemporal chaos called spiral defect chaos [56] that will be the focus of this dissertation.

Although experiments have traditionally played a significant role in exploring the properties of spatiotemporal chaos, many of the observed phenomena are difficult to analyze theoretically [28]. As a result, there is a need for the use of direct numerical simulations of these experiments to make quantitative comparisons between theory and experiment. This dissertation focuses on making such quantitative comparisons. In particular, simulations are used to explore parameter regimes that are not easily attained by experiment, and to calculate quantities that are difficult to deduce from experimental data. Finally, it should be emphasized that this dissertation does not seek to use the simulations to reproduce previous experimental results, but to provide new avenues of exploration that are complementary to the experimental ones, and to stimulate further experimental work in novel parameter ranges.

1.2 Overview

In the remaining part of this chapter, the system studied in this dissertation, buoyancy-driven convection, is introduced. In Chap. 2, details of the algorithms used in this dissertation for the direct numerical simulations of buoyancy-driven convection are described. The next three chapters discuss the investigations of three separate problems on spiral defect chaos. In Chap. 3, the question of how the appearance of spiral defect chaos can be traced to the presence of nonlocal mean flow modes is addressed [21]. In Chap. 4, the transport of passive neutrally-buoyant tracers in spiral defect chaotic flows is described. In Chap. 5, the spatial propagation of perturbations in spiral defect chaos is described. Finally, in Chap. 6, conclusions are presented.

1.3 Rayleigh-Bénard convection

The model used in this dissertation is buoyancy-driven convection, also more commonly known as Rayleigh-Bénard convection [10, 27, 38, 52]. It has played a vital role in developing ideas in low-dimensional chaos [1] and spatiotemporal chaos [2, 9], and is generally regarded as the canonical example of a continuous system capable of generating and sustaining spatiotemporal chaos. It has the advantages that the underlying equations [see Eqs. (1.5)–(1.7) below] are well understood, and that there is a close connection between theory and experiment.

In a Rayleigh-Bénard convection experiment, illustrated in Fig. 1.1, a fluid layer is confined between two horizontal plates, and is thermally driven far from equilibrium by maintaining the bottom plate at a temperature that is higher than that of the top plate.

The dynamics of the fluid layer is then governed to a good approximation by the Boussinesq equations. They are the combination of the incompressible Navier-Stokes and heat equations in three dimensions, with the further assumptions that density

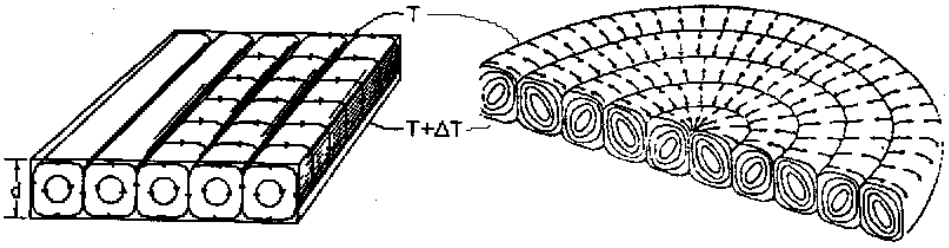

Figure 1.1: Schematic illustrations of Rayleigh-Bénard convection. A fluid layer of depth d is confined between two horizontal plates. The bottom plate is maintained at a temperature ΔT higher than that of the top plate. The left panel illustrates the formation of ideal straight and parallel convection rolls in a rectangular cell. The right panel illustrates the formation of ideal axisymmetric convection rolls in a cylindrical cell. The arrows denote fluid streamlines.

variations are proportional to temperature variations

$$\rho = \tilde{\rho}\left[1 - \alpha(T - \tilde{T})\right] \tag{1.1}$$

with $\tilde{\rho}$ and $\tilde{T}$ some reference values and α the isobaric thermal expansion coefficient, and that this density variation appears only in the buoyancy force. The equations read:

$$\begin{aligned}
(\partial_t + \mathbf{u}\bullet\nabla)\,\mathbf{u}(x,y,z,t) &= -\nabla\left(\frac{p}{\tilde{\rho}}\right) + \nu\nabla^2\mathbf{u} + g\alpha(T-\tilde{T})\hat{z}, &(1.2)\\
(\partial_t + \mathbf{u}\bullet\nabla)\,T(x,y,z,t) &= \kappa\nabla^2 T, &(1.3)\\
\nabla\bullet\mathbf{u} &= 0. &(1.4)
\end{aligned}$$

The field $\mathbf{u}(x,y,z,t)$ is the velocity field at point (x,y,z) and time t, while p and T are the pressure and temperature fields, respectively. The variables x and y denote the horizontal coordinates, while the variable z denotes the vertical coordinate, with the unit vector $\hat{z}$ pointing in the direction opposite to the gravitational acceleration g. The parameters ν and κ are the kinematic viscosity and the thermal diffusivity of the fluid, respectively. These parameters are assumed to be independent of the temperature of the fluid. These equations can also be expressed in dimensionless

form:

$$\begin{aligned} \sigma^{-1}\left(\partial_t + \mathbf{u}\bullet\nabla\right)\mathbf{u}(x,y,z,t) &= -\nabla p + \nabla^2\mathbf{u} + RT\hat{z}, & (1.5)\\ \left(\partial_t + \mathbf{u}\bullet\nabla\right)T(x,y,z,t) &= \nabla^2 T, & (1.6)\\ \nabla\bullet\mathbf{u} &= 0. & (1.7) \end{aligned}$$

Space is now measured in units of the cell depth d, and time is measured in units of the vertical diffusion time d^2/κ. Dedimensionalization also reduces the number of parameters in the equations to just two. They are the Rayleigh number R, which can be thought of as the dimensionless temperature difference ΔT across the top and bottom plates,

$$R = \frac{\alpha g d^3}{\nu\kappa}\Delta T, \tag{1.8}$$

and the Prandtl number σ, which is the ratio of the fluid's thermal to viscous diffusivities,

$$\sigma = \frac{\nu}{\kappa}. \tag{1.9}$$

The reduced Rayleigh number,

$$\epsilon = \frac{R - R_c}{R_c}, \tag{1.10}$$

where $R_c \approx 1708$ is the critical Rayleigh number at the onset of convection in an infinite domain [27], will also be frequently used.

In this dissertation, the material walls of the cell are assumed to be no-slip, so that the velocity field satisfies

$$\mathbf{u} = \mathbf{0}, \quad \text{on all material walls.} \tag{1.11}$$

The temperature field is assumed to be constant on the top and bottom plates:

$$T\left(x, y, z = \mp\frac{1}{2}, t\right) = \pm\frac{1}{2}, \tag{1.12}$$

and the lateral walls are assumed to be perfectly insulating, so that

$$\widehat{n} \bullet \nabla T = 0, \quad \text{on lateral walls,} \tag{1.13}$$

where $\widehat{n}$ is the unit vector perpendicular to the lateral walls at a given point. The pressure field p has no associated boundary condition since it does not satisfy a dynamical equation.

The influence of the lateral walls on the dynamics is determined by the dimensionless aspect ratio Γ, defined to be the half-width-to-depth ratio of the cell if it is rectangular and the radius-to-depth ratio if it is cylindrical. For example, for a rectangular geometry, the fluid occupies the region defined by

$$-\Gamma_x \le x \le \Gamma_x, \qquad -\Gamma_y \le y \le \Gamma_y, \qquad -\frac{1}{2} \le z \le \frac{1}{2}, \tag{1.14}$$

where Γ_x and Γ_y are the aspect ratios in the x and y directions, respectively.

If the Rayleigh number is small, $R < R_c = 1708$, the fluid remains motionless and heat is transported only via conduction from the bottom plate to the top plate. However, as the Rayleigh number is increased, the fluid undergoes an instability to a state in which there is motion driven by the buoyancy forces. When the Rayleigh number is above but near this convective threshold, the fluid spontaneously organizes itself into convection rolls, each with a diameter that is close to the depth of the cell. Images of the temperature field at mid-plane reveal patches of locally parallel rolls. Examples of these laminar planforms are shown in Fig. 1.2. When the Rayleigh number is increased, the fluid undergoes other instabilities [15] that may result in the convection rolls developing a simple or a chaotic time dependence. Finally, when the Rayleigh number is increased further, the convection rolls may collectively become disordered in space and in time, and exhibit spatiotemporal chaos.

In particular, spiral defect chaos is observed for the Rayleigh number $R \gtrsim 3000$, the Prandtl number $\sigma \sim 1$, and the aspect ratio $\Gamma \gtrsim 20$. It is characterized by a disordered collection of spirals of both the left- and right-handed kinds that rotate in the counter-

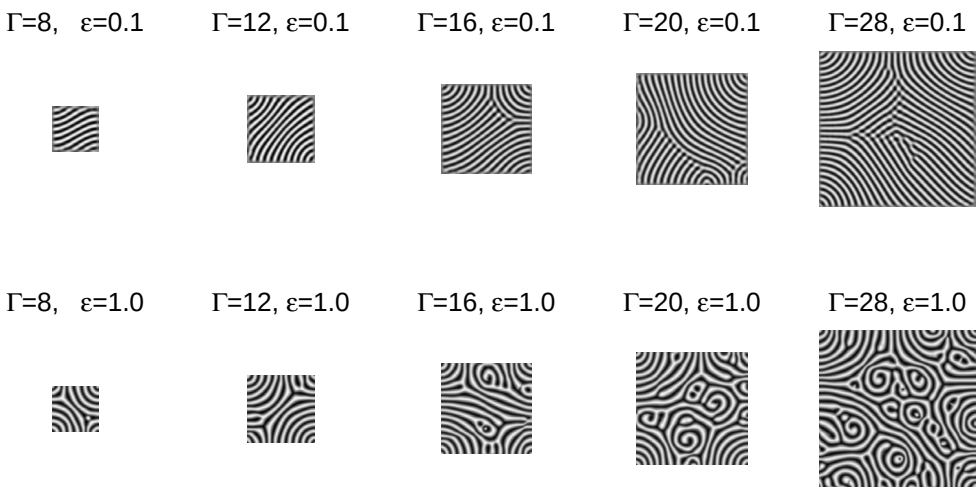

Figure 1.2: Examples of convection planforms, including spiral defect chaos, observed in direct numerical simulations of Rayleigh-Bénard convection. The mid-plane temperature field $T(x, y, z = 0)$ is plotted at time $t = 500$ for the reduced Rayleigh number $\epsilon = 0.1$ (top row) and $\epsilon = 1.0$ (bottom row), the Prandtl number $\sigma = 1$, and the aspect ratio Γ ranging from 16–56. Dark regions correspond to cold sinking fluid, light regions to hot rising fluid. Spiral defect chaos appears in the rightmost two planforms on the bottom row.

clockwise and clockwise senses, respectively. The spirals nucleate and annihilate in seemingly random fashions. In addition to the spirals, dynamical defects such as grain boundaries and dislocations are also present. Examples of spiral defect chaos are shown in the rightmost two planforms, labelled $\Gamma = 20, \epsilon = 1.0$ and $\Gamma = 28, \epsilon = 1.0$, on the bottom row of Fig. 1.2. A time sequence showing the evolution of a spiral defect chaos planform is also shown in Fig. 1.3.

It is useful to characterize the convection planforms, both laminar and spiral defect chaotic, by the distribution $P(k)$ of wave numbers k. The wave number measures the inverse width of the convection rolls, and can be approximated by a local method [33], in which the wave number $k(x, y)$ at the location (x, y) is computed using

$$k(x, y) \approx \left| \frac{-\nabla^2 T(x, y)}{T(x, y)} \right|^{1/2}, \tag{1.15}$$

where $T(x, y)$ is the temperature field at location (x, y) and the mid-plane $z = 0$.

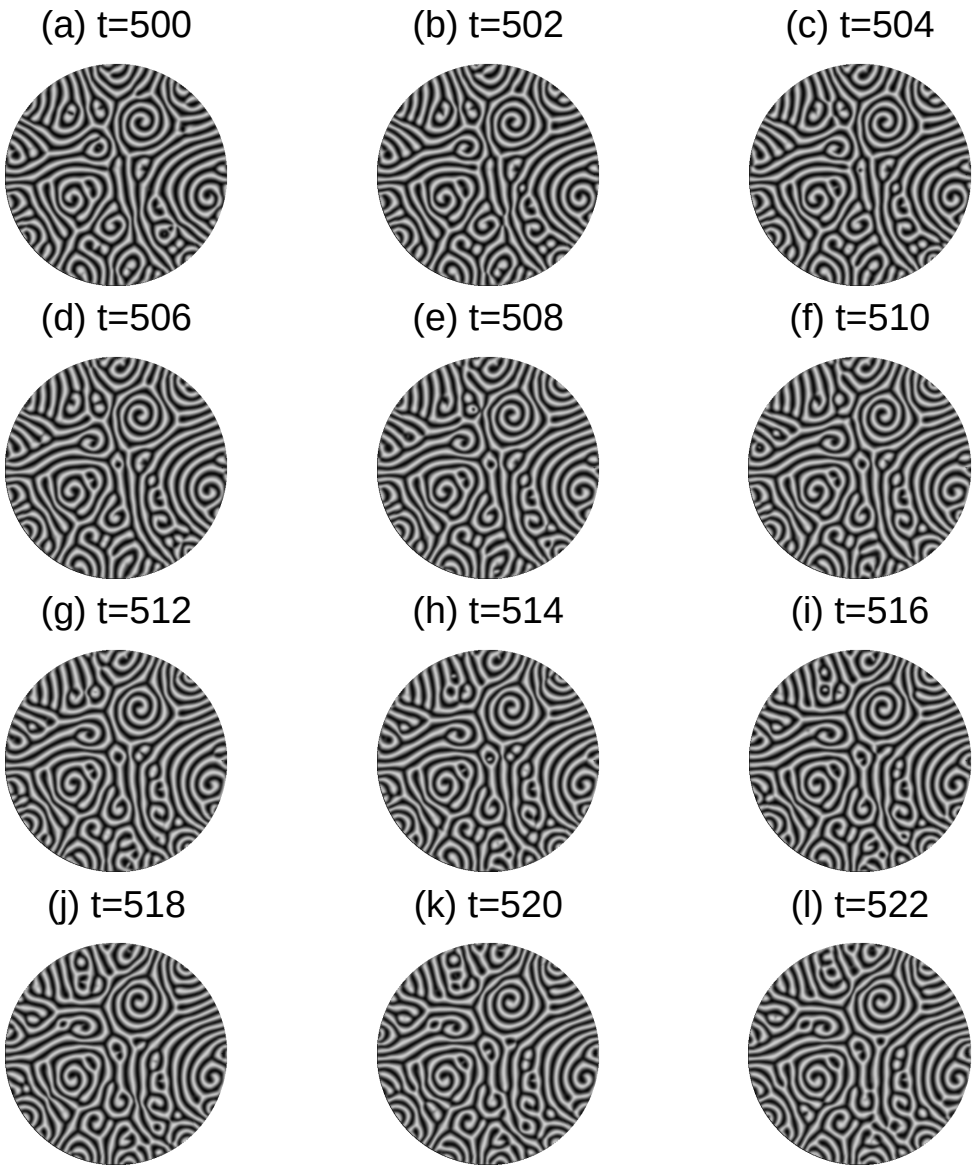

Figure 1.3: Time sequence of the evolution of a spiral defect chaos planform in a cylindrical cell of aspect ratio $\Gamma = 30$ at the Rayleigh number $R = 3500$ and the Prandtl number $\sigma = 1$ for a period of 22 time units. Spiral defect chaos is characterized by a disordered collection of spirals of both the left- and right-handed kinds that rotate in the counter-clockwise and clockwise senses, respectively. The spirals nucleate and annihilate in seemingly random fashions. In addition to the spirals, dynamical defects such as grain boundaries and dislocations are also present.

(For smaller aspect ratios $\Gamma \lesssim 20$, this method produces better statistics than global Fourier transform methods that were used in previous experiments [44, 56, 57].)

The mean of this wave number distribution, $\langle k \rangle$ can then be computed as a function of the Rayleigh and Prandtl numbers, thus defining a "phase diagram" for the convection planforms. An example for several different values of the reduced Rayleigh number ϵ and the Prandtl number $\sigma = 1$ is shown in Fig. 1.4. This phase diagram allows one to deduce certain trends about the convection planforms. First, it shows that the variation of $\langle k \rangle$ with the reduced Rayleigh number ϵ is nearly independent of the aspect ratio $\Gamma \equiv \Gamma_x = \Gamma_y$ of a rectangular cell. Second, it shows that the mean wave number $\langle k \rangle$ decreases approximately linearly with increasing Rayleigh number, up to about $\epsilon \approx 1$. At this point, there is a change in the trend, with the mean wave number $\langle k \rangle$ becoming essentially independent of the Rayleigh number. In the larger aspect ratios, these points correspond to the convection planforms exhibiting fully-developed spiral defect chaos. (In the smaller aspect ratio cells, the convection planforms are chaotic but do not exhibit spiral defect chaos.) Experimentally, this independence is not observed. For example, the mean wave number calculated in a previous experiment [56, 57] performed in a cylindrical cell with $\Gamma = 40$ and $\sigma = 0.98$ decreases with increasing Rayleigh number, up until $\epsilon \approx 5$; c.f. Fig. 12 of Ref. [44]. Presumably, the smaller aspect ratios used in the simulations mean that their wave numbers are affected by finite size effects.

In addition to the mean wave number, a correlation length, ξ, can also be defined from the inverse width of the wave number distribution $P(k)$. It is a measure of the average length scale of correlated regions in the pattern, and generally speaking, quantifies the average amount of spatial disorder in the convection planform. Values of the correlation length as a function of the reduced Rayleigh number ϵ are plotted in Fig. 1.5. It shows that the correlation length ξ is independent of the aspect ratio and obeys approximately a power law dependence

$$\xi \propto \epsilon^{-1/2} \tag{1.16}$$

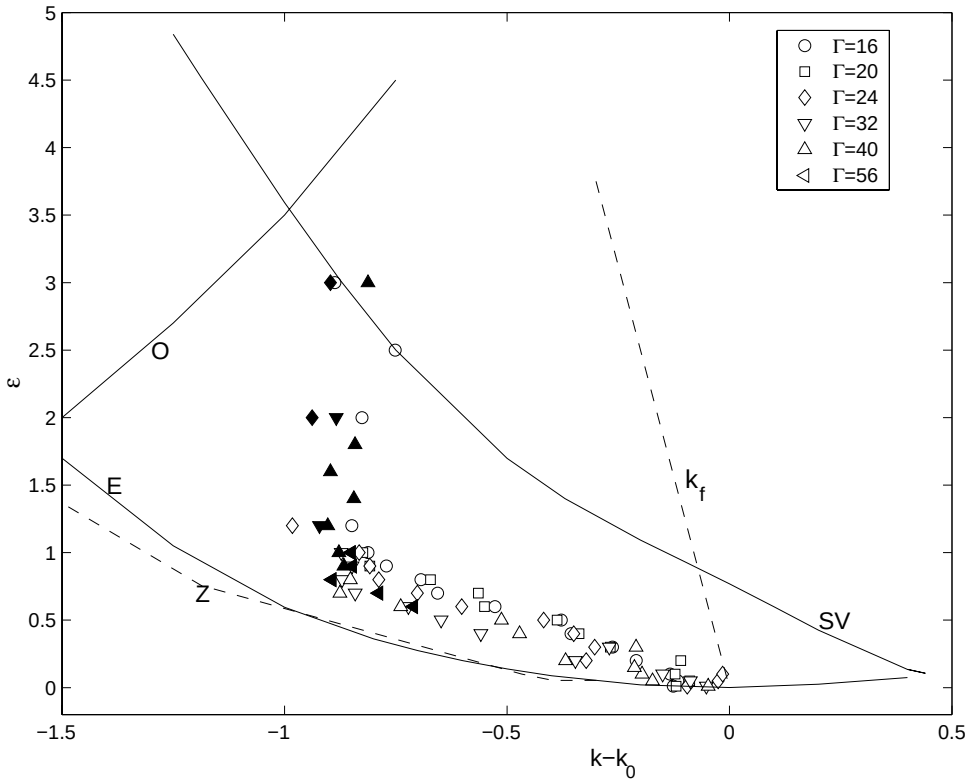

Figure 1.4: The reduced Rayleigh number ϵ vs. the mean wave number $\langle k \rangle - k_c$, with $k_c = 3.117$ the critical wave number at the onset of convection in an infinite domain [27]. Solid symbols denote convection planforms where spiral defect chaos is observed. Also shown are the instability boundaries [15] which limit the range for an ideal state of straight and parallel rolls in an infinite domain. The various symbols denote the various instability mechanisms: Eckhaus(E); zig zag(Z); skew varicose (SV); oscillatory (O). The unique wave number that is selected in axisymmetric rolls, k_f, is also shown (see Sect. 3.3.4).

which is consistent with that predicted by the amplitude equation theory [27] (although the range of Rayleigh numbers in the plot is much larger than the range over which this theory might be expected to hold). A similar trend has also been noticed in cylindrical geometry experiments [44, 57], although an experiment in a rectangular cell [16] found a divergence at a nonzero value of ϵ.

The wave number distribution, the mean wave number, and the correlation length will be used extensively to quantify the various properties of spiral defect chaos in later chapters.

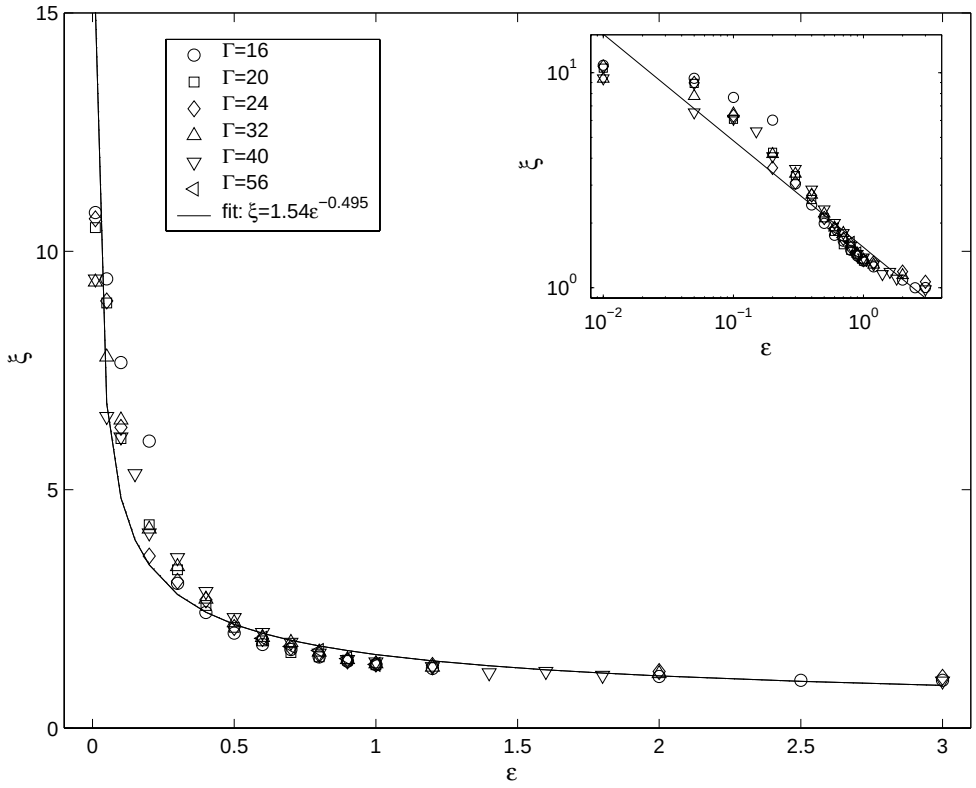

Figure 1.5: The correlation length ξ, defined as the inverse width of the wave number probability distribution $P(k)$, is plotted as a function of the reduced Rayleigh number ϵ. The inset shows the same information but on a log-log scale. The straight line in the inset has a slope 1/2 as would be predicted by amplitude equation theory that is valid near threshold.

Finally, instead of the Boussinesq equations, Eqs. (1.5)–(1.7), models of Rayleigh-Bénard convection have also been used in the study of spatiotemporal chaos. One such example is the Swift-Hohenberg model equation [90] and its generalizations. These models are computationally less expensive to integrate than the Boussinesq equations, and are useful when qualitative, and not quantitative, comparisons between theory and experiment are needed quickly. However, recent advances in parallel computers and data storage have allowed for the development of direct numerical simulations that allow for the efficient integration of the Boussinesq equations with realistic boundary conditions and without any approximations to the physics. Two of these algorithms will be discussed in Chap. 2. The availability of these direct numeri-

cal simulations have largely obviated the need for model equations. Nevertheless, the model equations are briefly discussed here for completeness.

The Swift-Hohenberg model equation [50, 90] describes the evolution of a real scalar field $\psi(x, y, t)$ that is supposed to mimic the convection planforms [such as the temperature field $T(x, y)$ at the mid-plane $z = 0$],

$$\partial_t \psi(x, y, t) = \epsilon\psi - (\nabla^2 + 1)^2\psi - \psi^3. \tag{1.17}$$

The stress parameter ϵ is supposed to mimic the role of the reduced Rayleigh number defined in Eq. (1.10). Various other nonlinear terms can also be chosen in lieu of the cubic ψ^3 term. For example, the term $3(\nabla\psi)^2\nabla^2\psi$ has been used [41] because it gives a better representation of the stability of the stripe state as the wave vector and stress parameter are varied. The behavior of the scalar field $\psi(x, y, t)$ very often reproduces the convection planforms observed in experiments. However, there are several limitations to the Swift-Hohenberg modeling. First, the Swift-Hohenberg model equation describes the spatiotemporal behavior of a field in two dimensions, whereas convection is a three-dimensional phenomenon. Second, the long-time dynamics of the Swift-Hohenberg equation may not correspond to that of the Boussinesq equations of convection. In particular, Swift-Hohenberg models exhibit spiral defect chaos as a transient behavior, whereas in experiments, spiral defect chaos is known to persist for much longer times [76]. Third, the small-scale structure of the depth-averaged vorticity potentials at the cores of the spirals, which might be crucial for the persistence of spiral defect chaos, are not perfectly captured in the Swift-Hohenberg equation [10]. While some of these limitations may be overcome by using more elaborate modeling, this approach will not be followed in this dissertation. Instead, in the next chapter, direct numerical simulations of the Boussinesq equations will be discussed.

Chapter 2

Direct numerical simulations

2.1 Introduction

This dissertation makes extensive use of two previously developed packages of direct numerical simulations of the Boussinesq equations, Eqs. (1.5)–(1.7), in realistic boundaries conditions, Eqs. (1.11)–(1.13). However, because details of the algorithms are already available in the literature, they will not be presented here. Instead, the goal of this chapter is to briefly describe these two solvers and their relevance to the problems introduced in Chaps. 3–5.

The main characteristic of these two solvers that is relevant to this dissertation is their ability to solve for large aspect ratios necessary for the study of spatiotemporal chaos. The first solver, `boxcode`, is a serial second-order accurate finite difference algorithm that uses a rectangular colocated mesh. Consequently, it can only simulate rectangular cells but is highly efficient in doing so, as long as the aspect ratio is kept moderate. The second solver, `nek5000`, is a parallel spectral element algorithm that is second- or third-order accurate in time and exponentially convergent in space and is able to treat complex geometries (including both rectangular and cylindrical cells).

The regime of large aspect ratio Γ poses significant computational challenges. Many numerical degrees of freedom in the form of basis functions or mesh points are needed to represent the spatial structure of the convecting fluid. In addition, the dynamics needs to be studied over long times up to at least the horizontal diffusion time scale, $t \sim \Gamma^2$, which is an estimate of the minimum time for thermal transients to

diffuse over the entire cell and thus for the spatial structure to reach an asymptotic state. Because of this quadratic dependence on the aspect ratio, the time needed to execute the numerical schemes so that an asymptotic state is reached becomes prohibitively long for $\Gamma \gtrsim 50$ (based on current computational resources; for details, see Ref. [22]). The many degrees of freedom and long integration times, together with the need to repeat the simulations for different parameter values, imply that efficient algorithms are essential for studying spatiotemporal chaos.

Because of these requirements, there have been few direct numerical simulations of the Boussinesq equations, Eqs. (1.5)–(1.7), with aspect ratios $\Gamma \gtrsim 20$. Previous attempts have included the following: Pesch et al. have carried out pseudo-spectral simulations (both serial and parallel) up to $\Gamma = 32$ to study spiral defect chaos[30, 34, 68]. However, their code uses periodic boundaries and not the experimentally-realistic boundaries, Eqs. (1.11)–(1.13). Xi et al. [103] have studied the transition to spatiotemporal chaos in a $\Gamma = 30$ square cell, but with the unphysical free-slip horizontal boundaries. Arter and Newell [5], and Tomita and Abe [93] have also carried out simulations in small aspect ratios with thermally insulated no-slip sidewalls, the former in a $\Gamma_x = 8, \Gamma_y = 5.75$ aspect ratio box, the latter in a $\Gamma \approx 10$ square cell.

2.2 Finite difference solver: `boxcode`

The `boxcode` solver is a semi-implicit second-order accurate finite difference solver [22] for a rectangular geometry with the boundary conditions prescribed by Eqs. (1.11)–(1.13). (Periodic and perfectly conducting sidewalls are also possible but will not be considered in this dissertation.) It currently works on a serial workstation, but extending the solver to work on parallel workstations is possible [49]. This solver complements the more flexible spectral element approach, discussed in the next section, by being more than an order of magnitude more efficient on a serial processor (for a box with the same aspect ratio and boundary conditions; see also Fig. 2.4). It is well suited for studying long time dynamics of large-aspect-ratio boxes of $\Gamma \sim 50$ [46].

The main advantages of `boxcode` are the simplicity of implementation and its

efficiency on a single processor. Its simplicity arises from the use of a single mesh for all field values. This is called a "non-staggered" or "colocated" mesh in contrast to a "staggered" mesh for which the values of different fields appear at different points in space [4, 66]. A non-staggered mesh reduces the effort to write and to validate a code (compared to one using a staggered mesh). The use of a single non-staggered mesh also helps to explain the efficiency of the algorithm. Using a standard operator splitting and projection method [8] together with second-order accurate finite differences on a uniform three-dimensional mesh, the advancement of the velocity, temperature, and pressure fields at each time step requires the numerical solution of four Helmholtz equations and one Poisson equation. Because the resulting elliptic equations and their boundary conditions are separable, they can be solved efficiently using fast direct methods from the `FISHPACK` library [88, 89], with a complexity per problem of $O(N \log(N))$, where N is the total number of mesh points. Fast direct methods are more efficient than most iterative methods on a single processor [12], and have the additional advantage that no internal parameters need to be adjusted to obtain convergence. However, fast direct methods are not applicable to complex geometries, to problems with spatially varying parameters, or to complicated boundary conditions that lead to non-separable equations. Complete detail of the algorithm of `boxcode` is available in Ref. [22].

On a workstation with a 667 MHz 21264A 64-bit Alpha processor, a square box with aspect ratio $\Gamma = 20$ and spatial resolution $\Delta x = \Delta y = \Delta z = 1/8$ takes about 4.8 seconds per time step of $\Delta t = 0.001$. This corresponds to 80 minutes per vertical diffusion time and 90 days per horizontal diffusion time, so this code is too slow to explore $\Gamma \gtrsim 10$ cells over time scales exceeding a horizontal diffusion time. On a workstation with a 2 GHz 32-bit Pentium processor, the corresponding times for the same test with same parameters are 4 minutes per vertical diffusion time and 4.5 days per horizontal diffusion time. This then allows the code to explore $\Gamma \gtrsim 50$ cells over time scales exceeding a horizontal diffusion time.

Although mathematically there is no boundary condition for the pressure field — and by discretizing first space and then time, a boundary condition can be avoided

— a Neumann condition,

$$\widehat{n} \bullet \nabla p = 0, \quad \text{on all walls,} \tag{2.1}$$

was imposed. This boundary condition has been shown [37, 92] to produce acceptably accurate results for problems in which the fluid is confined by no-slip surfaces. However, the Gauss divergence theorem may not be satisfied for the Poisson equation for the pressure field that results from applying the projection method,

$$\nabla^2 p^{n+1} = -\nabla^2 p^n + \frac{2}{\Delta t} \nabla \bullet \mathbf{u}^{**}, \tag{2.2}$$

where p^{n+1} is the unknown pressure field to be solved, and p^n and $\mathbf{u}^{**}$ are the pressure field at the previous time step and the intermediate velocity field, respectively. The right-hand side of Eq. (2.2), which in general is nonvanishing, is incompatible with the imposed boundary condition, Eq. (2.1). To overcome this problem, `FISHPACK` instead computes the solution to Eq.(2.2) that minimizes the error in the least-squares sense [88, 89]. The error incurred means that the velocity field is only approximately divergence-free. In Fig. 2.1, the magnitude of this divergence is shown. It plots $|\nabla \bullet \mathbf{u}|$ as a function of x along $y = z = 0$ for a mesh with $\Gamma_x = \Gamma_y = 8$ and spatial resolution $\Delta x = \Delta y = \Delta z = 1/8$, and at the Rayleigh number $R = 3000$ and the Prandtl number $\sigma = 1$. It can be seen that $|\nabla \bullet \mathbf{u}| \sim 10^{-2} \sim \mathcal{O}(h^2)$ where h is the larger of the spatial resolutions Δx, Δy, and Δz.

The algorithm is proven to be second-order by showing that the order of convergence $p \to 2$ in the limits of sufficiently fine time resolutions. By definition, the convergence with respect to time resolution is of order p if $\|u_h - u_{\text{exact}}\| = O(h^p)$ in the limit $h \to 0$, where $\|u\| = \sqrt{\sum_{ijk} u_{ijk}^2}$ denotes the Euclidean norm of a field u on the spatial mesh, $h = \Delta t$ is the uniform time step, $u_h(x, y, z)$ denotes a discrete numerical field obtained using a time step h, and $u_{\text{exact}}(x, yz)$ is the unknown exact field on the spatial mesh. By writing $u_h(x, y, z) = u_{\text{exact}}(x, y, z) + C(x, y, z)h^p$ in the limit $h \to 0$, for some function C independent of h, the order p can be estimated by

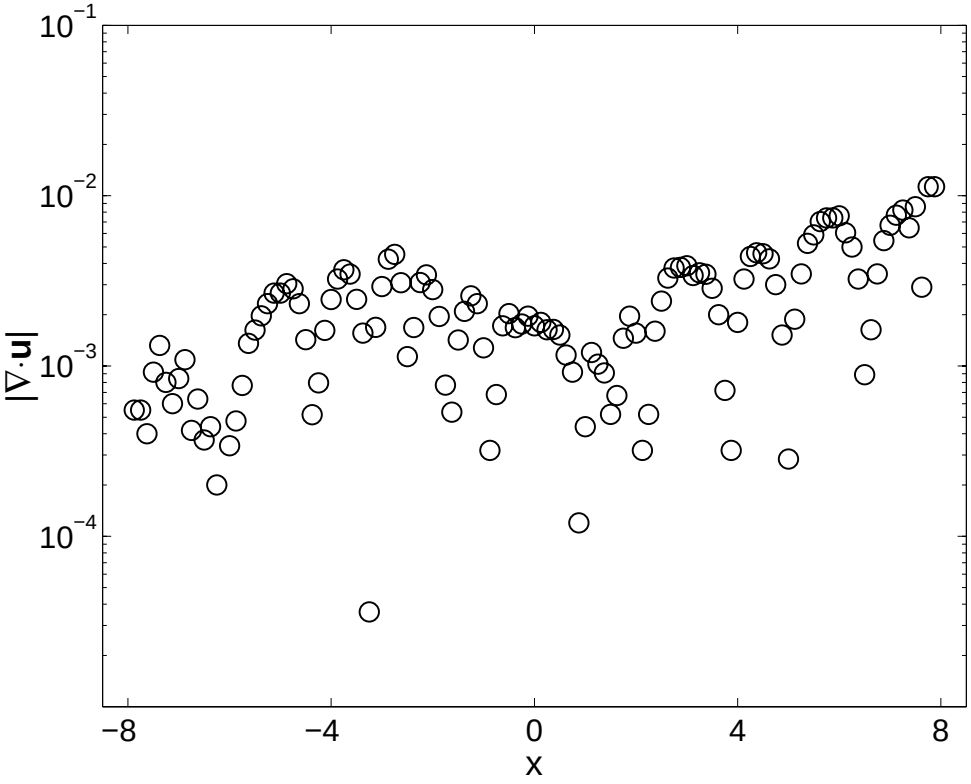

Figure 2.1: Magnitude of the divergence of the velocity field, $|\nabla \bullet \mathbf{u}|$, plotted as a function of x along $y = z = 0$ for a mesh with $\Gamma_x = \Gamma_y = 8$ and spatial resolution $\Delta x = \Delta y = \Delta z = 1/8$, and at the Rayleigh number $R = 3000$ and the Prandtl number $\sigma = 1$.

examining the quantity

$$p_h = \log_2 \left(\frac{\|u_{4h} - u_{2h}\|}{\|u_{2h} - u_h\|} \right), \tag{2.3}$$

in the limit $h \to 0$. The estimate Eq. (2.3) involves field values at the three different time steps $4h$, $2h$, and h, largest to smallest.

The convergence is evaluated for a three-dimensional box with perfectly insulating sidewalls and for parameter values $\Gamma_x = \Gamma_y = 2$, $R = 1725.0 \approx 1.01 R_c$, and $\sigma = 0.71$. The initial conditions consisted of small random perturbation about the linearly conducting state $T = -z$, $\mathbf{u} = \mathbf{0}$, and these were integrated up to 20 time units at which point the state became stationary. For various time steps $h = 0.0001$, 0.00005, and 0.000025, all with a space resolution of $N = 64$, the convergence was found (using

Eq. (2.3)) to be $p = 1.7$. This provides evidence that the code is indeed asymptotically second-order accurate with respect to the time step.

Since an important practical feature of any production code is the largest time step that can be taken before numerical instability occurs, the maximum stable time step as a function of the Rayleigh and Prandtl numbers have also been calculated. A three-dimensional box with periodic sidewalls and aspect ratio $\Gamma_x = \Gamma_y = 2$ was used, with a spatial resolution $\Delta x = 16$. The Euclidean norm of the temperature field, $\|T\|$, was calculated for various values of Δt each time after a interval of twenty vertical diffusion times so that transients decayed. The maximum stable time step was then defined as the value of Δt such that $\|T\|$ remains bounded, i.e., $\|T\| < 10^5$.

In Fig. 2.2, the maximum stable time step as a function of the Rayleigh number is plotted for two Prandtl numbers $\sigma = 1$ (squares) and $\sigma = 10$ (crosses). The maximum stable time step decreases rapidly with increasing Rayleigh number. This is to be expected since the magnitude of the velocity and temperature fields increase with increasing Rayleigh number. In fact, a best log-log fit to the data yields the relation

$$\max(\Delta t) \propto R^{\alpha} \tag{2.4}$$

where $\alpha = -1.2$ when $\sigma = 1$, and $\alpha = -1.3$ when $\sigma = 10$.

In Fig. 2.3, the maximum stable time step as a function of the Prandtl number is plotted for fixed Rayleigh numbers $R = 2048$ (squares) and $R = 8192$ (crosses). For $R = 2048$, the maximum stable time step decreases toward both small and large Prandtl numbers. For $R = 8192$, the maximum stable time step decreases toward small Prandtl numbers but is approximately constant at large Prandtl numbers. The smaller time step needed at small Prandtl numbers can be attributed to the more dynamical nature of the convective flow at small Prandtl numbers, such as the presence of spiral defect chaos [56].

Other methods of validating the accuracy of the algorithm, such as the calculating the critical Rayleigh number and plotting the Nusselt number curve as a function of the Rayleigh number are available in Ref. [22].

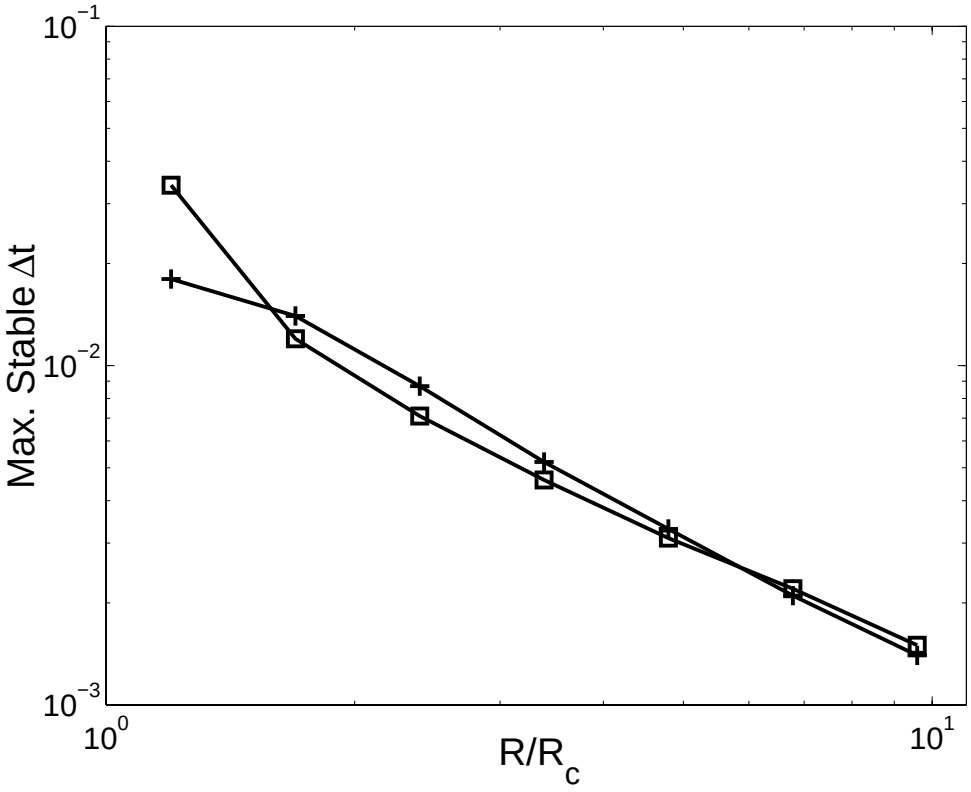

Figure 2.2: Plot of the maximum stable time step as a function of the Rayleigh number. The Prandtl number is kept constant at $\sigma = 1$ (squares) and $\sigma = 10$ (crosses). The cell has aspect ratio $\Gamma_x = \Gamma_y = 2$ and periodic sidewalls. The mesh resolution is $\Delta x = 1/16$. Small random perturbations in the temperature field are used as initial conditions. The simulation is run until twenty vertical diffusion times, at which time the Euclidean norm $\|T\|$ is then calculated. The value of Δt such that this norm becomes greater than 10^5 is defined as the maximum stable time step.

2.3 Spectral element solver: `nek5000`

The `nek5000` solver is a spectral element solver that is implemented efficiently on modern parallel architectures [35]. It was developed by Fischer et al. to study challenging problems in fluid mechanics and heat transfer, such as the flow in a cartoid artery, Rayleigh-Taylor instabilities, etc. It has been adapted by Fischer and Paul [63] to solve the Boussinesq equations in a variety of geometry and boundary conditions, such as cylindrical cells with Eqs. (1.11)–(1.13) [64] and cylindrical cells with a ra-

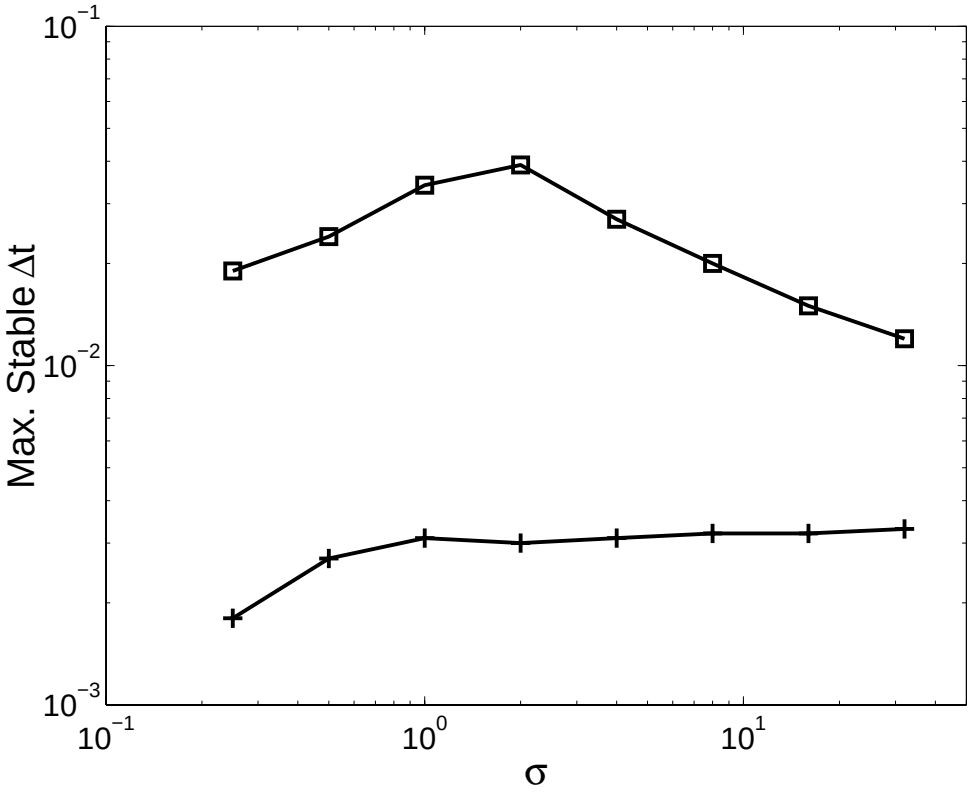

Figure 2.3: Plot of the maximum stable time step as a function of the Prandtl number. The Rayleigh number is kept constant at $R = 2048$ (squares) and $R = 8192$ (crosses). The same aspect ratio, mesh resolution, and initial conditions as in Fig. 2.2 are used.

dial ramp in plate separation [65]. Complete detail of the algorithm of `nek5000` is available in Refs. [35, 96].

Briefly, the temporal discretization is based on the high-order operator splitting approach of Ref. [51]. The nonlinear convective term is expressed as a material derivative, which can be discretized by, for example, second-order backwards differentiation, leading to a linearly symmetric Stokes problem that can be solved implicitly at each time step using the iterative method of parallel preconditioned conjugate gradients [37, 92]. The spatial discretization uses the spectral element method, which is exponentially convergent, and can asymptotically achieve higher accuracy for a given number of numerical degrees of freedom than a finite difference code such as `boxcode`. These have been implemented efficiently on modern parallel architectures,

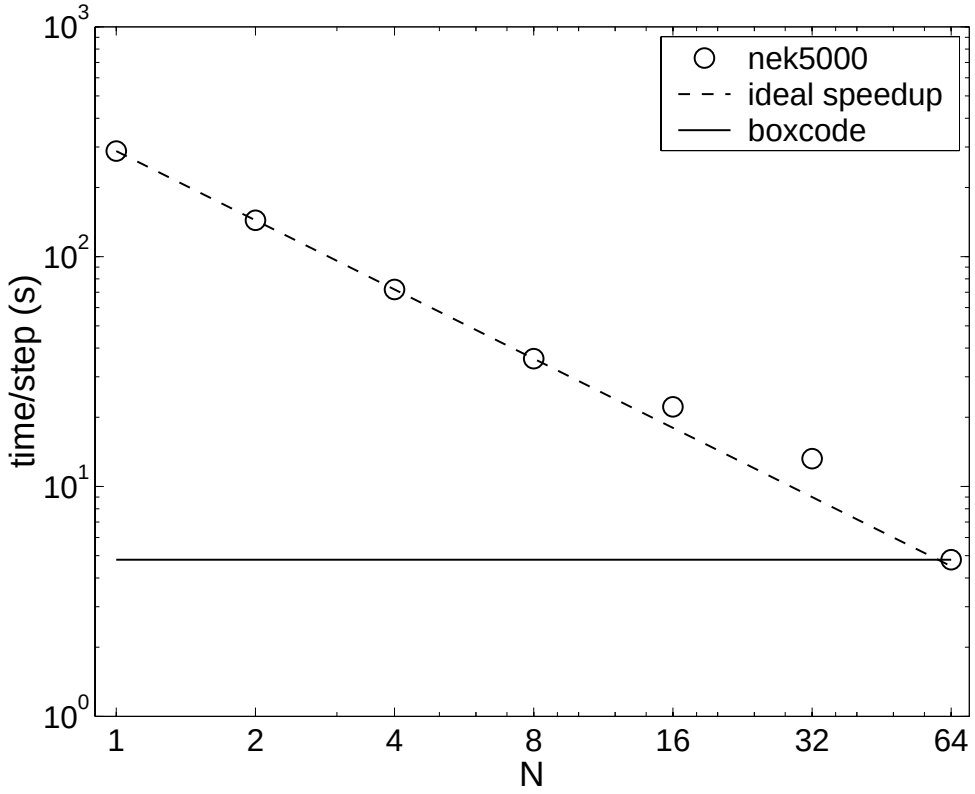

Figure 2.4: Parallel speedup of the `nek5000` solver. The wall time needed to integrate one time step using `nek5000` for an aspect ratio $\Gamma = 20$ rectangular cell with 8×10^5 mesh points is plotted as a function of N, the number of processors used in parallel. Ideal speedup is denoted by the dashed line. For comparison, the wall time needed to integrate one time step using the `boxcode` solver for the same number of mesh points and parameters is plotted as the solid horizontal line.

thus allowing the simulation of Rayleigh-Bénard convection in large aspect ratios of up to $\Gamma = 50$.

To illustrate this efficiency, the parallel speedup of `nek5000` is plotted in Fig. 2.4. Speedup is measured by measuring the wall times needed in `nek5000` to integrate, say, one time step as a function of the number of processors used, while maintaining the mesh size and all parameters of the problem constant. The `nek5000` is able to attain a near-ideal speedup. For comparison, the wall time needed in `boxcode` to integrate one time step for the same mesh spacing and parameters is plotted as the solid horizontal line.

Chapter 3

Importance of mean flow in spiral defect chaos

3.1 Introduction

Since the discovery of spiral defect chaos in Rayleigh-Bénard convection experiments [56], the following facts about spiral defect chaos have been established: The parameter values for which it appears [44, 45, 48, 56, 57], namely, the Rayleigh number $R \gtrsim 3000$, the Prandtl number $\sigma \sim 1$, and the aspect ratio $\Gamma \gtrsim 20$; the distributions of local roll properties such as the wave number [33]; statistics of spiral and defect populations [32, 31]; the mechanisms for the generation of chaos from spatial disorder [34]; the wave number selection mechanism for spirals [26, 95]; and the conditions under which spiral defect chaos transitions to other states. Of particular interest to this chapter are experiments [6, 7] that have observed that the spirals transform into targets when the Prandtl number is increased from $\sigma \sim 1$ to $\sigma \sim 10$ and when the Rayleigh number $R \gtrsim 3500$. While this observation establishes that spiral defect chaos occurs only at low Prandtl numbers, it does not allow one to conclude which of the many dynamic phenomena that occur at low Prandtl numbers [27] is responsible for the formation of spiral defect chaos.

One particular phenomenon that becomes important at low Prandtl numbers is the presence of mean flow [58, 59, 82]. Mean flow is the name given to the velocity field with a non-zero mean over the depth of the convective cell that is generated

by the variations of the structure of the convection rolls such as their curvature, amplitude, and wave number, and that in turn couples through advection to further modify the roll structure [25]. Its magnitude is approximately inversely proportional to the Prandtl number [29].

It is believed that spiral defect chaos is an effect of the mean flow which in turn is important at low Prandtl numbers [56, 57]. This hypothesis has been investigated in numerical studies of the Swift-Hohenberg model equation. For example, by coupling a mean-flow-like field to the Swift-Hohenberg equation [50, 90], chaotic behavior is observed [41]. Furthermore, when the parameter in the model that gives the strength of the mean flow is made large, spatiotemporal chaotic states akin to spiral defect chaos are observed [47, 94, 102, 101]. However, as discussed in Sect. 1.3, results obtained from these model equations are tenuous.

The goal of this chapter is to describe the results of direct numerical simulations of Rayleigh-Bénard convection that will show that spiral defect chaos is indeed a consequence of the presence of mean flow. In the absence of mean flow, spiral defect chaotic states are found to cease to exist, and are replaced by states whose statistical properties differ from those of spiral defect chaos. In general, studies of mean flow are difficult to perform in experiments, primarily because it is difficult to measure mean flow in an experimental setup. This is due to several reasons, namely that the magnitude of mean flow is small (typically of the order of 1% of the magnitude of the velocity of the convecting rolls), and that it exists only in distorted and not regular patterns. There has only been one experiment that has successfully imaged aspects of the mean flow, but only in a simple distorted pattern [23, 70]. It is not clear if such imaging techniques can be applied to more general and complicated patterns. Thus, the direct numerical simulations described in Chap. 2 are particularly valuable for the study of mean flow.

The novel approach of this dissertation is the construction of a *gedanken* fluid whose velocity field is modified to have zero mean flow. By investigating the states that arise from the dynamics of this fluid and by comparing them with spiral defect chaos, the role of mean flow in the formation and dynamics of spiral defect chaos can

be directly inferred.

The capability to remove mean flow from the fluid dynamics can be applied to the study of other problems as well. One such problem is the relation between mean flow and lateral boundaries. In Sect. 3.3.6, mean flow is shown to contribute to the commonly observed phenomenon of convection rolls terminating perpendicularly into lateral walls, an observation that is still without much theoretical understanding.

3.2 Definitions

3.2.1 Mean flow

When the convection pattern is made up of rolls that are neither concentric nor straight and parallel, a mean flow, slowly varying in the horizontal coordinates, will be set up. The importance of mean flow is that it is a nonlocal flow mode, and as such, affects the global behavior of the convection pattern even though its magnitude is small. A detailed derivation of mean flow can be found in Ref. [59]. Heuristically, it can be understood as follows. When there are inhomogeneities in the amplitude $A(x, y)$ and wave vector $\mathbf{k}(x, y)$ (or equivalently, the phase $\phi(x, y)$ where $\nabla_\perp \phi = \mathbf{k}$) of the convection rolls, a Reynolds stress will be generated locally from the gradients of A and $\mathbf{k}$. This results in a flow slowly varying in the plane. In addition, these inhomogeneities will also induce a varying component $p_s(x, y, t)$ in the pressure field that is constant across the depth of the cell and slowly varying in the plane. The gradient $\nabla_\perp p_s$ will then drive a global flow that, together with the Reynolds-stress-induced flow, distorts the convection rolls further. If the slowly varying flow is called $\mathbf{u}_D$, then [29]

$$\sigma \partial_{zz} \mathbf{u}_D = \nabla_\perp p_s + \frac{1}{2\pi} \int_0^{2\pi} d\phi \, \mathbf{u} \bullet \nabla \mathbf{u}_\perp, \tag{3.1}$$

where the integral over the phase variable ϕ serves to average out the fast modes of the integrand. The as yet unknown field p_s can be determined via the incompressibility

condition, Eq. (1.7), which requires that

$$\nabla_\perp \bullet \int_{-1/2}^{1/2} dz\, \mathbf{u}_D(x,y,z,t) = 0. \tag{3.2}$$

Eq. (3.1) can then be integrated twice with respect to z, with boundary condition Eq. (1.11), to completely give $\mathbf{u}_D$. Finally, the slow distortions, $\mathbf{u}_D$, advect the phase contours of the convection rolls, yielding an additional advection term in the phase equation [29],

$$\partial_t \phi \to \partial_t \phi + \mathbf{U} \bullet \nabla_\perp \phi. \tag{3.3}$$

The velocity field $\mathbf{U}$ is called the mean flow. It is an average of the slow distortions over the depth of the cell,

$$\mathbf{U}(x,y,t) = \int_{-1/2}^{1/2} dz\, \mathbf{u}_D(x,y,z,t) g(z), \tag{3.4}$$

with $g(z)$ a weighting function that in principle can be calculated from the nonlinear structure of the rolls [27, 59].

The mean flow can be approximated from the direct numerical simulations as the average over the depth of the cell of the slow components of the horizontal velocity,

$$\mathbf{U}(x,y,t) \approx \frac{1}{2\pi} \int_0^{2\pi} d\phi \int_{-1/2}^{1/2} dz\, \mathbf{u}_\perp(x,y,z,t). \tag{3.5}$$

In practice, the integral over the phase variable ϕ is replaced with a Gaussian filter of characteristic width $\mathcal{O}(1)$ so that variations over short length scales are smoothed out.

For the approximation of Eq. (3.5), and with the no-slip boundaries Eq. (1.11), the mean flow $\mathbf{U}(x,y,t)$ is solenoidal:

$$\nabla_\perp \bullet \mathbf{U} = 0. \tag{3.6}$$

It is also sometimes convenient to use the mean flow stream function, $\zeta(x,y,t)$, and

the vertical component of the mean flow vorticity, ω_z, defined by

$$-\nabla_\perp^2 \zeta = \omega_z = \widehat{z} \bullet (\nabla_\perp \times \mathbf{U}) . \tag{3.7}$$

The stream function, in particular, is useful to visualize because it gives the stream lines and so the geometry of the mean flow.

3.2.2 Quenching mean flow

In this section, a procedure to construct a modified velocity field that does not have any mean flow is prescribed. The goal is to add a forcing term, $\mathbf{\Phi}$, to the fluid equation, Eq. (1.5), to make the resulting fluid dynamics have zero mean flow. The functional form of $\mathbf{\Phi}$ will now be derived.

As mentioned above, the mean flow comprises a local component generated by the Reynolds stress $1/(2\pi) \int_0^{2\pi} d\phi \mathbf{u} \bullet \nabla_\perp \mathbf{u}_\perp$ and a global component driven by a slow horizontal pressure gradient that is present in order to guarantee the incompressibility condition, Eq. (1.7). Thus, if the Reynolds stress is subtracted from the dynamics at all times, then mean flow will not be generated. The following can then be written,

$$\mathbf{\Phi}(x, y, t) = \rho \int_{-1/2}^{1/2} dz \mathbf{u} \bullet \nabla \mathbf{u}_\perp, \tag{3.8}$$

where the operator $\rho \int_{-1/2}^{1/2} dz$ serves as an average over the depth of the cell.

The value of the constant ρ now needs to be evaluated. To do this, the equation for the slow distortions, Eq. (3.1), can be rewritten as

$$\sigma \partial_{zz} \mathbf{u}_D = \nabla_\perp p_s + \frac{1}{2\pi} \int_0^{2\pi} d\phi \, \mathbf{u} \bullet \nabla \mathbf{u}_\perp - \mathbf{\Phi}. \tag{3.9}$$

Following Ref. [29], the Reynolds stress term near threshold takes the form

$$\frac{1}{2\pi} \int_0^{2\pi} d\phi \, \mathbf{u} \bullet \nabla \mathbf{u}_\perp \equiv I(k, z) \mathbf{R}(x, y). \tag{3.10}$$

where

$$\mathbf{R}(x,y) \equiv \mathbf{k}\nabla_\perp \bullet (\mathbf{k}A^2), \tag{3.11}$$

and

$$I(k,z) \equiv w_0(k,z)\partial_z \frac{\partial \phi_0(k,z)}{\partial k_c^2} - \frac{\partial w_0(k,z)}{\partial k_c^2}\partial_z \phi_0(k,z), \tag{3.12}$$

with $w_0(k,z)$ and $\phi(k,z)$ the vertical profiles of the vertical velocity and the potential of the horizontal velocities, respectively. For systems satisfying the rigid boundary condition, Eq. (1.11), these functions are the familiar Chandrasekhar functions [19].

Eq. (3.9) can then be rewritten as

$$\sigma\partial_{zz}\mathbf{u}_D = \nabla_\perp p_s + I(k,z)\mathbf{R}(x,y) - \rho\int_{-1/2}^{1/2} dz I(k,z)\mathbf{R}(x,y). \tag{3.13}$$

Integrating Eq. (3.13) with respect to z twice, and making use of the boundary condition, Eq. (1.11),

$$\sigma\mathbf{u}_D = p(z)\nabla_\perp p_s + J(k,z)\mathbf{R}(x,y) - p(z)\rho\int_{-1/2}^{1/2} dz I(k,z)\mathbf{R}(x,y), \tag{3.14}$$

with

$$p(z) \equiv \frac{1}{2}\left(z^2 - \frac{1}{4}\right) \tag{3.15}$$

the Poiseuille profile, and $J(k,z)$ the double integral of $I(k,z)$ with respect to z. Employing the incompressibility condition, Eq. (3.2), the following equality is derived:

$$\rho = \frac{12\int_{-1/2}^{1/2} dz J(k,z)}{\int_{-1/2}^{1/2} dz I(k,z)}. \tag{3.16}$$

These integrals can then be evaluated, and the resulting values of ρ as a function of k are plotted in Fig. 3.1. The value of ρ is found to be approximately 1.5, independent of k, suggesting the validity of treating it as a constant in the first place.

Finally, to numerically confirm this result, the quenching of the mean flow, as described in Eq. (3.17), is carried out for a range of values for ρ, at the reduced Rayleigh number $\epsilon = 1.0$ and several values of the Prandtl number, and in a rectangular cell

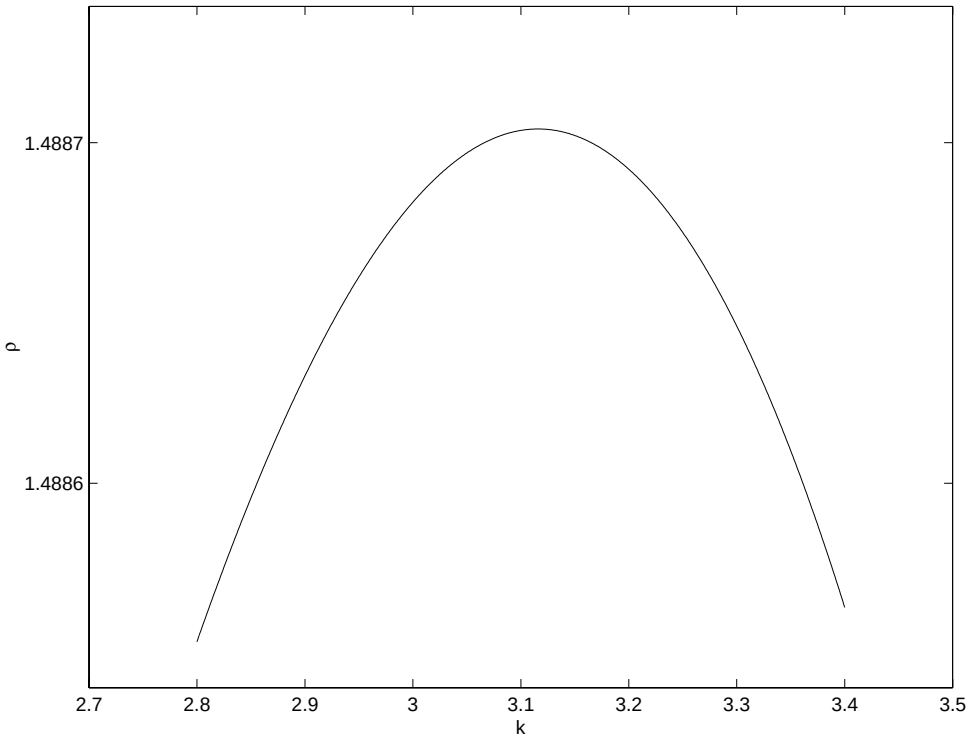

Figure 3.1: The value of ρ as a function of the wave number k evaluated according to Eq. (3.16). It can practically be taken to be a constant, $\rho \approx 1.5$ for all values of k.

of $\Gamma_x = \Gamma_y = 20$. At ten time units after affecting the quenching, the maximum magnitude of the mean flow as a function of ρ is measured. The results are shown in Fig. 3.2, where the maximum mean flow magnitude (normalized by the maximum mean flow magnitude observed without quenching) vs. ρ is plotted. When $\rho \approx 1.5$, the normalized maximum mean flow magnitude is indeed zero.

Now, the additional term $\mathbf{\Phi}$ given by Eq. (3.8) with $\rho = 1.5$ can be added to the fluid equation, so that Eq. (1.5) becomes

$$\sigma^{-1} \left(\partial_t + \mathbf{u} \bullet \nabla \right) \mathbf{u}(x, y, z, t) = -\nabla p + \nabla^2 \mathbf{u} + RT\widehat{z} + \sigma^{-1}\mathbf{\Phi}. \tag{3.17}$$

If $\mathbf{\Phi}$ is introduced at time $t = t_q$, the time needed for the modified velocity field $\mathbf{u}$ to respond to this additional forcing can be estimated by applying dimensional arguments on the terms in Eq. (3.17). This time scale is $\mathcal{O}(\sigma)$. For example, when

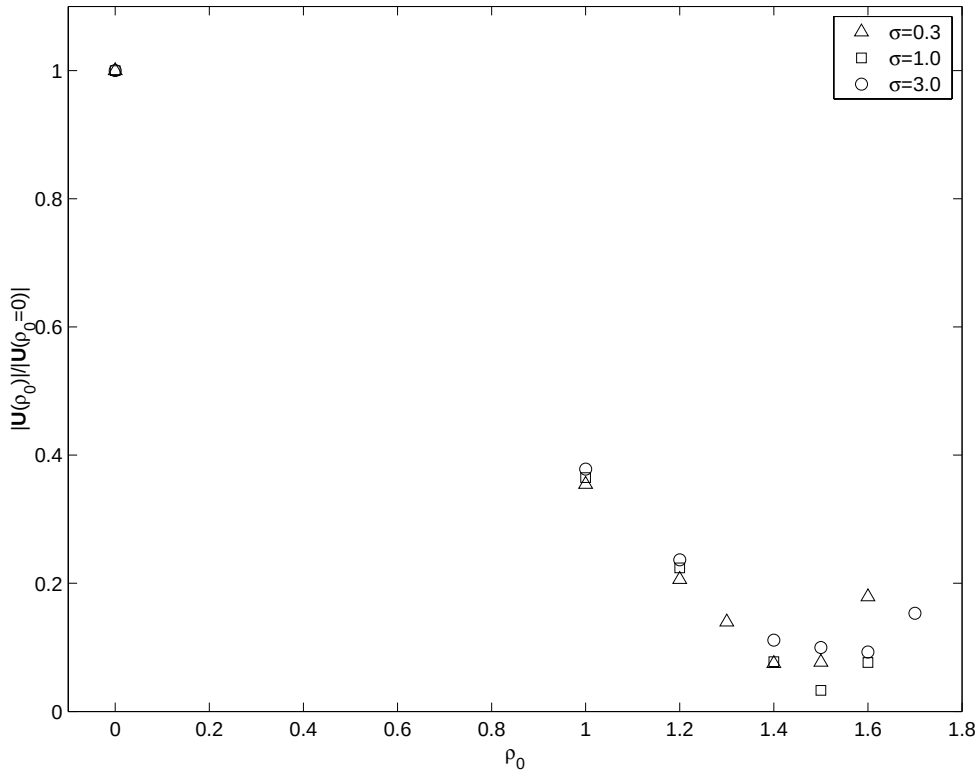

Figure 3.2: The maximum mean flow magnitude vs. various trial values of ρ. The mean flow magnitudes are normalized by their values at $\rho = 0$, i.e., when there is no quenching. When $\rho \approx 1.5$, the mean flow goes to zero, for all three Prandtl numbers.

$\sigma = 1$ when spiral defect chaos appears, the mean flow is expected to be quenched in a time scale of $\mathcal{O}(1)$ from time t_q.

For a pattern that does not have mean flow, such as a pattern comprising straight parallel rolls with no defects or concentric circular rolls, the quenching procedure should leave the convective properties, such as the Nusselt number N, of the fluid unchanged. [The Nusselt number is the ratio of convective heat transfer to heat transfer that would occur by conduction alone if the fluid remained at rest. It can be computed by

$$N = 1 + \langle w\,(T - T_{\text{cond}})\rangle, \tag{3.18}$$

where w is the z-component of the velocity field and $T_{\text{cond}} = -z$ is the temperature profile of the linear conducting state with $\mathbf{u} = \mathbf{0}$. The brackets $\langle \cdots \rangle$ denote an average

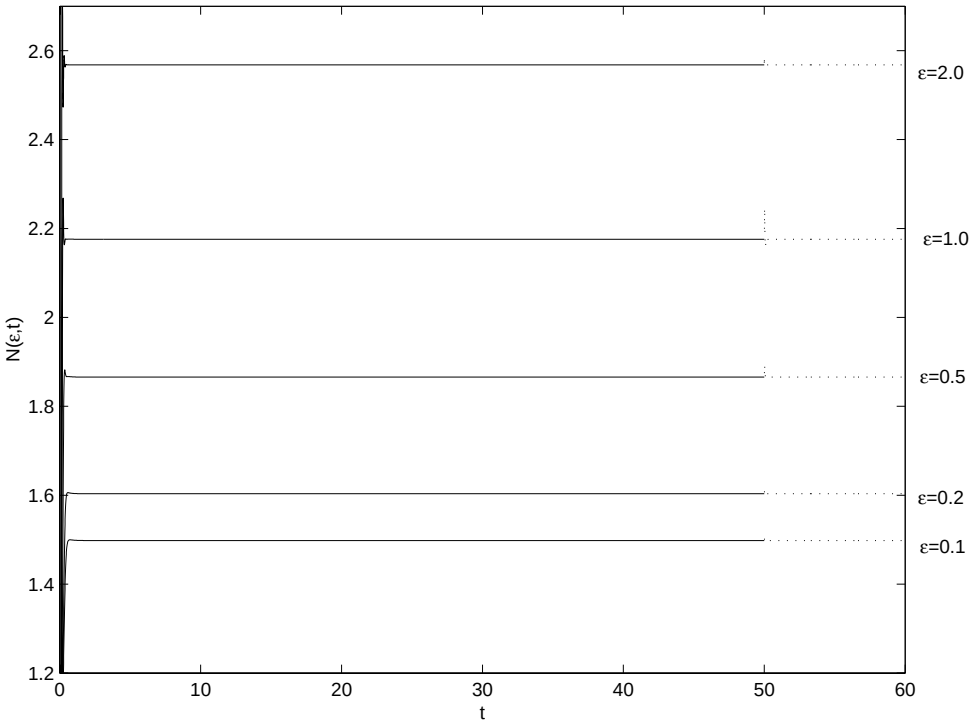

Figure 3.3: Time series of the Nusselt number $N(\epsilon, t)$ for patterns comprising straight parallel rolls that have no mean flow at several values of ϵ before (denoted by solid lines) and after (dotted lines) quenching of the mean flow, which occurred at time $t_q = 50$. All data reported here are for the Prandtl number $\sigma = 1$ and in a rectangular cell of aspect ratio $\Gamma_x = \Gamma_y = 20$. (In order to achieve straight parallel rolls, periodic lateral boundaries were imposed and a small sinusoidal perturbation in the temperature field was used as the initial condition.)

of a quantity over the cell.] This is shown to be true in Fig. 3.3. The Nusselt numbers before (denoted by solid lines) and after (dashed lines) the quenching procedure, which occurred at $t = t_q = 50$, are indeed the same.

3.3 Results

3.3.1 Quenching mean flow applied to spiral defect chaos

Using the `boxcode` and `nek5000` solvers described in Chap. 2, Eqs. (1.6), (1.7), and (3.17) are evolved from the initial conditions

$$\mathbf{u}(x, y, z, t = 0) = \mathbf{0}, \quad p(x, y, z, t = 0) = 0, \tag{3.19}$$

and

$$T(x, y, z, t = 0) = -z + \eta(x, y, z), \tag{3.20}$$

where $T = -z$ is the linear conduction profile and η is randomly chosen from a uniform distribution such that $-10^{-5} \leq \eta \leq 10^{-5}$. Spiral defect chaos is observed when the parameters are chosen such that the reduced Rayleigh number ϵ lies in the range $0.6 \leq \epsilon \leq 3.0$, the Prandtl number $\sigma \approx 1$, and the aspect ratio lies in the range $16 \leq \Gamma \leq 30$. In Fig. 3.4(a), an example is shown: a planform of the mid-plane temperature field $T(x, y, z = 0)$ at time $t = 500$ for parameters $\epsilon = 1.0$, $\sigma = 1$, and $\Gamma_x = \Gamma_y = 20$. In general, the planforms observed are qualitatively similar to those observed in experiments in both cylindrical [56] and rectangular [16] geometries.

In the rest of this section, results are reported on simulations performed in a rectangular cell of aspect ratio $\Gamma_x = \Gamma_y = 20$ integrated for 500 time units. At time $t = t_q = 500$, the forcing term given by Eq. (3.8) that will quench the mean flow dynamics is invoked. In Fig. 3.4(b), the mid-plane temperature field at time $t = 510$ which is ten time units after the quenching of the mean flow has begun is plotted. [Recall that the quenching takes place in a time of $\mathcal{O}(\sigma)$ so the quenched state at ten time units should have already been asymptotic for these $\sigma = 1$ states.] As can be seen, the rolls have "straightened out" in that they have lost their curvature and have developed angular bends. More strikingly, the straightened roll patches become stationary, leaving the only dynamics in the pattern to come from the motion of defects such as dislocations and grain boundaries. To illustrate this transition from a

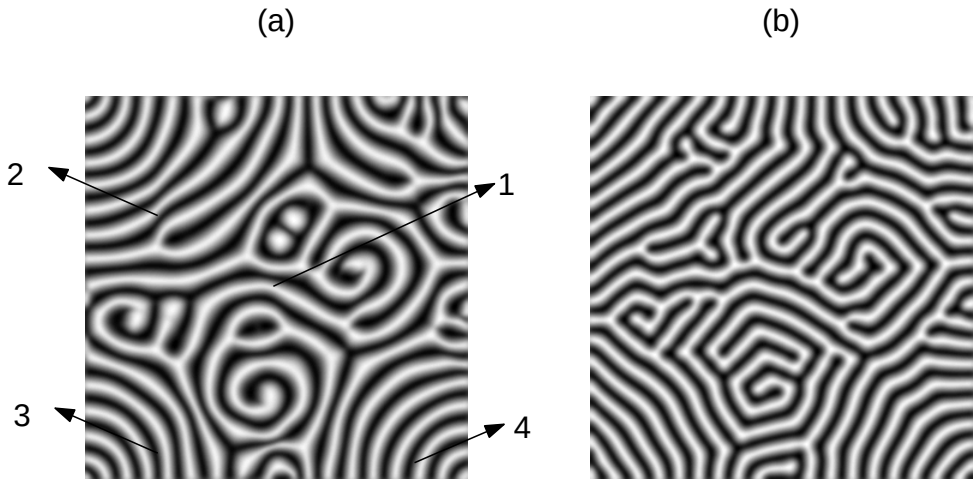

Figure 3.4: *(a)* An example of spiral defect chaos observed in a numerical simulation using the `boxcode` solver. The mid-plane temperature field is plotted at time $t = 500$ for parameters $\epsilon = 1.0$, $\sigma = 1$, and $\Gamma_x = \Gamma_y = 20$. Dark regions correspond to cold sinking fluid, light regions to hot rising fluid. The spiral defect chaos planform is characterized by a disordered collection of spirals rotating in both directions and coexisting with dynamical defects such as grain boundaries and dislocations. The labels "1" to "4" are discussed in Fig. 3.5. *(b)* When mean flow is quenched, spiral defect chaos collapses to a stationary pattern of textures of stripes with angular bends. The planform shown here is at 10 time units after the quenching has been introduced to the state shown in (a). All other parameters are unchanged.

dynamical state to a seemingly "frozen" one, Fig. 3.5 shows the time series of the rate of change of the temperature field at several locations in the cell. For $t < t_q = 500$, the derivative $dT(x, y)/dt$ fluctuates and is significantly different from zero at all $t < t_q$. However, after the quenching of the mean flow is initiated at $t = t_q = 500$, the derivative $dT(x, y)/dt$ relaxes to approach zero in a time scale of $\mathcal{O}(1)$, suggesting that all dynamics is becoming "frozen" and that a stationary pattern is being approached.

The quenching of the mean flow has also been repeated at other Rayleigh numbers ranging from $\epsilon = 0.6$ to 3.0, and for different instances of the initial condition Eq. (3.20). In all cases, similar stationary planforms as shown in Fig. 3.4(b) are observed. In addition, this spiral-to-angular transition can be observed in the reverse direction. When the mean flow quenching is turned off at a later time $t = 550$ so that mean flow is again restored to the system, the angular bends develop into spirals

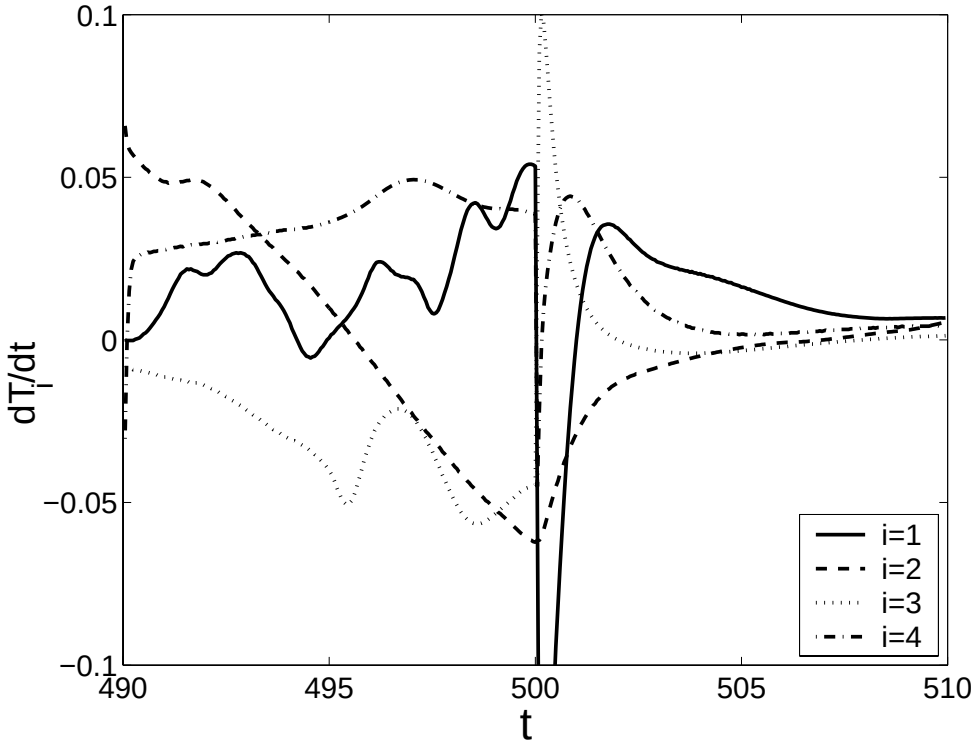

Figure 3.5: The rate of change of the temperature field dT_i/dt versus time t for the four locations in the cell indicated in Fig. 3.4(a). Prior to quenching of the mean flow which takes place at time $t = t_q = 500$, the derivative dT/dt fluctuates and differs from zero. After quenching, it approaches zero in a time scale of $\mathcal{O}(1)$, suggesting that the pattern is approaching stationarity.

and the stationary planform becomes dynamical again. Spiral defect chaos is fully restored. Furthermore, the stationary textures of stripes with angular bends can also be observed when the quenching is initiated at other times. For example, instead of initiating the mean flow quenching procedure at a time when a spiral defect chaotic state is already asymptotic, the quenching procedure has also been initiated immediately at the start of the simulation, $t = t_q = 0$, again using Eqs. (3.19)–(3.20) as initial conditions. In Fig. 3.6(a), the planform after 100 time units for the parameters $\epsilon = 1.0$, $\sigma = 1$, and $\Gamma_x = \Gamma_y = 20$ is shown. It is comprised of patches of locally straight rolls ending into each other in angular bends. There are no spirals present. When mean flow is restored at time $t = 100$, after a time of $\mathcal{O}(1)$, spiral defect chaos appears, as can be seen in Fig. 3.6(b) which shows the planform at 500 time units

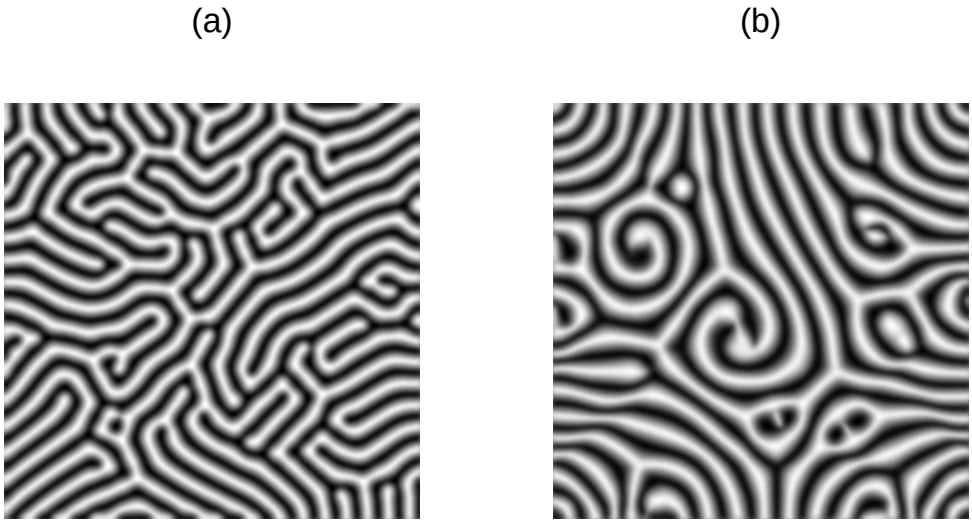

Figure 3.6: *(a)* Stationary patches of stripes with angular bends at time $t = 100$ when mean flow quenching is introduced at time $t = 0$. The parameters are $\epsilon = 1.0$, $\sigma = 1$, and $\Gamma_x = \Gamma_y = 20$. *(b)* When the quenching is turned off at time $t = 100$ so that mean flow is restored, spiral defect chaos is observed. The planform shown here is at 500 time units after the restoration of mean flow.

after the mean flow has been restored.

Thus, this section has shown that spiral defect chaos does not exist without the presence of mean flow.

Before concluding this section, the differences between the states observed when mean flow is quenched and at high Prandtl numbers, for which mean flow is weak, are qualitatively compared. (Recall that the magnitude of mean flow is inversely proportional to the Prandtl number.) Starting from the state shown in Fig. 3.4(a), the Prandtl number for that state is instantaneously increased from $\sigma = 1$ to $\sigma = 10$ at time $t = 500$. Although increasing the Prandtl number changes the convective properties of the fluid and hence the dynamics of the state, it is nevertheless observed [see Fig. 3.7(a)] that stripes with angular bends are similar to those observed when the mean flow is quenched. Thus, the states observed when the mean flow is quenched and unquenched states observed at high Prandtl numbers are similar. In addition, in Fig. 3.7(b) the state observed when the mean flow quenching procedure after increasing the Prandtl number to $\sigma = 10$ is shown. It is again similar to the pattern

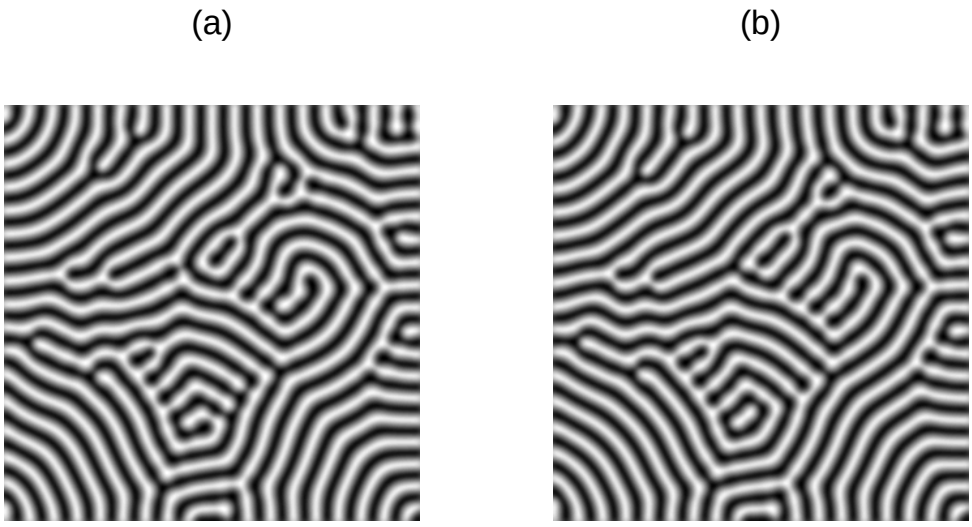

Figure 3.7: *(a)* The pattern observed when the Prandtl number is instantaneously increased from $\sigma = 1$ to $\sigma = 10$ comprises stripes with angular bends that are similar to the quenched patterns in Fig. 3.4(a). The pattern shown here is at 100 time units after the Prandtl number has been instantaneously increased. The parameters correspond to those of the state in Fig. 3.4. *(b)* When the mean flow is quenched for the $\sigma = 10$ state of (a), the resulting pattern is qualitatively unchanged. Shown here is the state at 100 time units after the mean flow has been quenched.

at $\sigma = 10$, suggesting that even at $\sigma = 10$, the residual mean flow components are negligible.

Finally, it is also worthwhile to note that, contrary to the results of Assenheimer and Steinberg [6, 7], the transition from spirals to targets as the Prandtl number is increased to $\sigma = 10$ is not observed. Several explanations are plausible: First, in the Assenheimer and Steinberg experiments, non-Boussinesq effects are significant [6, 7], whereas in this dissertation, the direct numerical simulations are only for Boussinesq fluids. Second, the smaller aspect ratios may not support the formation of targets, and that the direct numerical simulations would indeed see the spiral to target transition in larger aspect ratios. Third, the transition to targets may be strongly dependent on the history of the system, in particular on the path (in parameter space) that the parameters traverse.

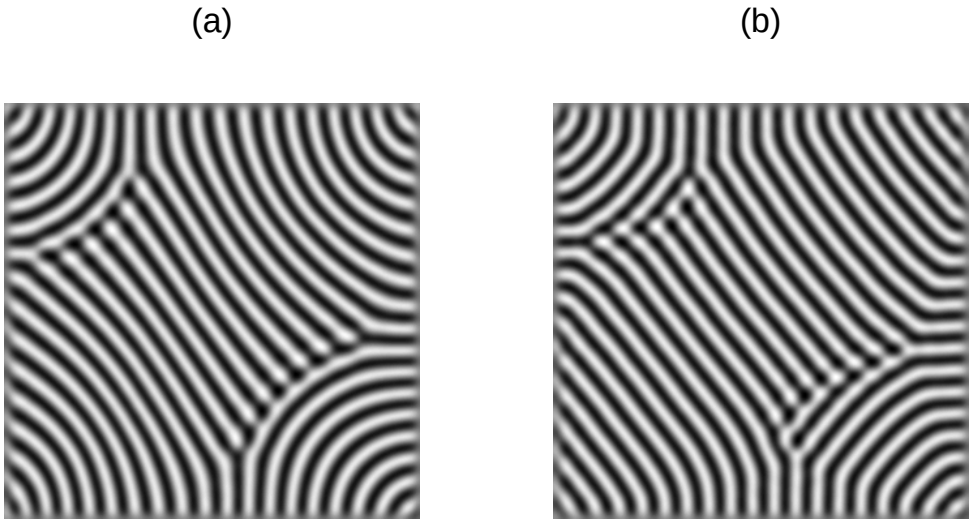

Figure 3.8: *(a)* Mid-plane temperature field at time $t = 500$ for parameters $\epsilon = 0.15$, $\sigma = 1$ and $\Gamma_x = \Gamma_y = 20$. The stripe texture comprises patches of locally parallel rolls and arcs that are stationary. *(b)* The state of (a) observed at 10 time units after the mean flow is quenched. The curved rolls have transitioned into stripes with angular bends that are stationary.

3.3.2 Quenching mean flow applied to pre-chaotic stripe textures

At lower Rayleigh numbers near the convective threshold, the planforms observed take the form of stripe textures rather than exhibiting spiral defect chaos. While stripe textures are not a form of spatiotemporal chaos, it is nevertheless interesting to study how quenching the mean flow affects them. They comprise patches of locally parallel rolls and arcs such that each patch terminates at the boundaries of another at a different orientation, and the boundaries between the patches are usually populated by defects. In general, the stripe textures are stationary after transients, except for the motion of defects at the grain boundaries. In Fig. 3.8(a), a planform of the mid-plane temperature field is shown at time $t = 500$ at $\epsilon = 0.15$ and $\sigma = 1$ in a rectangular cell of aspect ratio $\Gamma_x = \Gamma_y = 20$.

When the mean flow is quenched at time $t = t_q = 500$, the stationary stripe textures remain stationary, and those rolls that are curved are straightened out. The

resulting pattern, shown in Fig. 3.8(b) which is at 10 time units after the quenching, comprises patches of angular structures that replaced patches of curved arcs.

3.3.3 Nusselt number variations

One way to quantify the changes introduced by the quenching procedure to a pattern is to look at its global convective properties, such as the Nusselt number. For a pattern with mean flow, the Nusselt number will be different from those of the unmodified velocity field of Eq. (3.17) because the latter is not a solution to the Boussinesq equations. An alternate way of saying this is that Eq. (3.17), together with Eqs. (1.6) and (1.7), can be interpreted as the driven Boussinesq equations with a driving force $\sigma^{-1}\mathbf{\Phi}$ that is turned on at time t_q. Owing to this driving, the convective properties of the fluid is expected to be stronger at time $t > t_q$ than at time $t < t_q$. This is illustrated in Fig. 3.9. The fractional change in the Nusselt number $\Delta N/N$ caused by the introduction of the quenching of the mean flow increases with the reduced Rayleigh number. A best linear fit to the data yields the relation

$$\Delta N/N = (0.052 \pm 0.005)\epsilon. \tag{3.21}$$

Thus, for example, when $\epsilon \sim 1$, modifying the velocity field to quench the mean flow introduces a change of approximately 5% to the averaged convective properties of the fluid.

3.3.4 Wave number distributions

In this section, the differences between the patterns observed with mean flow and with mean flow quenched are quantified by studying the wave number distributions. The probability density function of wave numbers, $P(k)$, is computed from a time-average of the patterns, using Eq. (1.15). The mean of the wave number distribution then gives the mean wave number $\langle k \rangle(\epsilon)$ as a function of the reduced Rayleigh number ϵ. The mean wave numbers obtained from the above numerical simulations of spiral

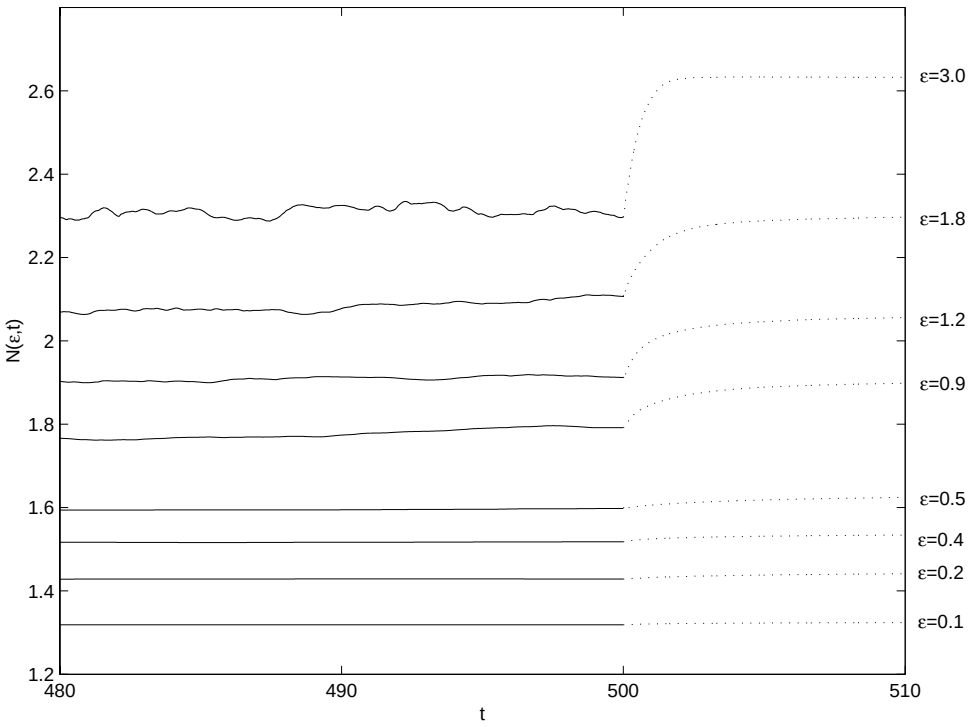

Figure 3.9: Time series of the Nusselt number $N(\epsilon, t)$ for stripe textures and spiral defect chaos at several values of ϵ before (denoted by solid lines) and after (dotted lines) quenching of the mean flow which occurred at time $t_q = 500$. All data reported here are for Prandtl number $\sigma = 1$ and a rectangular cell of aspect ratio $\Gamma_x = \Gamma_y = 20$.

defect chaos lie within the Busse stability balloon [15]. In addition, they are also consistent with existing theory for the selection of wave numbers in spiral defect chaos [26, 95], which suggests that the wave numbers of convecting spirals are "frustrated," i.e., they lie between two competing selection mechanisms, selection by focus-type singularities [13, 14] and selection by dislocations [10, 69]. The former is the unique wave number possessed by axisymmetric rolls (as illustrated in the right panel of Fig. 1.1) in large geometries. The latter is the wave number in straight and parallel rolls (as illustrated in the left panel of Fig. 1.1) at which an added dislocation does not climb in either direction along the rolls. These two sets of selected wave numbers, at $\sigma = 1$, are denoted in Fig. 3.10 by the dashed and the dotted lines, respectively. The direct numerical simulations produced wave numbers (denoted by the circles) that lie within these two sets of selected wave numbers. For comparison purposes,

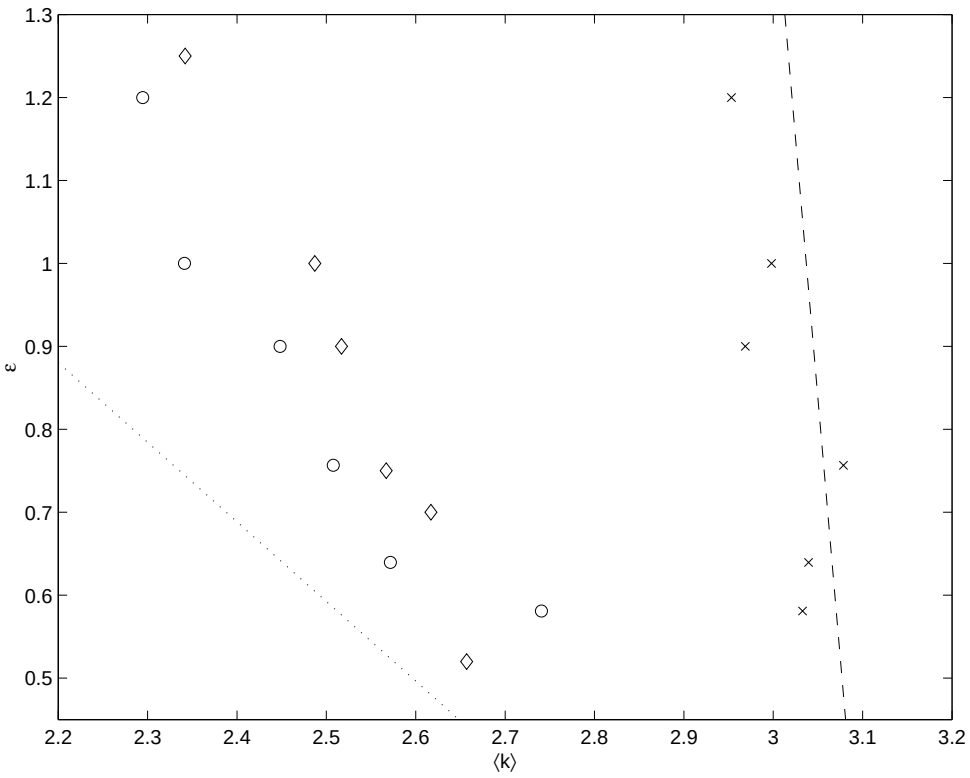

Figure 3.10: Mean wave numbers $\langle k \rangle$ vs. reduced Rayleigh numbers ϵ. The circles denote wave numbers estimated for spiral defect chaotic states at $\sigma = 1$ and $\Gamma_x = \Gamma_y = 20$. The crosses denote wave numbers for states observed at 10 time units after mean flow is quenched. For comparison, the diamonds denote wave numbers obtained in the experiment of Ref. [56]. The dashed line denotes the unique wave number k_f of Eq. (3.23). The dotted line denotes the unique wave number k_d selected by dislocations.

the mean wave numbers calculated in a previous experiment [56, 57] performed in a cylindrical cell with $\Gamma = 78$ and $\sigma = 0.95$ (diamonds) are also included. At lower Rayleigh numbers, the mean wave numbers from the direct numerical simulations agree with the experimental findings. However, at higher Rayleigh numbers, the wave numbers from the simulations are smaller than those of the experiments. Presumably, the smaller aspect ratios used in the simulations mean that their wave numbers are affected by finite size effects.

For the range $0.6 \leq \epsilon \leq 1.2$, the mean wave numbers of the stripes with angular bends when mean flow is quenched (denoted by the crosses in Fig. 3.10) appear to

fall onto a straight line whose mathematical form can be obtained from a linear fit,

$$\langle k \rangle = (3.14 \pm 0.05) - (0.16 \pm 0.06)\ \epsilon. \tag{3.22}$$

This relation is consistent with the wave numbers selected by focus-type singularities at Prandtl number $\sigma = 1$ [13, 14],

$$k_f = 3.117 - 0.13\ \epsilon. \tag{3.23}$$

The local pattern in focus-selected convection includes rolls that form closed contours about a point within the cell. In the rectangular geometries of the direct numerical simulations, the four corners act as focus centers, as can be seen by the presence of approximately axisymmetric roll patches emanating from the corners, see Fig. 3.4(a). In the absence of mean flow, the wave number selected therefore appears to be dominated by that selected by the focus centers (i.e., the corners) to give a mean wave number consistent with that selected in focus-type singularities.

Furthermore, in the absence of mean flow, the wave numbers k_f lie at the boundary of the zig zag instability [29]. The patterns observed with mean flow quenched are thus dominated by lateral "zig and zag" bendings, leading to the stripes with angular bends observed in Figs. 3.4(b) and 3.8(b).

The correlation length $\xi(\epsilon)$ of the patterns can also be computed as a function of the reduced Rayleigh number ϵ. In Fig. 3.11, $\xi(\epsilon)$ is plotted for both unquenched patterns (circles) and for patterns observed when the mean flow is quenched (crosses). For comparison purposes, the correlation lengths calculated from a previous experiment [56, 57] performed in a cylindrical cell with $\Gamma = 78$ and $\sigma = 0.95$ (diamonds) are included. The correlation lengths for the states when mean flow is quenched are, on the average, about twice as large as those for spiral defect chaos at all values of ϵ. In addition, the correlation lengths for the unquenched patterns can be fitted with the power law $\xi \propto \epsilon^{-1/2}$. However, the same cannot be said for the quenched states. In fact, the data suggests that while an exponent of $-1/2$ might be fitted for $\epsilon \gtrsim 0.7$, the

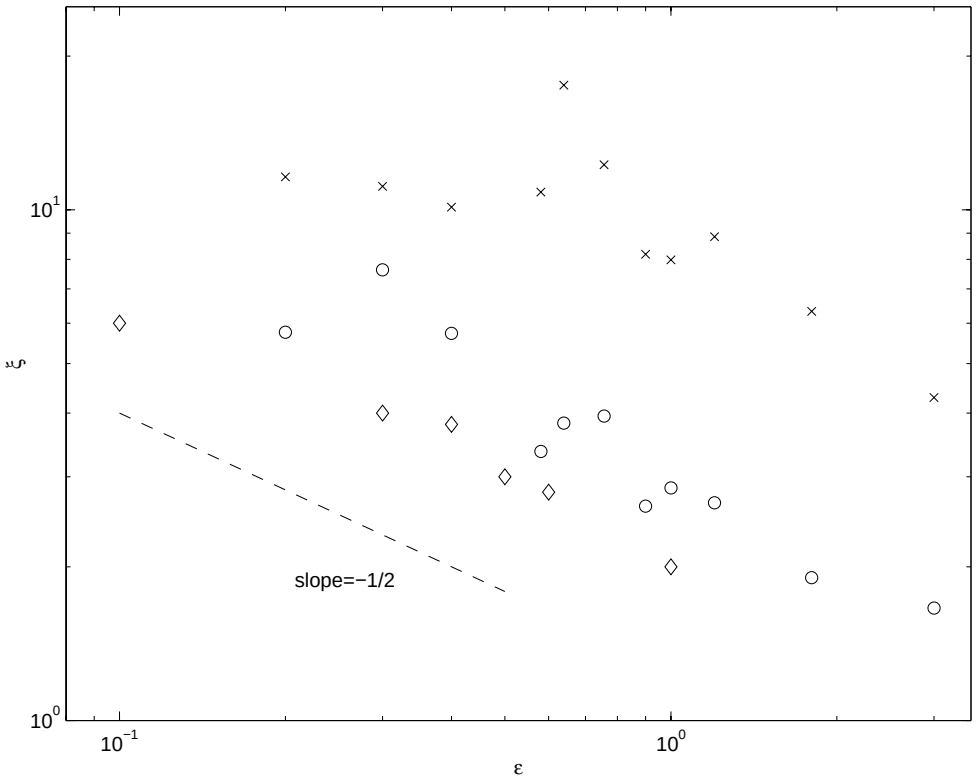

Figure 3.11: Correlation length ξ vs. reduced Rayleigh number ϵ. The symbols are as defined in Fig. 3.10. The dashed line corresponds to the power law $\xi \propto \epsilon^{-1/2}$.

correlation lengths appear to have saturated at $\xi \sim \Gamma = 14$ for $\epsilon \lesssim 0.7$. This suggests that finite size effects become important, and that, in order to obtain a better estimate of the scaling relation for the patterns observed when mean flow is quenched, a larger aspect ratio would be needed. Owing to the lack of data over more decades of reduced Rayleigh numbers, actual fits to the data were not carried out.

3.3.5 Curvature distributions

How much the quenching of the mean flow straightens the rolls can be quantified by looking at the distribution of the local curvature χ, defined at every point in the planform to be the magnitude of the divergence of the unit wave vector:

$$\chi = |\nabla \bullet \widehat{k}|. \tag{3.24}$$

A value of $\chi = 0$ corresponds to a straight roll, whereas a value of $\chi = 1$ corresponds to a roll with a radius of curvature of unity.

The probability density function $P(\chi)$ for spiral defect chaos observed at $\epsilon = 1.0$, $\sigma = 1$, and $\Gamma_x = \Gamma_y = 20$ are computed, as well as for the resulting stripes with angular bends observed at 10 time units after mean flow is quenched. In Fig. 3.12, the two distributions are plotted. The curvature distribution for spiral defect chaos (solid line) peaks at a value of $\chi \approx 0.1$, suggesting that the pattern is dominated by spirals whose radius of curvature is $\chi^{-1} \sim 10$, consistent visually with the pattern shown in Fig. 3.4(a). This peak broadens to become a plateau at $0 \lesssim \chi \lesssim 0.1$ for the quenched state (dashed line), suggesting an increase in the dominance of straighter rolls in the pattern.

Similar results are also observed for the comparison of the curvature distribution for the stripe textures. In Fig. 3.13, the comparisons for a state at $\epsilon = 0.15$ is shown. Both distributions, with (solid line) and without (dashed line) mean flow decrease approximately monotonically and rapidly with increasing χ. Both the comparisons for spiral defect chaos and for stripe textures suggest that the consequence of quenching mean flow is to straighten out the rolls.

In addition, the distribution at $\epsilon = 0.15$ for the quenched case is higher for $\chi \lesssim 0.05$ as well as for $0.1 \lesssim \chi \lesssim 0.4$ (see the inset of Fig. 3.13), and lower otherwise. This suggests that another consequence of quenching mean flow is the development of angular structures that have large curvatures.

3.3.6 Mean flow and lateral boundaries

In experiments where the Rayleigh number is sufficiently high, it has been frequently observed that convection rolls terminate perpendicularly into the lateral walls. In this section, it is shown that mean flow generated by amplitude gradients near lateral walls can be used to explain this phenomenon, although the applicability of this argument rests on a number of factors, among them the presence of defects which affects the ability of the patterns to reorient themselves.

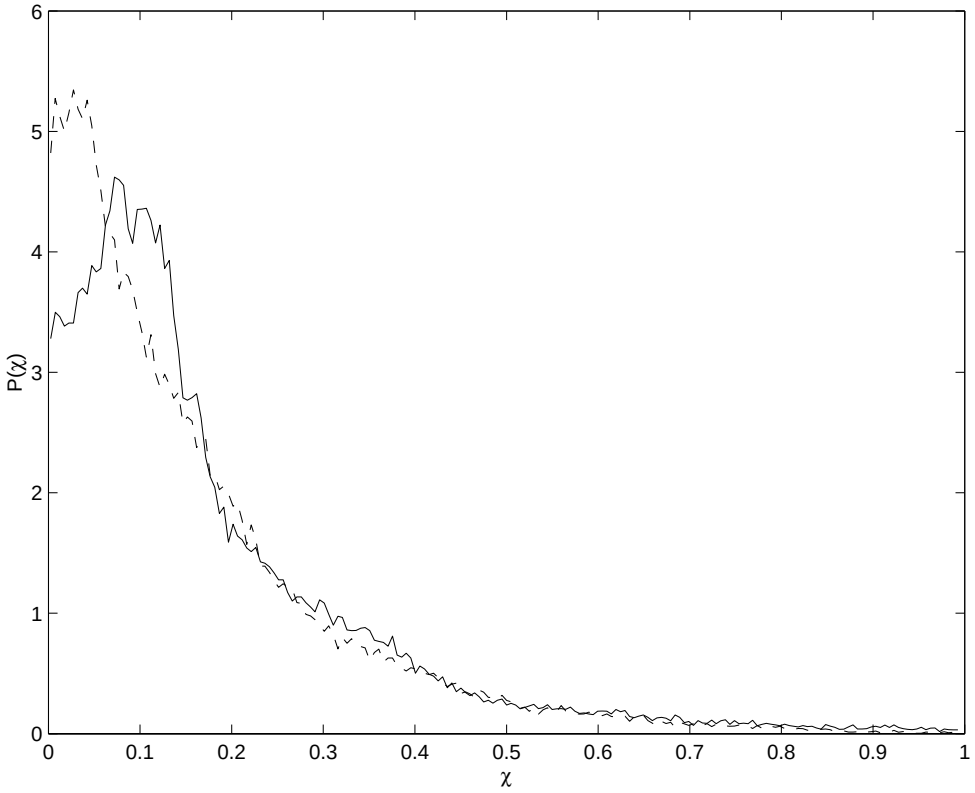

Figure 3.12: The probability density function $P(\chi)$ of the curvature χ. The solid line is for the spiral defect chaotic state at $\epsilon = 1.0, \sigma = 1$, and $\Gamma_x = \Gamma_y = 20$ averaged over different random initial conditions and times $t = 400$ to 500. The dashed line is for the stripes with angular bends observed at 10 time units after mean flow has been quenched.

If $\widehat{n}$ is the outward unit vector normal to the lateral boundary and $\widehat{k}$ the wave director of the rolls, then the wall-roll obliqueness angle can be defined as

$$\Theta \equiv \arccos |\widehat{k} \bullet \widehat{n}|. \tag{3.25}$$

In practice, the numerical value of Θ at a particular location along the lateral boundary is obtained by averaging Eq. (3.25) over a length $r = 0.5$ to $r = 1.5$, where r is the perpendicular distance away from that location along the lateral boundary. The value $\Theta = \pi/2$ corresponds to rolls terminating perpendicularly into the walls. The common occurrence of this value remains a phenomenological observation, without

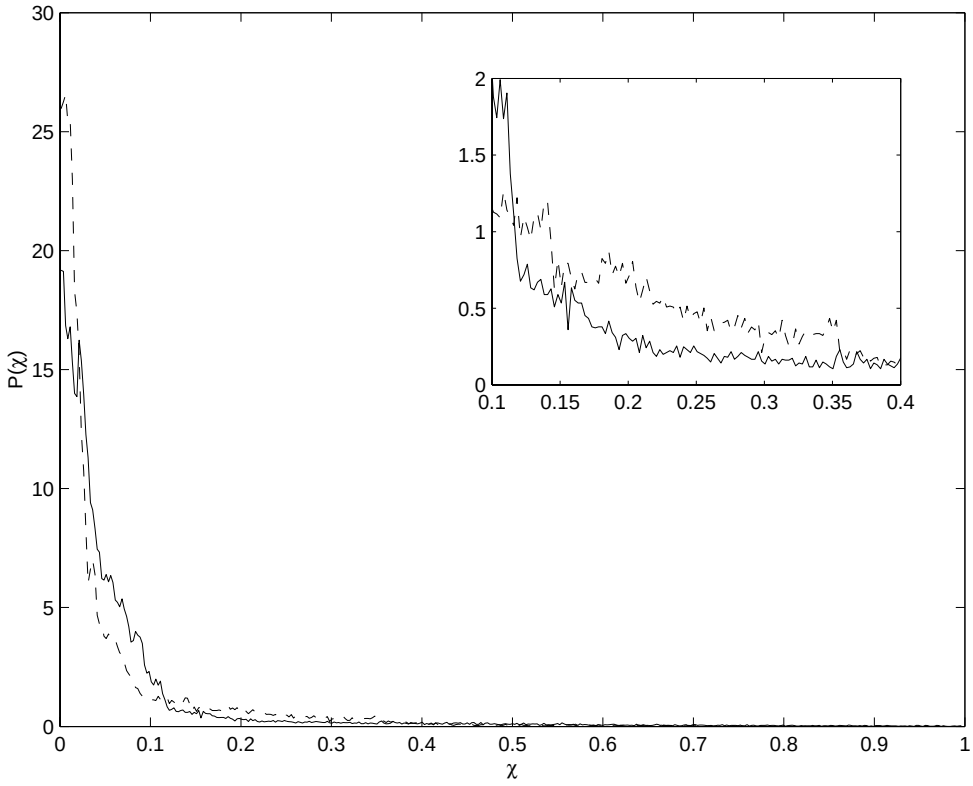

Figure 3.13: The probability density function $P(\chi)$ of the curvature χ. The solid line is for stripe textures at $\epsilon = 0.15, \sigma = 1$, and $\Gamma_x = \Gamma_y = 20$ averaged over different random initial conditions and times $t = 400$ to 500. The dashed line is for the stripes with angular bends observed at 10 time units after mean flow has been quenched. The inset shows the region $0.1 \leq \chi \leq 0.4$ enlarged.

much theoretical underpinning, although it has been found [24] that Θ is not fixed by the physical boundary conditions, Eqs. (1.11)–(1.13).

However, when rolls do not terminate perpendicularly at a lateral boundary, variations in the amplitude of the convection rolls as it decays near the lateral boundaries results in the generation of a mean flow. [Recall from Eq. (3.1) that a mean flow is generated by inhomogeneities in the wave numbers and amplitudes of the convection rolls.] This mean flow then tends to restore the rolls back to being perpendicular to the lateral boundary. The various quantities used in this section are defined in the sketch in Fig. 3.14.

For simplicity, the wave vectors of the rolls are assumed to be constant near the

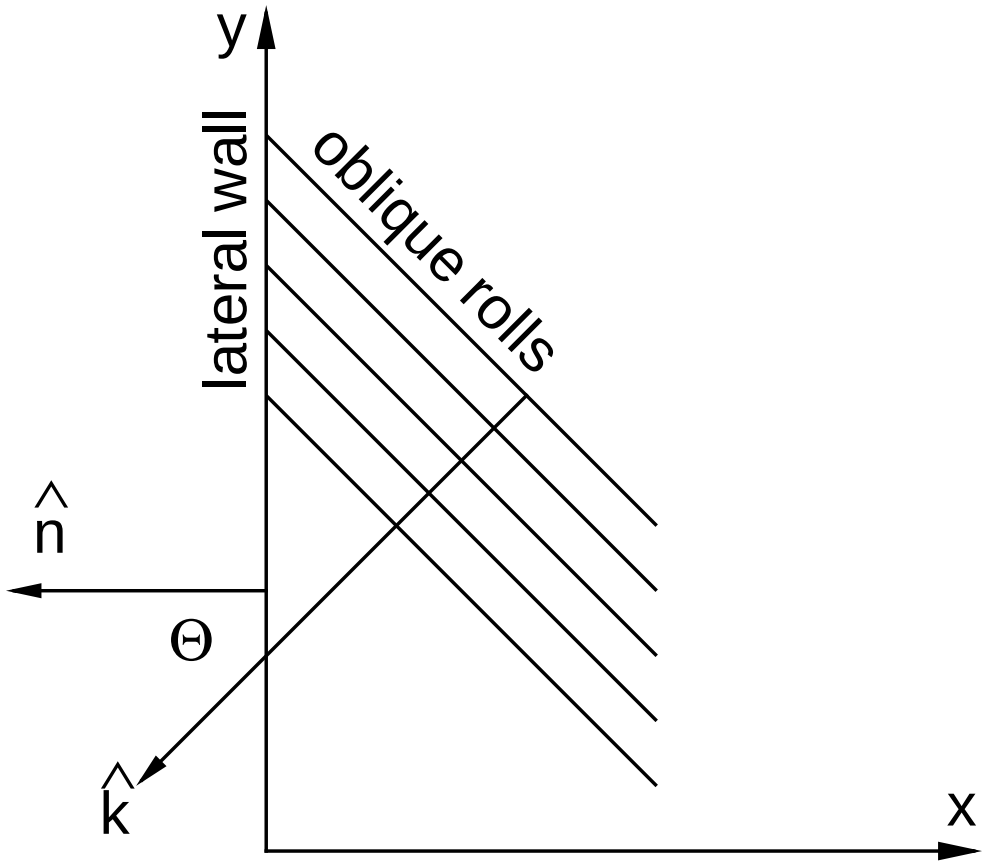

Figure 3.14: Straight and parallel convection rolls with wave director $\widehat{k}$ terminating at a lateral boundary with outward normal $\widehat{n}$ at an angle of obliqueness Θ. Note that, by definition, $0 < \Theta < \pi/2$. The perpendicular distance away from the lateral wall is x.

lateral boundary,

$$\mathbf{k} = (-k\cos\Theta, -k\sin\Theta). \tag{3.26}$$

(If the assumption that the wave numbers of the rolls are constant is relaxed, then the compression and dilation of the rolls as well as inhomogeneities in their curvatures will also contribute to the mean flow.) In addition, the convection amplitude within a correlation length ξ of a lateral boundary is assumed to be suppressed [27, 100]:

$$A(x,y) = A_0 \tanh\left(\frac{x}{\xi\cos\Theta}\right). \tag{3.27}$$

The quantity A_0 is the amplitude in the bulk. The correlation length $\xi = \sqrt{2}\epsilon^{-1/2}\xi_0$ with $\xi_0 = 0.385$. The variable x is the perpendicular distance away from the lateral boundary.

Then, from the Cross-Newell equation [29], the amplitude gradients near the lateral wall will result in a non-zero mean flow vorticity, ω, given by

$$\omega = \gamma \hat{z} \bullet \nabla_\perp \times [\mathbf{k}\nabla_\perp \bullet (\mathbf{k}A^2)], \tag{3.28}$$

where γ is a constant that is inversely proportional to the Prandtl number σ. Substituting Eqs. (3.26) and (3.27) into Eq. (3.28) then gives

$$\omega(x) = 2\gamma A_0^2 k^2 \xi^{-2} f(\Theta, x) \tag{3.29}$$

where the normalized mean flow vorticity,

$$f(\Theta, x) = \tan(\Theta)\mathrm{sech}^2\left(\frac{x}{\xi\cos\Theta}\right) \times \left[1 - 3\tanh^2\left(\frac{x}{\xi\cos\Theta}\right)\right] \tag{3.30}$$

is plotted in Fig. 3.15(a) for several representative values of Θ. The mean flow vorticity ω is positive for $x/\xi \lesssim 1$, and negative otherwise. The currents from this vorticity pair will then drive the rolls back to a perpendicular orientation.

The mean flow generated by this vorticity can also be easily computed. Along the lateral wall, it is given by

$$|\mathbf{U}| = \gamma |\mathbf{k}_y| \nabla_\perp \cdot (\mathbf{k}A^2). \tag{3.31}$$

(The component of the mean flow normal to the lateral wall is cancelled by the flow coming from the slow pressure gradient.) Using Eqs. (3.26) and (3.27),

$$|\mathbf{U}| = 2\gamma A_0^2 k^2 \xi^{-1} g(\Theta, x) \tag{3.32}$$

where the normalized restoring mean flow magnitude in the direction of the lateral

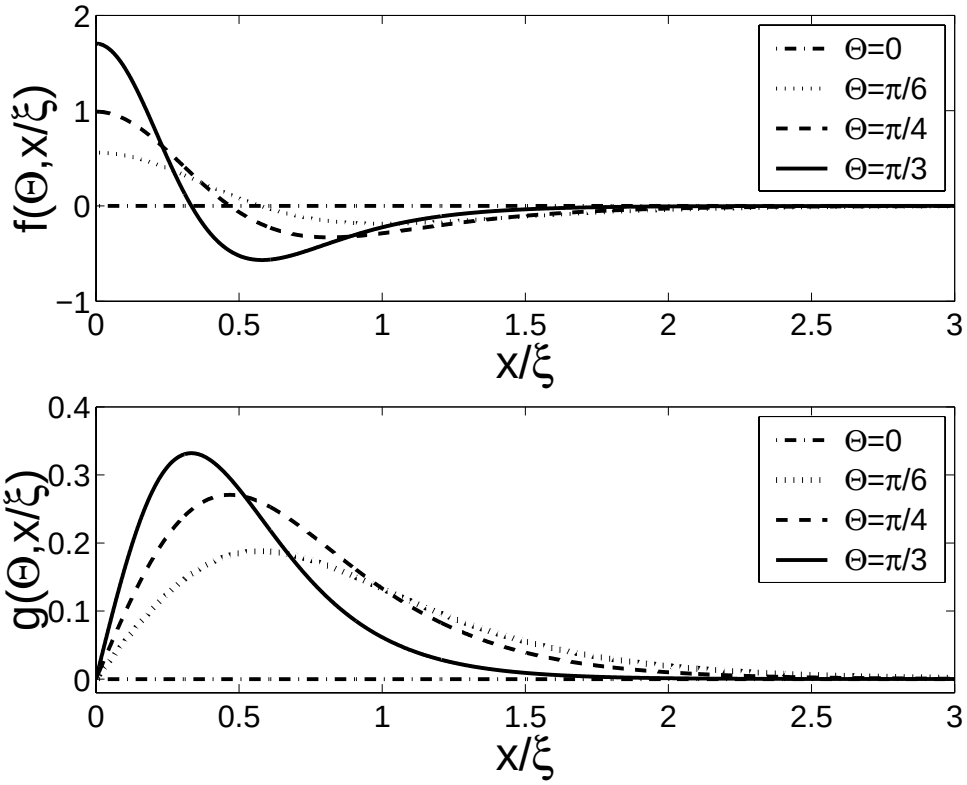

Figure 3.15: *(a)* The function $f(\Theta, x)$ defined in Eq. (3.30) which is the normalized vertical component of the mean flow vorticity. It is plotted here for several values of Θ and vs. x/ξ. *(b)* The function $g(\Theta, x)$ defined in Eq. (3.33) which is the normalized mean flow magnitude. It is plotted here for several values of Θ and vs. x/ξ.

wall,

$$g(\Theta, x) = \sin(\Theta)\mathrm{sech}^2\left(\frac{x}{\xi\cos\Theta}\right)\tanh\left(\frac{x}{\xi\cos\Theta}\right) \tag{3.33}$$

is plotted in Fig. 3.15(b) for several representative values of Θ.

Finally, the quantity $\max|\mathbf{U}|$ as a function of Θ is plotted in Fig. 3.16. The restoring mean flow magnitude grows monotonically from zero at $\Theta = 0$ (corresponding to sets of rolls parallel to the lateral wall) to attain its largest value at $\Theta \to \pi/2$ (corresponding to sets of rolls perpendicular to the wall). This analysis actually breaks down for $|\Theta - \pi/2| \lesssim \epsilon^{1/4}$ because modifications at the next order in Eq. (3.27) become important [24].

The importance of this restoring mean flow in ensuring that the rolls terminate

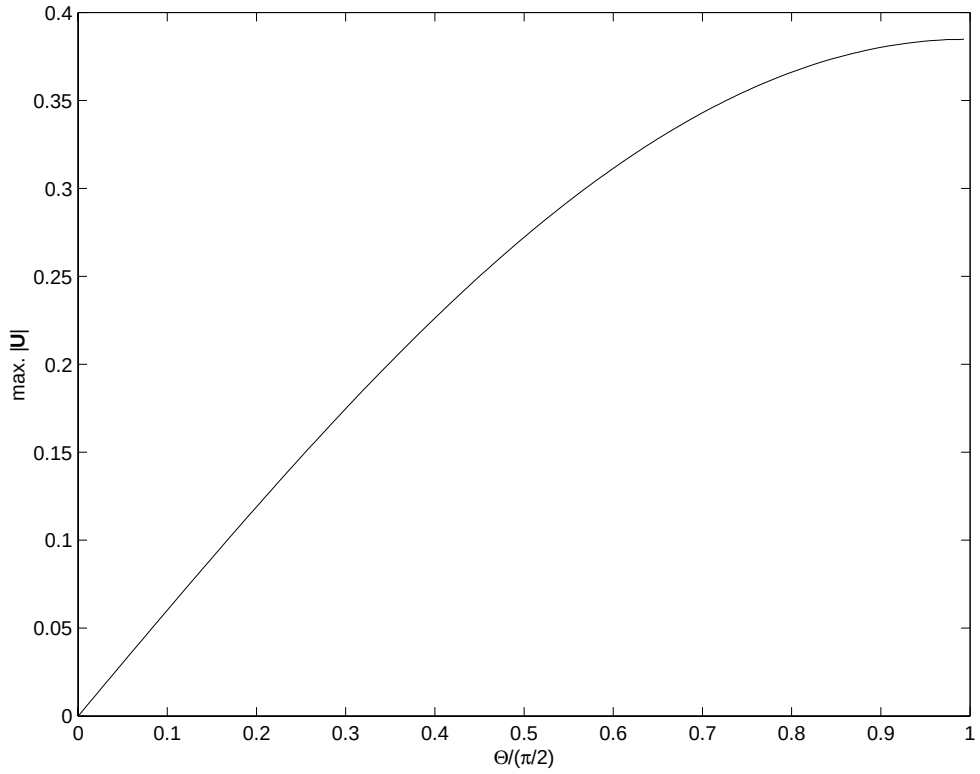

Figure 3.16: The maximum magnitude of the mean flow $\mathbf{U}$ as a function of the wall-roll obliqueness angle Θ. It increases monotonically from zero at $\Theta = 0$ (rolls parallel to the wall).

perpendicularly is indicated by observing that, in the absence of mean flow, oblique rolls are more prevalent. In Fig. 3.17, the wall-roll obliqueness angle averaged over the lateral boundaries is plotted for planforms observed at $t = 500$ at various reduced Rayleigh number ϵ, the Prandtl number $\sigma = 1$, and in a rectangular cell of aspect ratio $\Gamma_x = \Gamma_y = 20$, with mean flow and with the mean flow quenched. With mean flow, the rolls are close to perpendicular, $\Theta \approx \pi/2$. However, when mean flow is quenched, the rolls are more oblique, $\Theta \lesssim \pi/2$. In fact, the difference in the mean wall-roll obliqueness angle between the states with mean flow and with mean flow quenched, $\Delta\langle\Theta\rangle$, increases approximately linearly with ϵ,

$$\Delta\langle\Theta\rangle = (0.16 \pm 0.01)\epsilon, \tag{3.34}$$

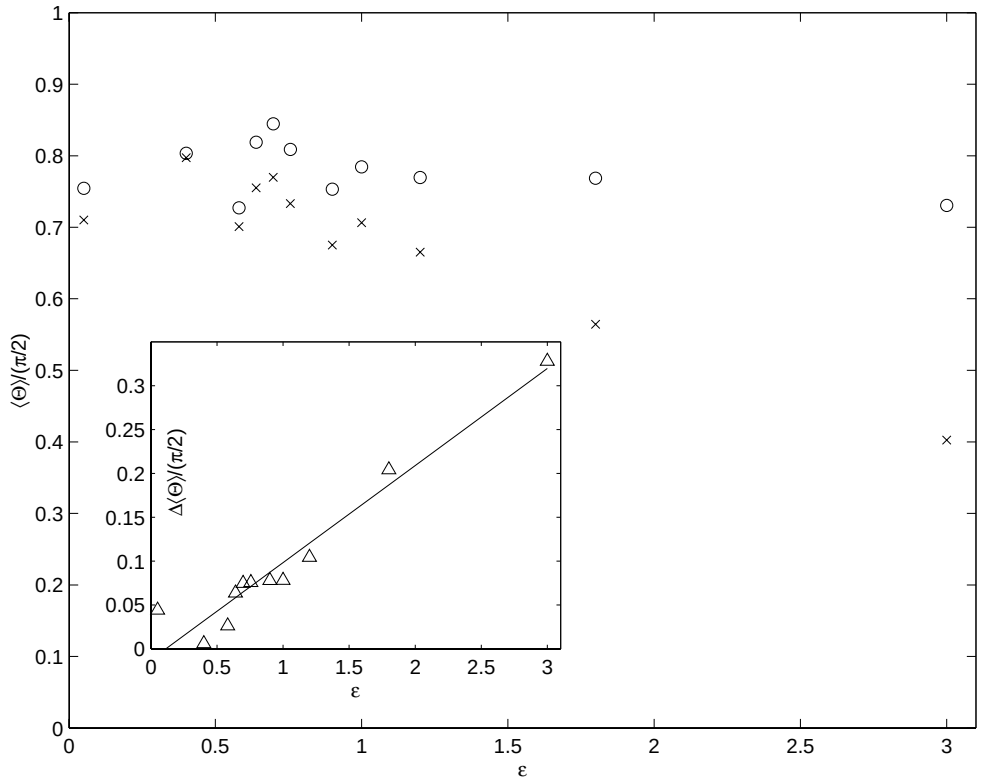

Figure 3.17: The mean wall-roll obliqueness angle $\langle\Theta\rangle$ as a function of the reduced Rayleigh number ϵ for states with mean flow (circles) and with mean flow quenched (crosses). The inset shows the difference between the two sets of data, $\Delta\langle\Theta\rangle$, as a function of ϵ.

as the inset of Fig. 3.17 depicts.

When mean flow is quenched, the reorientation of the rolls away from $\Theta = \pi/2$ is almost instantaneous. This result is illustrated in Fig. 3.18 for one particular reduced Rayleigh number, $\epsilon = 1.0$. In this case, the mean flow quenching takes place at time $t = t_q = 500$. At time $t = 500$, the mean wall-roll obliqueness angle moves away from $\Theta = \pi/2$ in a time scale of $\mathcal{O}(1)$.

The above argument that mean flow restores the rolls to a perpendicular orientation may not always be applicable. Two scenarios are presented here. First, when the simulations are performed in a cylindrical cell of aspect ratio $\Gamma = 30$, it is found that, at $\epsilon = 1.0$, the mean wall-roll obliqueness angle $\langle\Theta\rangle$ still remains close to $\pi/2$ when mean flow is quenched. This can be seen more clearly in Fig. 3.19, where the

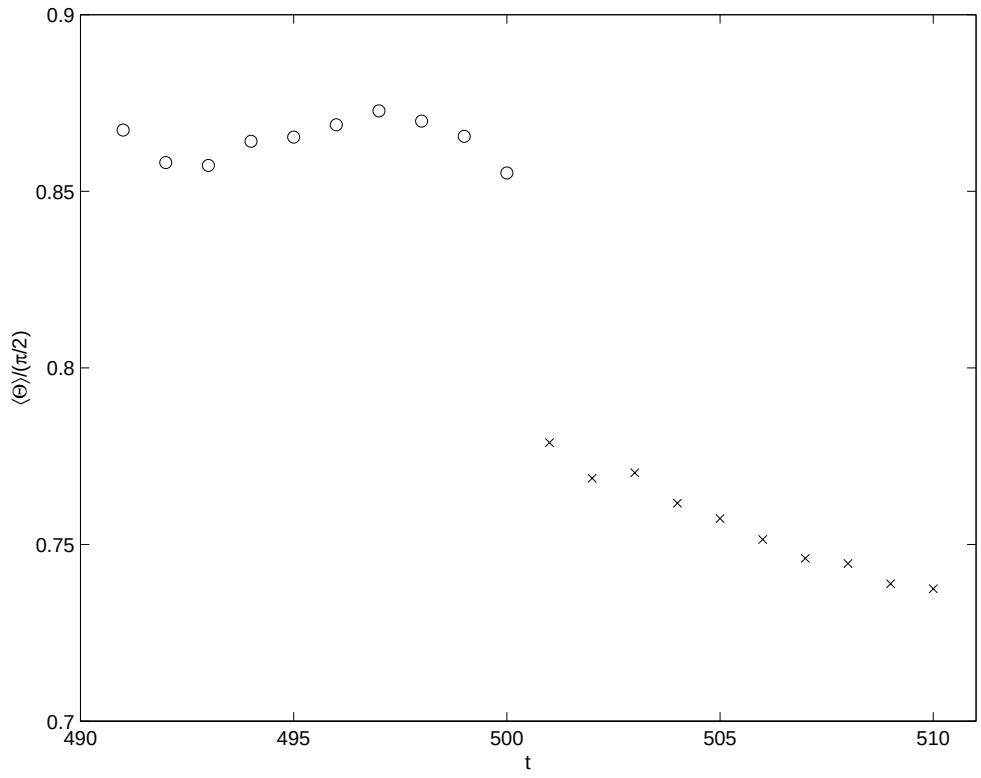

Figure 3.18: The change in the mean wall-roll obliqueness angle $\langle\Theta\rangle$ as a function of time, averaged over different random initial conditions. The parameters here are $\epsilon = 1.0$, $\sigma = 1$, and $\Gamma_x = \Gamma_y = 20$. Mean flow quenching takes place at time $t = t_q = 500$, so that, for $490 \leq t \leq 500$, the mean wall-roll obliqueness angle is for a pattern whose bulk dynamics exhibits spiral defect chaos, whereas for $500 \leq t \leq 510$, the bulk dynamics is made up of stripes with angular bends.

probability density $P(\Theta)$ of wall-roll obliqueness angles along the lateral boundaries is shown for states observed in a rectangular cell of aspect ratio $\Gamma_x = \Gamma_y = 20$ and cylindrical cell of aspect ratio $\Gamma = 30$. In a cylindrical cell with mean flow quenched, the peak at $\Theta \approx \pi/2$ is still observed after the mean flow has been quenched. One possible explanation might be that, in a cylindrical cell, there are more defects existing near the lateral boundaries and that these defects then pin the rolls, preventing them from reorienting away from $\Theta = \pi/2$ when the mean flow is quenched.

A second scenario where the above argument does not apply is at low Rayleigh numbers. From Eq. (3.32), the magnitude of the mean flow $|\mathbf{U}| \propto \epsilon^{1/2}$ so that at low Rayleigh numbers, the mean flow may not be strong enough to reorient the rolls

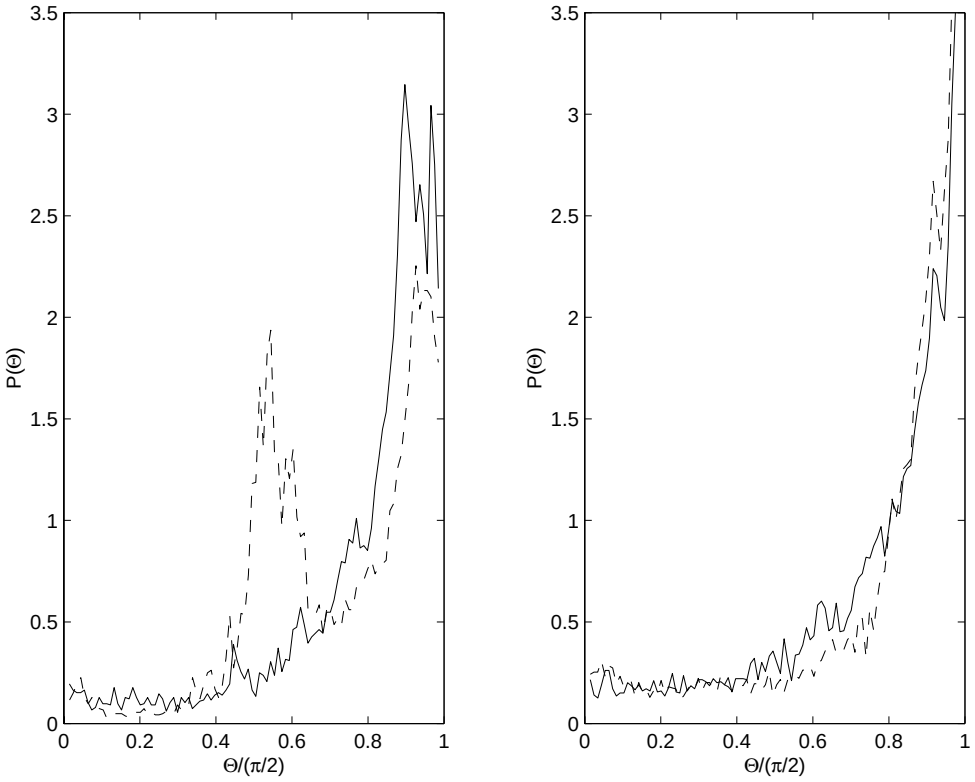

Figure 3.19: *(a)* Distribution of angles that rolls terminate at a lateral boundary in a rectangular cell of aspect ratio $\Gamma_x = \Gamma_y = 20$. The solid line shows the distribution for the spiral defect chaotic state averaged over different initial conditions at $\epsilon = 1.0$ and $\sigma = 1$. The dashed line shows the distribution for the state with mean flow quenched. *(b)* The solid line shows the distribution for spiral defect chaos observed in a cylindrical cell of aspect ratio $\Gamma = 30$ at $\epsilon = 1.0$ and $\sigma = 1$. The dashed line shows the distribution for this state but with mean flow quenched.

perpendicularly. This is evident in Fig. 3.8(a), where, at the reduced Rayleigh number $\epsilon = 0.15$, rolls are seen to terminate with an acute angle at the lateral walls. In this case, the presence of a restoring mean flow can also be visualized. The mean flow vorticity plot corresponding to this pattern, shown in Fig 3.20(a), shows the presence of strong vorticity along the bottom half of the left wall and the top half of the right wall. There, the restoring mean flow vorticity takes the form of long and narrow circulating "jets" that are about one roll size wide and several roll sizes long. In Fig. 3.20(b), the vorticity is plotted as a function of distance away from the lateral wall along the solid and dashed horizontal lines shown in Fig. 3.20(a). The existence

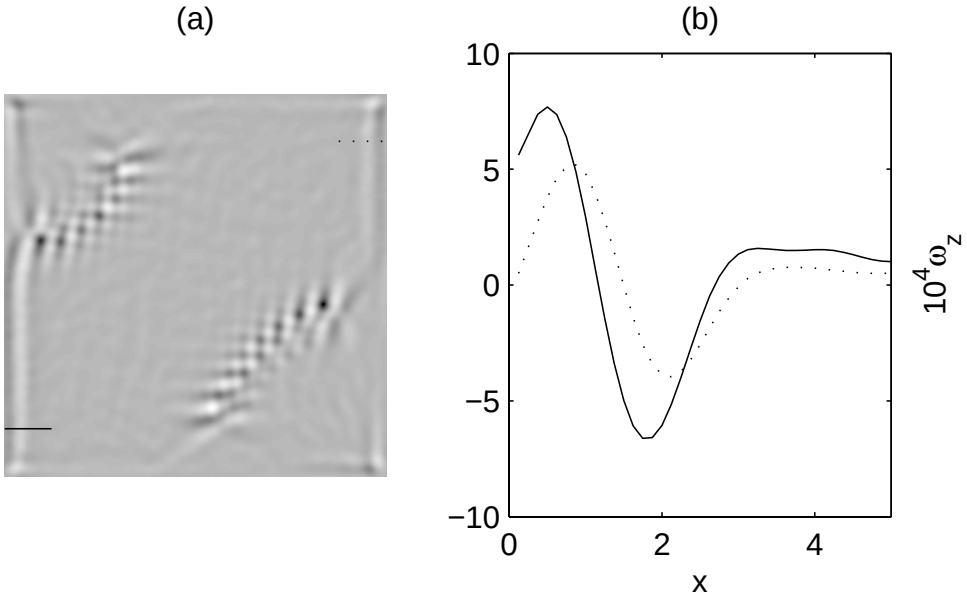

Figure 3.20: *(a)* The mean flow vorticity $\omega_z(x, y)$ corresponding to the stripe texture of Fig. 3.8(a) obtained using Eq. (3.7). Light regions correspond to positive vorticity, dark regions to negative vorticity. The important feature in this vorticity map is the presence of "jet"-like structures along the bottom half of the left wall and the top half of the right wall. *(b)* The vorticity $\omega_z(x)$ is plotted along the solid and the dashed horizontal lines shown in (a). The shape of $\omega_z(x)$ is to be compared with the plot of $f(\Theta, x/\xi)$ in Fig. (3.15), where a positive and a negative vorticity patch sets up a restoring mean flow.

of a positive vorticity patch close to the wall and a negative patch further away from the wall, which together indicates the presence of a restoring mean flow, agree qualitatively with the theoretical results $f(\Theta, x/\xi)$ in Fig. 3.15. When the Rayleigh number of the state in Fig. 3.8 is increased from $\epsilon = 0.15$ to $\epsilon = 1.0$, the mean flow becomes strong enough to reorient the rolls to become perpendicular to the lateral walls, and subsequently disappears.

3.4 Conclusions

In this chapter, a procedure to construct a modified velocity field that does not have any mean flow in a convecting flow is first described. This procedure is then used

to show that spiral defect chaos does not survive when the mean flow is quenched. Instead, a pattern characterized by textures of stripes with angular bends appears. The mean wave numbers of these quenched patterns approach those selected by focus-type singularities, which, in the absence of the mean flow, lie at the boundary of the zig zag instability.

In addition, a heuristic argument on how the mean flow can contribute to rolls terminating into a lateral boundary perpendicularly. Data is provided to show that, in the absence of the mean flow, the rolls begin to deviate from a perpendicular orientation, and this obliqueness increases with the Rayleigh number. However, the ability of this mean flow to restore the rolls to a perpendicular orientation may be impeded by the presence of defects that do not allow the rolls to reorient themselves, and at low Rayleigh numbers where the restoring mean flow is weak.

Chapter 4

Transport of passive tracers in spiral defect chaos

4.1 Introduction

This chapter addresses the transport of passive neutrally buoyant tracers in Rayleigh-Bénard convection exhibiting spiral defect chaos. As mentioned in Chap. 1, spiral defect chaos is an example of spatiotemporal chaos that is characterized by disorder in both space and time [28, 39, 43]. An important characteristic of such spatially disordered flows is that fluctuations in space play a significant role in their dynamics, resulting in non-trivial advection of the passive tracers. The transport of passive tracers is governed by this non-trivial advection in addition to molecular diffusion arising from collisions between tracers or thermal fluctuations. The goal of this chapter is to understand the net transport of passive tracers as a function of these two competing mechanisms. This is a problem that is of considerable importance in many branches of science and engineering. For example, it may allow one to gain insight into heat and mass transport in atmospheric and oceanic flows and also in chemical engineering processes such as combustion.

Previous studies of the properties of passive transport in convective flows have focused on the following regimes: laminar and time-independent, and oscillatory and weakly time-dependent, but not spatiotemporal chaotic. For example, in two-dimensional time-independent laminar Rayleigh-Bénard convection flow, experiments

have shown that the transport is effectively diffusive in the long time limit, with an effective diffusivity that is greater than the molecular diffusivity by a factor that scales as the square root of the Péclet number (defined in Eq. (4.5) to be the ratio of the strength of advection to diffusion) [84]. This enhancement, in the large Péclet number limit, has also been calculated theoretically using the matched asymptotic expansion method [74, 80]. In addition, higher-order corrections to the diffusion process, for arbitrary Péclet numbers, have been calculated numerically using the homogenization method [53, 54]. For nearly two-dimensional time-periodic convection, experiments near the onset of the oscillatory instability [15] have shown that the transport is again effectively diffusive but with an effective diffusivity that depends linearly on the local amplitude of the roll oscillations [83]. This result has also been confirmed theoretically by which the invariant structures of the flow were identified that acted as templates for the motion of the tracers [17, 18]. Passive tracer transport has also been studied in other types of laminar flows, including capillary waves generated by the Faraday instability [72, 73] and Taylor-Couette flow in a rotating annulus [85, 86]. In addition, the subject of passive tracer diffusion in turbulent flows is also a subject that has been extensively investigated [55, 81]. Experimentally, in Taylor-Couette flow, the effective diffusivity has been measured to vary linearly with the scale of the Taylor vortices [91]. Theoretically, mean transport quantities have been calculated as averages over ensembles of the velocity field. The latter is usually evaluated with the supplement of approximate closure schemes.

4.2 Definitions

The transport of passive neutrally buoyant tracers in a flow can be described by the advection-diffusion equation. Written in a dimensionless form, it is

$$(\partial_t + \mathbf{u} \bullet \nabla)\psi(x, y, z, t) = L\nabla^2\psi. \tag{4.1}$$

The scalar field $\psi(x, y, z, t)$ is the passive tracer concentration at point (x, y, z) and time t. The velocity field $\mathbf{u}$ is obtained from solving the Boussinesq equations, Eqs. (1.5)–(1.7). The parameter L is the Lewis number, defined to be the molecular diffusivity D of the tracers made dimensionless by the thermal diffusivity κ of the fluid,

$$L = \frac{D}{\kappa}. \tag{4.2}$$

In this chapter, small Lewis numbers in the range $10^{-3} \leq L \leq 10^{-1}$ will be considered. In comparison, the Lewis numbers of passive tracers used in previous convection experiments [84] in water at approximately 300 K, namely micrometer-sized latex spheres (vinyl toluene t-butylstyrene) and methylene blue dye, are $L = 1.2 \times 10^{-5}$ and $L = 3.9 \times 10^{-3}$, respectively.

The tracers are assumed to be passive, i.e., their motions in the fluid do not modify the fluid's velocity field. The Soret and Dufour effects are also assumed to be negligible. The former refers to the additional passive tracer concentration current driven by gradients of the temperature field, whereas the latter refers to the additional heat current driven by gradients of the passive tracer concentration. In addition, the lateral walls are assumed to be impermeable to the tracers, so that

$$\widehat{n} \bullet \nabla\psi = 0, \quad \text{on lateral walls}, \tag{4.3}$$

where $\widehat{n}$ is the unit vector perpendicular to the lateral walls at a given point.

Eq. (4.1) is also commonly written in the literature in an alternate but entirely equivalent form. By dividing it throughout by a characteristic velocity scale $||\mathbf{u}||$, Eq. (4.1) becomes

$$(\partial_t + \tilde{\mathbf{u}} \bullet \nabla)\psi(x, y, z, t) = \frac{1}{P}\nabla^2\psi, \tag{4.4}$$

with $\tilde{\mathbf{u}}$ the rescaled velocity field, and P the Péclet number, defined to be the ratio of the relative importance of the advection of the tracers to their molecular diffusion,

$$P = \frac{||\mathbf{u}||}{L}. \tag{4.5}$$

Finally, it should also be noted that instead of studying the passive tracer concentration field χ in the space coordinates defined in the laboratory frame (the Eulerian approach), one could also study the trajectories of each passive tracer individually (the Lagrangian approach) by integrating, for each passive tracer,

$$\frac{d\mathbf{x}(t)}{dt} = \mathbf{u}(\mathbf{x}(t), t) + \eta(t), \tag{4.6}$$

where $\mathbf{x}(t)$ is the position of the tracer [initially at $\mathbf{x}(0)$], $\mathbf{u}$ is the Eulerian velocity field at space $\mathbf{x}(t)$ and time t, and $\eta(t)$ is a Langevin noise introduced to represent molecular diffusion. However, this approach is not pursued in this chapter because of the difficulties associated with integrating Eq. (4.6). In fact, even if the velocity field $\mathbf{u}$ can be explicitly determined and has a very simple form, the tracer trajectories $\mathbf{x}$ can have very complicated dynamics [3].

4.3 Results

The transport equation, Eq. (4.1), is integrated concurrently with the Boussinesq equations, Eqs. (1.5)–(1.7), for the following parameters: the Rayleigh number ranging from the onset of spiral defect chaos at $R \approx 3000$ to fully developed spiral defect chaos at $R \approx 4000$, the Prandtl number $\sigma = 1$, and the Lewis number ranging from $L = 10^{-3}$ to $L = 10^{-1}$. The direct numerical simulations have been performed in both cylindrical and rectangular three-dimensional cells of various aspect ratios using both the `boxcode` and `nek5000` solvers. In this chapter, data from a cylindrical cell of aspect ratio $\Gamma = 30$ will be reported. The initial condition used for the passive tracer concentration field is a localized concentration at the center of the cell:

$$\psi(x, y, z, t = 0) = \exp\left[-\frac{x^2 + y^2 + z^2}{6\Delta^2}\right], \tag{4.7}$$

with $\Delta = 0.25$ a small constant to ensure that the passive tracer concentration is initially localized. At time $t = 0$, the temperature, velocity, and pressure fields correspond to an asymptotic state of spiral defect chaos, i.e., one that has been

evolved from random thermal perturbations up to a time of $\mathcal{O}(\Gamma^2)$. Because the focus is only on cells of large aspect ratio, $\Gamma \gg 1$, the z-dependence of the passive tracer concentration field is found to be essentially constant. As such, the z-dependence will be dropped in subsequent discussions and the passive tracer concentration $\psi(x, y, t)$ will be considered as a function of two-dimensional horizontal space and time.

In Fig. 4.1, the evolution of the passive tracer concentration field $\psi(x, y, t)$ at the mid-plane $z = 0$ for the parameters $R = 3500$, $\sigma = 1$, and $L = 10^{-2}$ is shown for various times t. The passive tracer concentration is seen to spread outwards with time. In Sect. 4.3.1, this spreading is quantified by studying the mean square displacement of the passive tracer concentration field. In Sect. 4.3.2, this spreading is shown to be governed by normal diffusion. In Sect. 4.3.3, the local dependence of the spreading on the wave number is discussed.

4.3.1 Statistics of moments of passive tracer concentration

The spreading of the passive tracers can be quantified by its mean square displacement $V(t)$, or the second moment of the passive tracer concentration field,

$$V(t) = \frac{\int_0^\Gamma \int_0^{2\pi} [r - \bar{r}(t)]^2 \psi(r, \theta, t)\, r\, dr\, d\theta}{\int_0^\Gamma \int_0^{2\pi} \psi(r, \theta, t)\, r\, dr\, d\theta}. \tag{4.8}$$

Here, (r, θ) is the radial coordinate with origin at the center of the cell. In practice, $V(t)$ is computed as the average over different instances (typically three to five) of ψ obtained from different initial conditions of spiral defect chaos, i.e., the velocity, temperature, and pressure fields used at $t = 0$ are different instances of fully-developed spiral defect chaos. The quantity $\bar{r}(t)$ is the center of mass of the tracer distribution,

$$\bar{r}(t) = \frac{\int_0^\Gamma \int_0^{2\pi} r\psi(r, \theta, t)\, r\, dr\, d\theta}{\int_0^\Gamma \int_0^{2\pi} \psi(r, \theta, t)\, r\, dr\, d\theta}. \tag{4.9}$$

In Fig. 4.2, the mean square displacement $V(t)$ is plotted for several different values of the Rayleigh number R and the Lewis numbers $L = 10^{-3}$ and $L = 10^{-2}$. It is found that, in all cases, the mean square displacement $V(t)$ is directly proportional

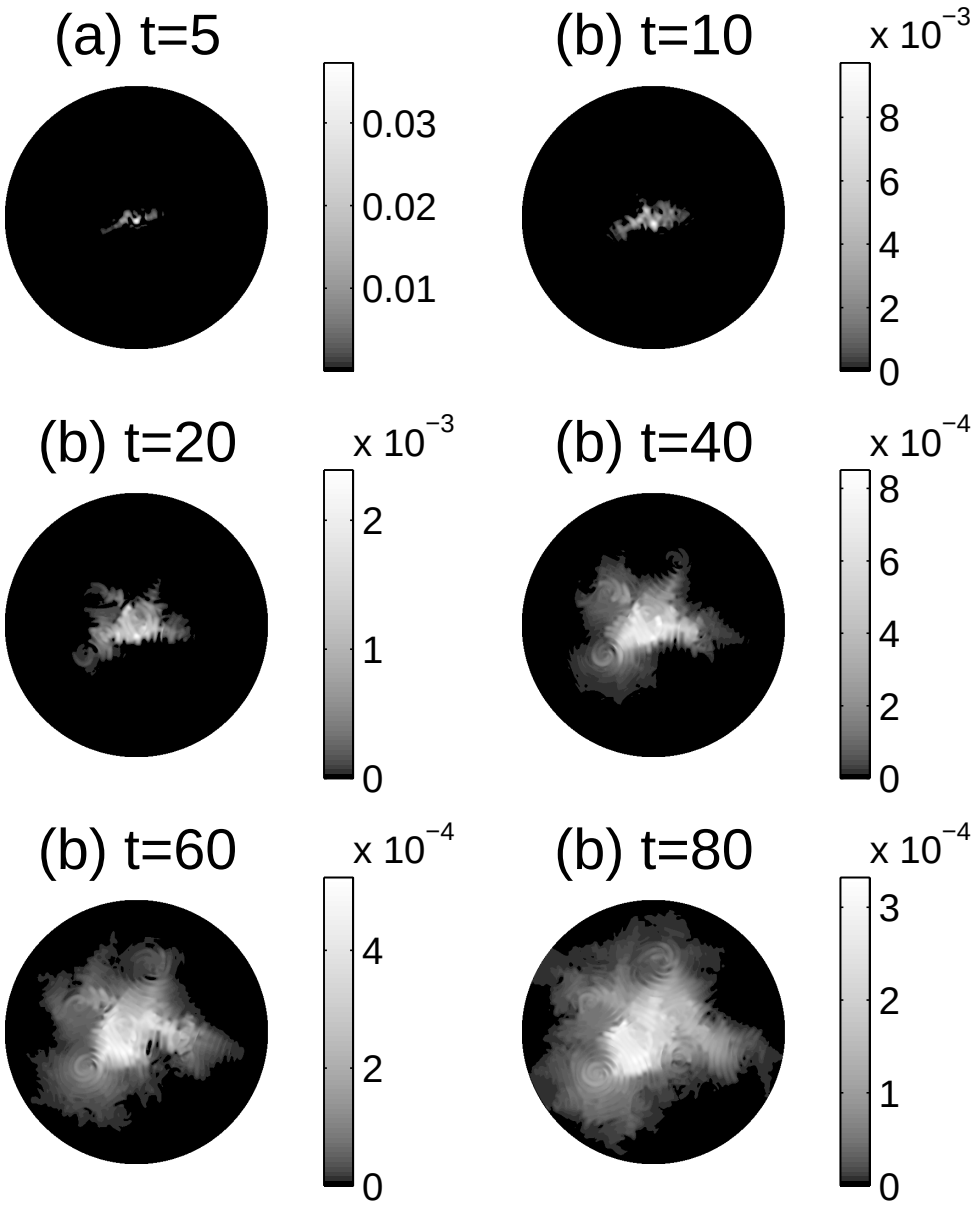

Figure 4.1: Evolution of the passive tracer concentration field $\psi(x, y, z = 0, t)$ for various times t, obtained by numerically solving Eq. (4.1). The Rayleigh number $R = 3500$, the Prandtl number $\sigma = 1$, and the Lewis number $L = 10^{-2}$, and the cylindrical cell has the aspect ratio $\Gamma = 30$. The initial condition for ψ at $t = 0$ is given by Eq. (4.7).

R	γ	
	$L = 10^{-2}$	$L = 10^{-3}$
3074	1.07	1.07
3500	1.04	1.11
4270	1.14	1.14

Table 4.1: The mean square displacement $V(t)$ is fitted to a power law $\sim t^{\gamma}$ for several different values of the Rayleigh number R and Lewis number L. The exponent γ is approximately unity in all instances.

to the time t to a very good approximation. Least squares fits of $V(t)$ to power laws $\sim t^{\gamma}$ yield exponents γ of approximately unity, as shown in Table 4.1. Thus, the spreading of the passive tracer concentration field is described by a normal diffusive process. In other words, the passive tracer concentration when averaged azimuthally, $\bar{\psi}(r,t)$, is described by the one-dimensional normal diffusion equation,

$$\partial_t \tilde{\psi}(r,t) = L^* \partial_{rr} \tilde{\psi} \tag{4.10}$$

with L^* an effective Lewis number. The quantity $(L^* - L)$ is then the increase in the Lewis number of the passive tracer concentration brought upon by the advection of the spiral defect chaotic flow.

The effective Lewis number, L^*, of the resulting one-dimensional normal diffusion of the passive tracer concentration can be extracted from the mean square displacement as

$$V(t) = 4L^* t. \tag{4.11}$$

Several values of the effective Lewis number for various values of the parameters are tabulated in Table 4.2.

In principle, the effective Lewis number will depend on both the properties of the advecting fluid, namely the Rayleigh and Prandtl numbers, as well as the property of the passive tracer concentration, namely, its Lewis number. However, it is found that,

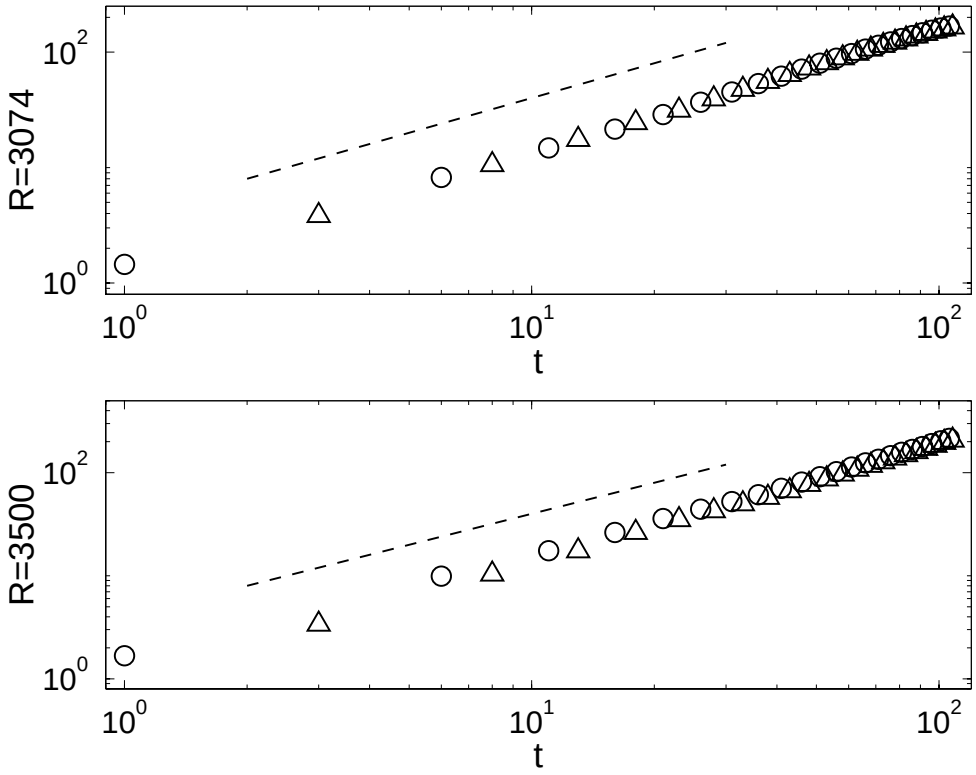

Figure 4.2: The mean square displacement $V(t)$ of the passive tracer concentration field for two different Rayleigh numbers $R = 3074$ (top) and 3500 (bottom). The Prandtl number is $\sigma = 1$ in both cases. The triangle and circle symbols denote data for the Lewis number $L = 10^{-3}$ and $L = 10^{-2}$, respectively. The solid lines have slope of unity on the log-log scales. The exponents obtained from power law fits of the data are given in Table. 4.1.

in the range of small Lewis numbers, $10^{-3} \leq L \leq 10^{-2}$, the mean square displacement, and consequently the effective Lewis number, is independent of the Lewis number L. Thus, for small Lewis numbers at constant Prandtl number $\sigma = 1$, the effective Lewis number is then a function of only the Rayleigh number. This relation is plotted in Fig. 4.3, which shows that the increase in Lewis number is proportional to the square root of the reduced Rayleigh number,

$$L^* - L \propto \epsilon^{1/2}. \tag{4.12}$$

In other words, the effect of the advection of spiral defect chaos is to cause an increase

	$L = 10^{-3}$	$L = 10^{-2}$	$L = 10^{-1}$
$R = 3074$	0.290	0.291	0.382
$R = 3500$	0.350	0.351	0.498
$R = 4270$	0.420	0.413	0.529

Table 4.2: The effective Lewis number L^* computed from Eq. (4.11) for various values of the Rayleigh number R and the Lewis number L.

in the Lewis number of the passive tracer concentration that is proportional to the square root of the reduced Rayleigh number.

In addition, because it is also known that the characteristic velocity scale $||\mathbf{u}||$ of spiral defect chaos is proportional to the square root of the reduced Rayleigh number [27], it can also be deduced that the increase in Lewis number is directly proportional to the characteristic velocity scale of spiral defect chaos,

$$L^* - L \propto ||\mathbf{u}||, \tag{4.13}$$

An alternate way to state this result is to divide both sides of Eq. (4.13) by the Lewis number L to define the enhancement in Lewis number,

$$\Delta \equiv \frac{L^* - L}{L}, \tag{4.14}$$

so that one obtains the relation between this enhancement and the Péclet number,

$$\Delta \propto P. \tag{4.15}$$

Recall that the above result applies when the Lewis number is small, $L \leq 10^{-2}$ (or equivalently, when the Péclet number is large). On the other hand, when the Lewis number is large (when the Péclet number is small), similar calculations show that, although the net transport is still diffusive, a relation different from Eq. (4.15)

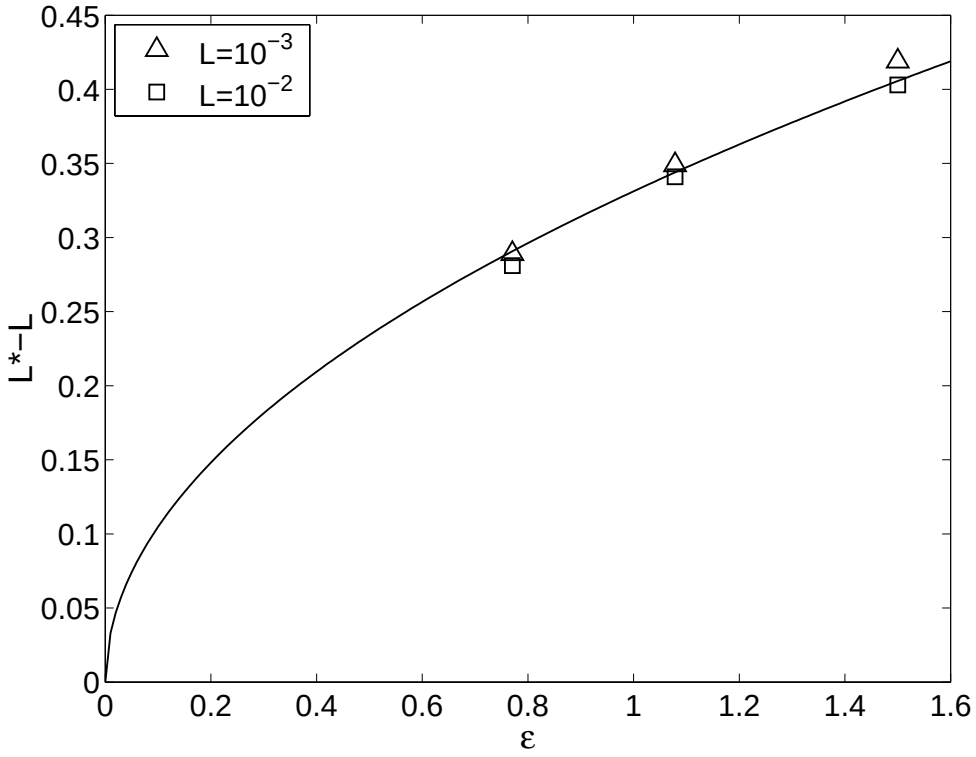

Figure 4.3: The effective Lewis number $L^* - L$ vs. the reduced Rayleigh number ϵ. The solid lines represent power laws with an exponent of 1/2.

is obtained,

$$\Delta \propto P^{1/2}. \tag{4.16}$$

This square root dependence of the enhancement on the Péclet number is similar to the result obtained experimentally [84] and calculated theoretically [74, 80] in the spreading of passive tracers in time-independent convection flows comprised of straight parallel rolls. In this case, the enhancement can be attributed to the Shraiman mechanism, which refers to the expulsion of the gradient of the passive tracer concentration from regions of closed stream lines [80]. Near a separatrix between two sets of closed stream lines, the only transport of the passive tracers from one roll to the next comes from the random walks of the passive tracers that lie within a thin layer of width d of the roll boundary (the roll itself is of unit width in the dimensionless unit system adopted in this dissertation). Thus, a fraction d of passive tracers

contribute to an increase, dL, in the effective Lewis number of the diffusion. The width d can be estimated from dimensional analysis [11] to be $d^2 \sim P^{-1}$. Combining these estimates leads immediately to Eq. (4.16). Thus, the result above suggests that the Shraiman mechanism, although strictly derived in a time-independent convection flows comprised of straight parallel rolls, may be a universal mechanism at sufficiently high Lewis numbers independent of the structure of the underlying flow field.

The enhancement in the Lewis number as a function of the Péclet number is summarized in Fig. 4.4. The two regimes given by Eqs. (4.15)–(4.16) are evident. In Sect. 4.3.3, the origin of these two distinct regimes is discussed in terms of the dependence of the wave number on the transport.

Finally, before concluding this section, some details are presented in the way the least squares fits are performed. First, data from early times are ignored due to the presence of transients. One such transient effect could be that, at very early times prior to the turnover time scale $\tau_c \sim ||\mathbf{u}||^{-1} \sim \mathcal{O}(10^{-1})$, the passive tracers "feel" that it is being transported by a constant velocity field, and so will exhibit ballistic behavior with $\gamma = 2$. There is then a crossover time in which γ decreases to unity, and this regime is to be ignored too. Second, data from late times are also ignored due to finite size effects. The effects of finite size are illustrated in Fig. 4.5, in which the exponent γ, obtained from the logarithmic derivative

$$\gamma(t) = \frac{d\log[V(t)]}{d\log(t)}, \tag{4.17}$$

is plotted as a function of time for the parameters $R = 3074$ and $L = 10^{-3}$ (solid line) and for a purely diffusive process without advection (dashed line, whose diffusivity is chosen to match that of effective diffusivity of the above process). The value of the exponent γ is found, in both cases, to be essentially a constant of approximately unity for all times $t \lesssim 80$. The decrease at $t \gtrsim 80$ is therefore a consequence of finite size effects.

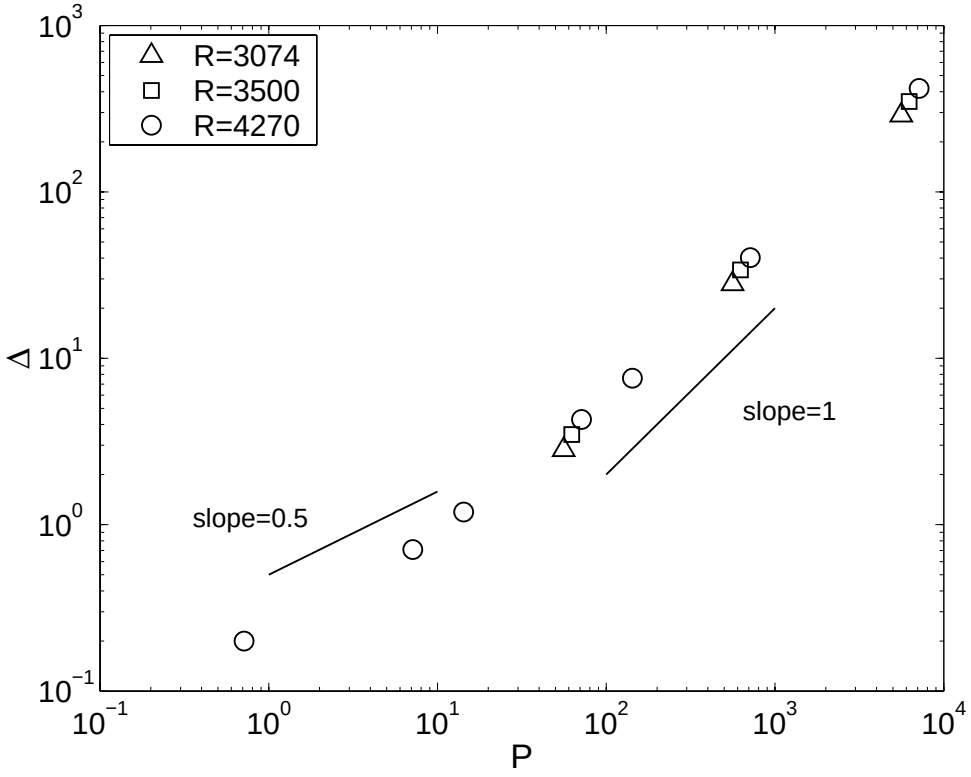

Figure 4.4: The enhancement in Lewis number Δ defined in Eq. (4.14) vs. the Péclet number P for various Rayleigh numbers R and the Prandtl number $\sigma = 1$. Note that, when the Péclet number approaches zero (i.e., when the advection becomes negligible so that the transport equation, Eq. (4.1), is the diffusion equation), the enhancement should approach zero as well. Thus, the data points are expected to pass through the origin ($P = 0, \Delta = 0$).

4.3.2 Normal diffusion vs. anomalous diffusion

In this section, several other tests are conducted on the passive tracer concentration to show that the spreading process is indeed governed by normal diffusion, and not anomalous diffusion. Anomalous diffusion is defined when the mean square displacement grows differently than being proportional to time, i.e., when $V(t) \propto t^{\gamma}$ with the exponent $\gamma \neq 1$. It has been observed in the transport of passive tracers in cellular Taylor-Couette flow in a rotating annulus [85, 86], and in various other geophysical turbulent flows arising from the presence of Lévy trajectories [79]. However, this section will show that there is no evidence of anomalous diffusion in transport in spiral

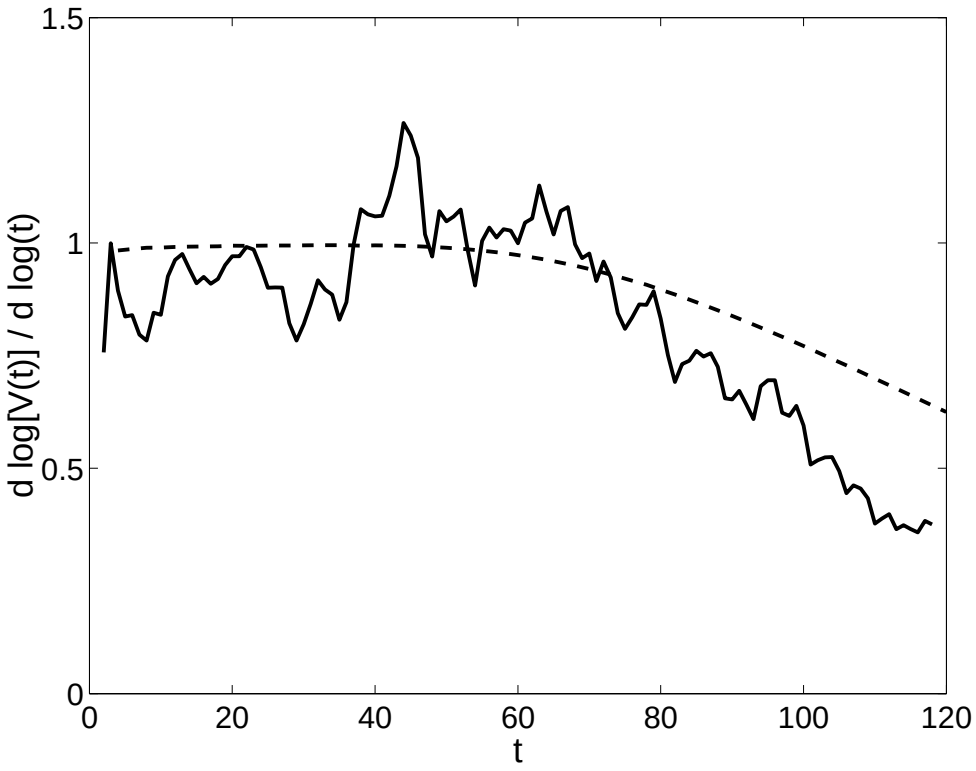

Figure 4.5: The logarithmic derivative γ vs. time t. The solid line is for the case of $R = 3074$ and $L = 10^{-3}$. The dashed line is for a purely diffusive process (i.e., Eq. (4.1) with $\mathbf{u} = 0$ and a Lewis number chosen to match the effective Lewis number of the previous case).

defect chaos, at least for the range of Lewis numbers investigated.

First, if the passive tracer concentration is spreading by normal diffusion, i.e., it obeys Eq. (4.10), then it can be expressed in the form of a Gaussian,

$$\tilde{\psi}(r,t) \sim \frac{1}{t} \exp\left(\frac{r^2}{4L^* t}\right), \tag{4.18}$$

and a plot of the logarithm of the scaled passive tracer concentration $\log[t \bullet \tilde{\psi}(r,t)]$ vs. the scaled distance squared $r^2/4t$ for different times t will all collapse onto the same straight line. This is indeed the case as shown in Fig. 4.6, which shows the data at times $t = 30$, $t = 40$, and $t = 70$ (triangles, squares, and circles, respectively) collapsing onto the same straight line. However, data from an earlier time $t = 5$ (dots)

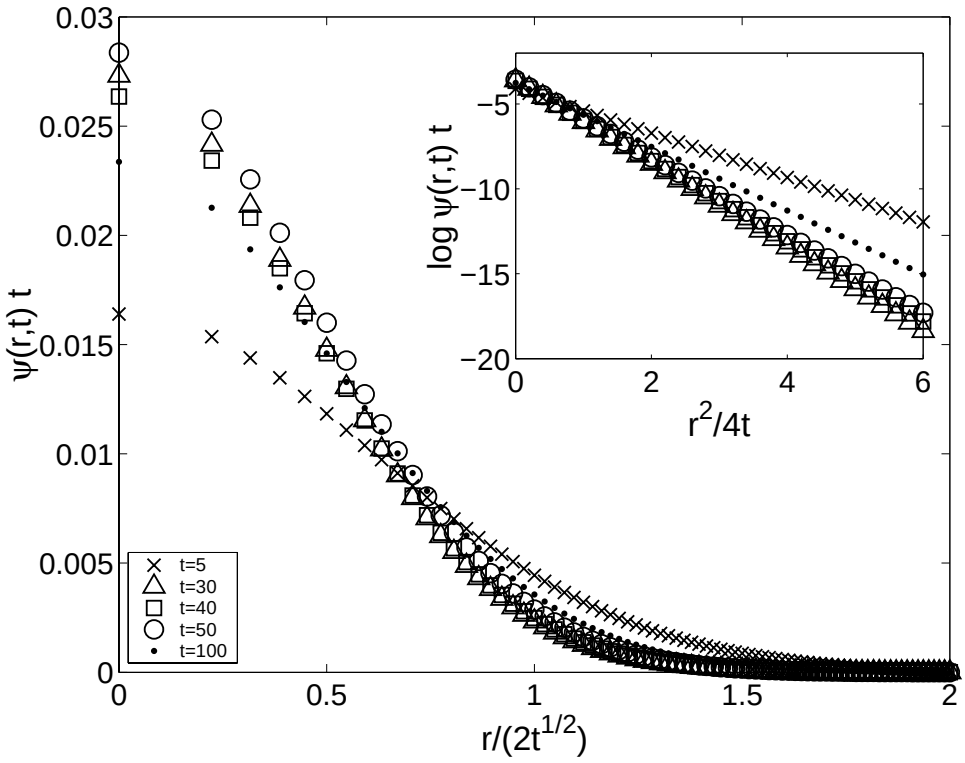

Figure 4.6: The scaled passive tracer concentration $t\psi(r,t)$ vs. the scaled distance squared $r^2/4t$. The various symbols denote different values of the times t. The data for times $t = 30$, $t = 40$, and $t = 70$ (triangles, squares, and circles, respectively) collapse onto the same straight line, suggesting the validity of the Gaussian form in this time range.

do not collapse onto the same straight line, presumably because of the presence of transient effects. Similarly, data from a later time $t = 100$ (crosses) do not collapse onto the same straight line, owing to the presence of finite size effects.

Second, there exists in general a relation between the mean square displacement of passive tracers and the correlation function of their Lagrangian velocities. More precisely, the Taylor relation for a passive tracer [11, 55] states that

$$\frac{d\langle|x_i(t) - x_i(0)|^2\rangle}{dt} = 2\int_0^t C_{ii}(\tau)d\tau \tag{4.19}$$

where

$$C_{ij}(\tau) \equiv \langle v_i(\mathbf{x}(t)v_j(\mathbf{x}(t+\tau))\rangle \tag{4.20}$$

is the correlation function of the Lagrangian velocities. The subscripts i and j represent x ,y, or z. This relation, discovered by G. I. Taylor in 1921, is a particular case of the Kubo formula [61] applied in a fluid dynamical context. Eq. (4.19) can then be integrated to give the mean square displacement in terms of the Lagrangian velocity correlation function,

$$V(t) \equiv \langle |x_i(t) - x_i(0)|^2 \rangle = 2 \int_0^t (t - \tau) C_{ii}(\tau) d\tau. \tag{4.21}$$

If the long time behavior of the correlation function C_{ii} decays exponentially, then the mean square displacement can be shown to grow linearly with time, thus yielding normal diffusion. However, if the long time behavior of the correlation function decays much more slowly, such as in an algebraic manner $C_{ii}(t) \sim t^{-\eta}$ with $0 < \eta < 1$, then the mean square displacement can be shown to grow faster than linearly, thus yielding anomalous diffusion, $\langle |x_i(t) - x_i(0)|^2 \rangle \sim t^{2-\eta}$. So, to verify whether the passive tracer concentration is spreading by normal diffusion or by anomalous diffusion, one can compute the Lagrangian velocity correlation function and study its long time decay. Unfortunately, the Lagrangian correlation function is not available in this dissertation because only the Eulerian approach is simulated. However, a "mean-field" hypothesis can be invoked to replace the Lagrangian correlation function with the Eulerian correlation function [11],

$$C_{ij}(\tau) \approx \langle u_i(x, t + \tau) u_j(x, t) \rangle. \tag{4.22}$$

Although this will almost certainly yield the wrong numerical values, one hopes that the form of the correlation function, i.e., whether it decays exponentially or algebraically, will be correctly reproduced. If the long time behavior of the Eulerian velocity autocorrelation function decays exponentially, then one expects from the Wiener-Khinchinte theorem [61] that the behavior of the power spectrum will follow a Lorentzian decay,

$$P(f) \sim \lim_{f \to f_0} \left[1 + \tau^2 (f - f_0)^2 \right]^{-1}, \tag{4.23}$$

in the vicinity $f \to f_0$ with a correlation time τ. If the long time behavior of the Eulerian velocity autocorrelation function decays as a power law, then the low-frequency behavior of the power spectrum will exhibit a power law cusp in the vicinity of $f \to f_0$. In Fig. 4.7, the power spectrum of the Eulerian velocity field is plotted. At the maxima $f \to f_0$, the power spectrum does not exhibit cusp-like behavior. In fact, the solid line is a fit to the Lorentzian form, Eq. (4.23). The good fit between the Lorentzian and the data at small $f - f_0$ suggests that the correlation function $C_{ij}(\tau)$ is indeed exponentially decaying at large times, and consequently, that the diffusion of the passive tracers is normal and not anomalous. (The power spectrum in Fig. 4.7 reveals that $f_0 \neq 0$, a result not observed in power spectra obtained from experiments [57]. It is postulated that this artifact arises from the use of a velocity time series that is not sufficiently long in time, and that finite length cutoffs are responsible for creating spurious oscillations.)

Third, possible deviations from the Gaussianity of the passive tracer concentration are checked by looking at the higher-order moments,

$$M_q(t) = \frac{\int_0^\Gamma \int_0^{2\pi} [r - \bar{r}(t)]^q \psi(r, \theta, t)\, r\, dr\, d\theta}{\int_0^\Gamma \int_0^{2\pi} \psi(r, \theta, t)\, r\, dr\, d\theta}. \tag{4.24}$$

Note that, in this notation, the mean square displacement $V(t)$ is simply $M_2(t)$. For normal diffusion, the higher-order moments are expected to scale like

$$M_q(t) \propto t^{q/2.} \tag{4.25}$$

Thus, if the passive tracer concentration is indeed of Gaussian form, then the scaled higher-order moments $t^{-1} M_q(t)^{2/q}$ will be constants in time for all q over a certain time range. In Fig. 4.8, the scaled higher-order moments for $q = 2$, 4, 6, and 8 are plotted as functions of time. The top panel is for the passive tracer concentration when the Rayleigh number $R = 3500$, the Prandtl number $\sigma = 1$ and the Lewis number $L = 10^{-2}$. The bottom panel is for a purely diffusive process with diffusivity chosen to match the former's effective diffusivity. Unfortunately, because of finite size effects,

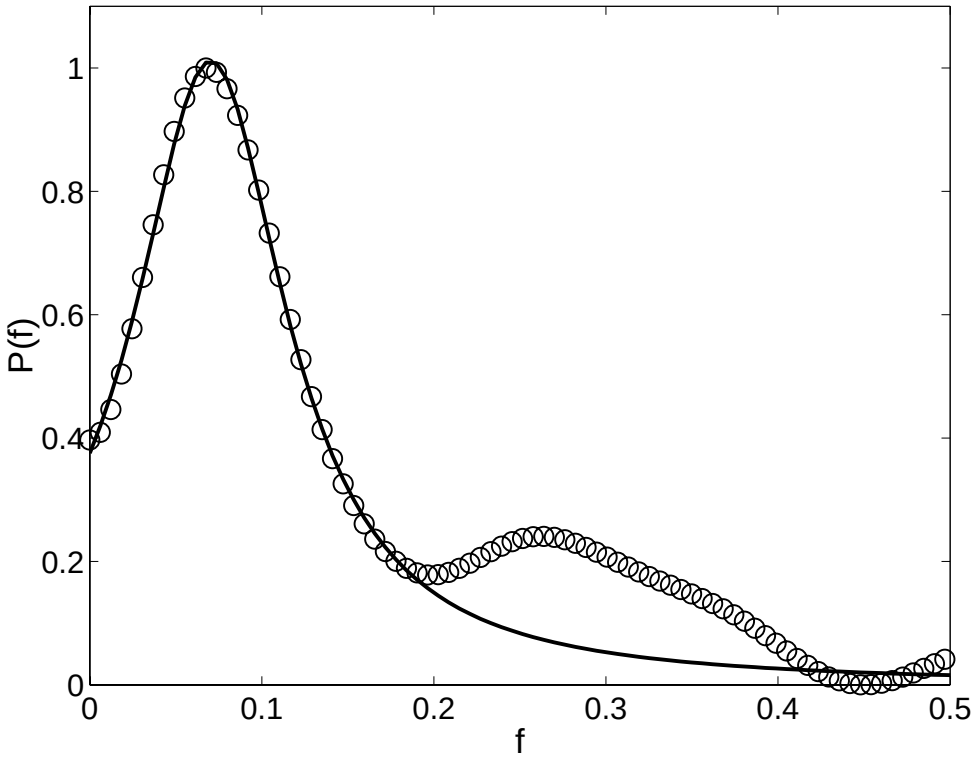

Figure 4.7: Power spectrum of the Eulerian velocity correlation function (circles) and a Lorentzian fit (solid line) of the form suggested in Eq. (4.23).

the scaled higher-order moments have only a very small range for which they are constant in time. For example, at $q = 8$, this range is only $5 \lesssim t \lesssim 20$. Nevertheless, by comparing both top and bottom plots, it is possible to discern that the scaled higher-order moments exhibit constancy in time over rather similar ranges. In other words, apart from finite size effects, there are no discernible deviations from Gaussianity for the passive tracer concentrations.

Thus, all three observations above suggest that the spreading of the passive tracer concentration is governed by normal diffusion.

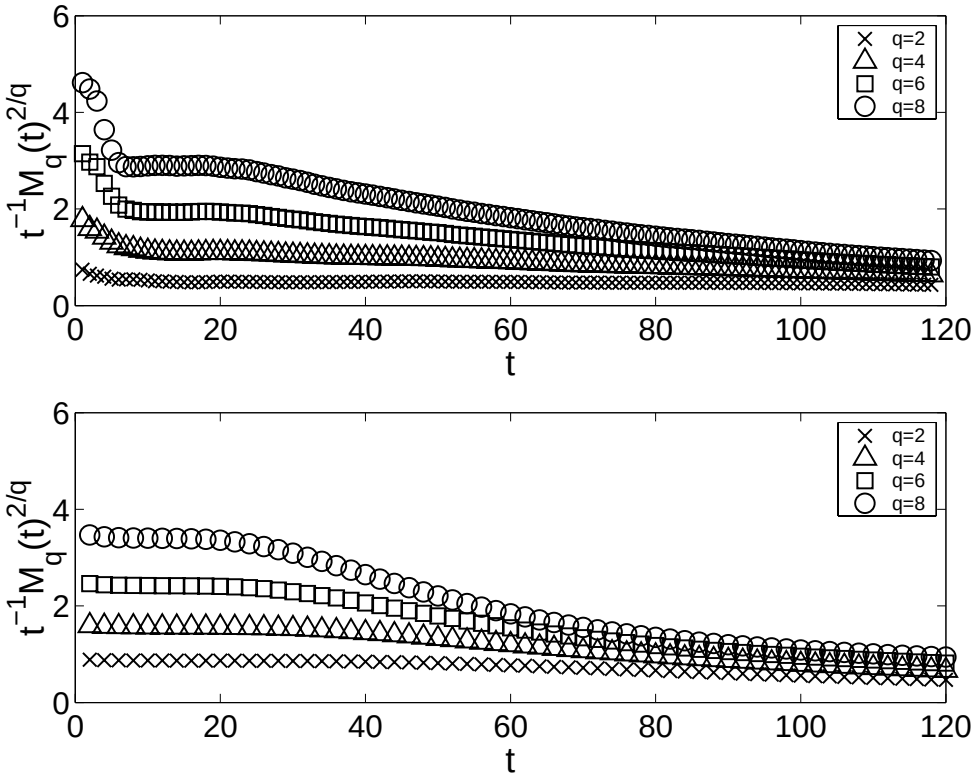

Figure 4.8: Scaled higher-order moments, $t^{-1}M_q(t)^{2/q}$, of the passive tracer concentration vs. time t for the parameters $R = 3500$, $\sigma = 1$, and $L = 10^{-2}$ (top) and for a purely diffusive process (bottom). As q increases, the range of time for which the scaled moment stays constant in time decreases, owing to finite size effects.

4.3.3 Wave number dependence in the transport of passive tracers

In this section, the existence of two distinct regimes for the enhancement in Lewis number, namely at small Lewis numbers given by Eq. (4.15) and at large Lewis numbers given by Eq. (4.16), is investigated in terms of the local wave number dependence. First, a local quantity called the horizontal spreading orientation, $\Theta(x, y)$, can be defined at every location in the cell,

$$\cos(\Theta) = \frac{\nabla_\perp \psi \bullet \mathbf{k}}{|\nabla_\perp \psi||\mathbf{k}|}, \tag{4.26}$$

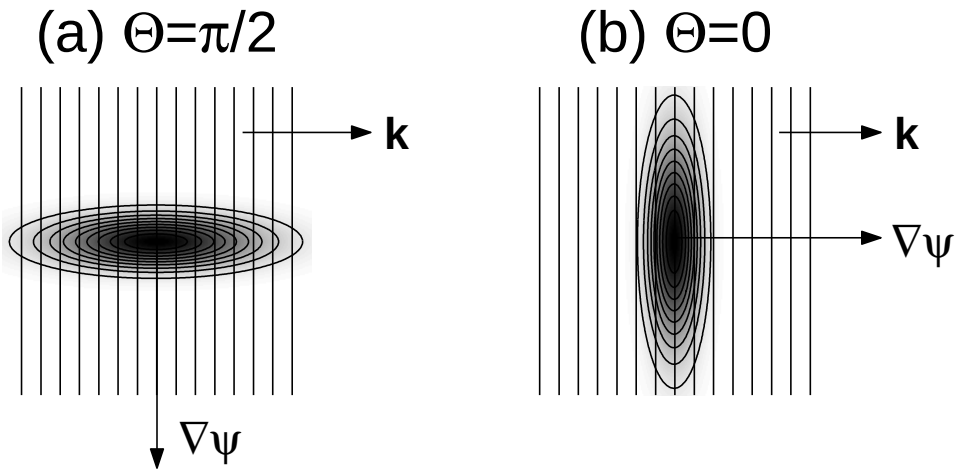

Figure 4.9: Illustrations showing the definition of the horizontal spreading orientation, Θ, at *(a)* $\Theta = \pi/2$ corresponding to lateral spreading, and *(b)* $\Theta = 0$ corresponding to longitudinal spreading.

where the subscript $\perp$ denotes the horizontal coordinates (x, y) and the wave vector $\mathbf{k}$ is defined in Eq. (1.15). If the passive tracer concentration spreads laterally in the direction parallel to the convection rolls, i.e., in the direction of $\mathbf{k}$, then, as illustrated in Fig. 4.9(a), the gradient $\nabla_\perp \psi$ will be orthogonal to $\mathbf{k}$, resulting in the local horizontal spreading orientation acquiring the value of $\Theta = \pi/2$. On the other hand, if the passive tracer concentration spreads longitudinally in the direction perpendicular to the convection rolls, i.e., in the direction orthogonal to $\mathbf{k}$, then, as illustrated in Fig. 4.9(b), the local horizontal spreading orientation will be $\Theta = 0$.

For a particular passive tracer concentration, the horizontal spreading orientation can then be computed locally at every point in the mid-plane of the convection cell and then histogrammed. In Fig. 4.10, such a distribution of the horizontal spreading orientation, $P(\Theta)$, is plotted for several values of the Lewis number ranging from $L = 10^{-4}$ to $L = 10^{-1}$, the Rayleigh number $R = 3500$ and the Prandtl number $\sigma = 1$ at the time $t = 50$. Consider first the distribution for the relatively large Lewis number of $L = 10^{-1}$ (denoted by crosses). This distribution has a dominant peak at $\Theta = \pi/2$. This suggests that, locally, the spreading of the passive tracer concentration occurs mostly laterally [i.e., as illustrated in Fig. 4.9(a)]. This can be attributed to the

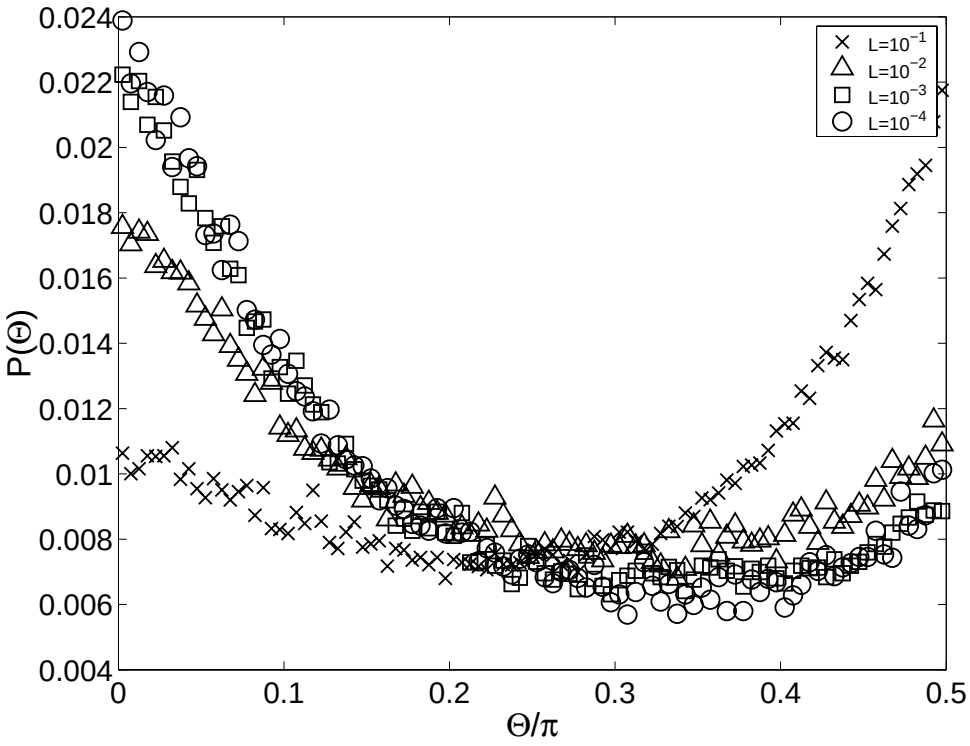

Figure 4.10: Distribution of horizontal spreading orientations $P(\Theta)$ for the Rayleigh number $R = 3500$, the Prandtl number $\sigma = 1$ and the Lewis number ranging from $L = 10^{-4}$ to $L = 10^{-1}$.

Shraiman mechanism described earlier in Sect. 4.3.1. However, at the smaller Lewis numbers of, say, $L = 10^{-2}$, the distribution of the horizontal spreading orientation is visibly different. In this case, the distribution shows a dominant primary peak at $\Theta = 0$ and then a smaller secondary peak at $\Theta = \pi/2$. In other words, the spreading of the passive tracer concentration is locally mostly longitudinal rather than mostly lateral [i.e., as illustrated in Fig. 4.9(b)].

To find out what is the underlying mechanism that causes this local longitudinal spreading, the following is performed. The local wave numbers that correspond to locations in the convection mid-plane that exhibit longitudinal spreading (i.e., $\Theta \to 0$) is compared to those locations in the convection mid-plane that exhibit lateral spreading (i.e., $\Theta \to \pi/2$). In Fig. 4.11, the distribution of wave numbers $P(k)$ for which the longitudinal spreading occurs is plotted (solid lines) together with the

distribution for which lateral spreading occurs (dashed lines) for a large Lewis number case [Fig. 4.11(a)] and a small Lewis number case [Fig. 4.11(b)]. Consider first the region of wave numbers near the mean, $\langle k \rangle \approx 2$, of the spiral defect chaotic planform. For both large and small Lewis numbers, lateral spreading ($\Theta \rightarrow \pi/2$, dotted lines) dominates. This suggests that, at regions of the planform with wave numbers near the mean, the Shraiman mechanism is the predominant mechanism for transport. However, this predominance is suppressed as the Lewis number decreases (i.e., the peak of the dotted distribution becoming smaller). At the same time, the magnitude of longitudinal spreading increases. Consider next the region of wave numbers far away from the mean, i.e., regions corresponding to the occurrence of defects. At large Lewis numbers [Fig. 4.11(a)], the distributions for both lateral spreading (dotted line) and longitudinal spreading (dashed line) are identical. This suggests that, in the region of a defect structure, the transport at large Lewis numbers is isotropic rather than by the Shraiman mechanism. However, at small Lewis numbers [Fig. 4.11(b)], longitudinal spreading (solid line) actually becomes dominant. Thus, at small Lewis numbers, the occurrence of defects suppresses the Shraiman mechanism but enhances longitudinal spreading [as illustrated in Fig. 4.9(b)].

4.3.4 Numerical details

Finally, before this chapter is concluded, a detail pertaining to the use of the `nek5000` solver in solving the transport equation, Eq. (4.1) is discussed. One well-known difficulty [37, 92] associated with integrating Eq. (4.1) is that, for small Lewis numbers $L \ll 1$ as was the focus of this chapter, the spatial resolution Δx has to be very small. This scale is set by the smallest scale in the tracer field, such as the thickness of the interface where the tracer is initially zero on one side and unity on the other. The interface is then stretched by a strain rate $S \sim \partial u/\partial x \sim ||\mathbf{u}||$, and its thickness will be proportional to $(L/S)^{1/2}$, i.e.,

$$\Delta x \sim \left(\frac{L}{||\mathbf{u}||} \right)^{1/2} = P^{-1/2}. \tag{4.27}$$

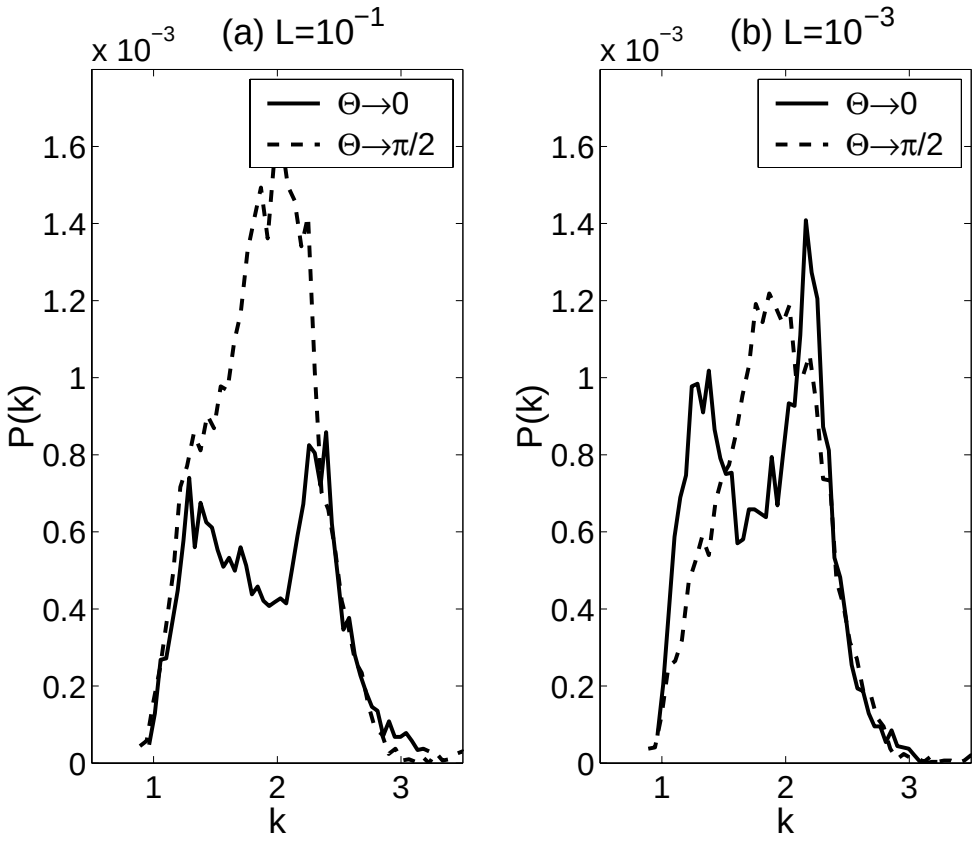

Figure 4.11: Distribution of wave numbers $P(k)$ for which longitudinal spreading occurs (solid lines) and for which lateral spreading occurs (dashed lines), for *(a)* large Lewis number $L = 10^{-1}$ and *(b)* small Lewis number $L = 10^{-3}$ at the Rayleigh number $R = 3500$ and the Prandtl number $\sigma = 1$.

For the kind of spiral defect chaos considered in this chapter, the velocity magnitude is $||\mathbf{u}|| \sim \mathcal{O}(10)$. Thus, a simulation at the Lewis number of, say, $L = 10^{-3}$ will require $\Delta x \sim 10^{-2}$ in order to satisfy Eq. (4.27). However, current computational resources dictate that Δx be about $\gtrsim 10^{-1}$, and in fact, in this dissertation, $\Delta x = 0.125$.

This problem is overcome by using a simple filtering procedure developed by Fischer and Mullen [36]. At the end of each time step, a filter is applied on an element-by-element basis to the passive tracer concentration field ψ. In one dimension, the filtered field can be written as

$$F(\psi;\alpha) = \alpha\Pi_{N-1}(\psi) + (1-\alpha)\psi, \tag{4.28}$$

where the operator Π_{N-1} first interpolates ψ onto the mesh points for a polynomial of degree $N-1$ determined by the mesh spacing and then interpolates the result back onto the mesh points for a polynomial for degree N. In higher dimensions, the tensor product form of Eq. (4.28) is used. Typical values of α used lie in the range $0.05 \leq \alpha \leq 0.2$. This filtering procedure preserves inter-element continuity and spectral accuracy. Using this filter and maintaining $\Delta x = 0.125$, a stable Lewis number of up to $L = 10^{-3}$ can be attained.

To verify that the filter allows the diffusion to be sufficiently resolved at small Lewis numbers, the following heuristic check is performed. First, a local advection orientation, $\Phi(x, y)$, is defined via

$$\cos(\Phi) = \frac{\nabla\psi \bullet \mathbf{u}}{|\nabla\psi||\mathbf{u}|}, \tag{4.29}$$

with $\mathbf{u}$ the velocity field. If the local passive tracer concentration is being advected by the local velocity and diffusion is not being sufficiently resolved, then the gradient of the former will be orthogonal to the local velocity, and consequently, $\Phi = \pi/2$. On the other hand, if the local passive tracer concentration exhibits diffusion, then it will change in a direction perpendicular to the local velocity, yielding $\Phi = 0$; see Fig. 4.12 for illustrations.

For small Lewis numbers where the effects of advection dominate over the effects of molecular diffusion, the distribution of the local advection orientation, $P(\Phi)$, over the mid-plane of the cell, should exhibit a strong peak at $\Phi = \pi/2$. This peak will then broaden as the Lewis number is increased, as the effects of diffusion cause the passive tracer concentration to spread out at all orientations relative to the local velocity. The presence of this broadening in the distribution of the local advection orientation is then an indication that molecular diffusion has been sufficiently resolved. The distributions $P(\Phi)$ for the various Lewis numbers ranging from $L = 10^{-4}$ to $L = 10^{-1}$ are plotted in Fig. 4.13.

The distribution for $L = 10^{-2}$ is distinctly different from that for $L = 10^{-3}$, providing evidence that the molecular diffusion at $L = 10^{-3}$ has been stably resolved,

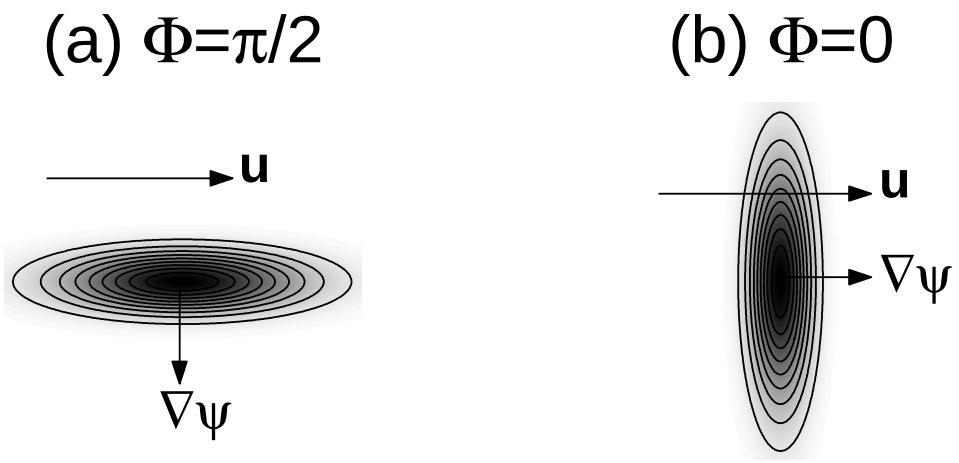

Figure 4.12: Illustrations showing the definition of the local advection orientation, Φ, at *(a)* $\Phi = \pi/2$ and *(b)* $\Phi = 0$.

i.e., that the chosen grid spacing Δx is sufficiently small for the simulation to be stable. However, the relative similarity in the distributions for $L = 10^{-3}$ and $L = 10^{-4}$ suggests that diffusion for the latter case may not have been sufficiently resolved. Consequently, the smallest allowed Lewis number is set at $L = 10^{-3}$.

4.4 Conclusions

In this chapter, the spreading of a passive tracer concentration in a Rayleigh-Bénard convection flow exhibiting spiral defect chaos is studied. It is found that, in the presence of advection by spiral defect chaos, the spreading can be characterized by normal diffusion. The enhancement in the diffusivity of the passive tracer concentration follows two regimes. When the molecular diffusivity of the tracer concentration is small, the enhancement is proportional to the Péclet number. When the molecular diffusivity is large, the enhancement is proportional to the square root of the Péclet number. This difference is explained in terms of the dependence of the transport on the local wave numbers. It is found that tracer concentrations with small molecular diffusivity experience enhanced longitudinal diffusion and suppressed lateral diffusion

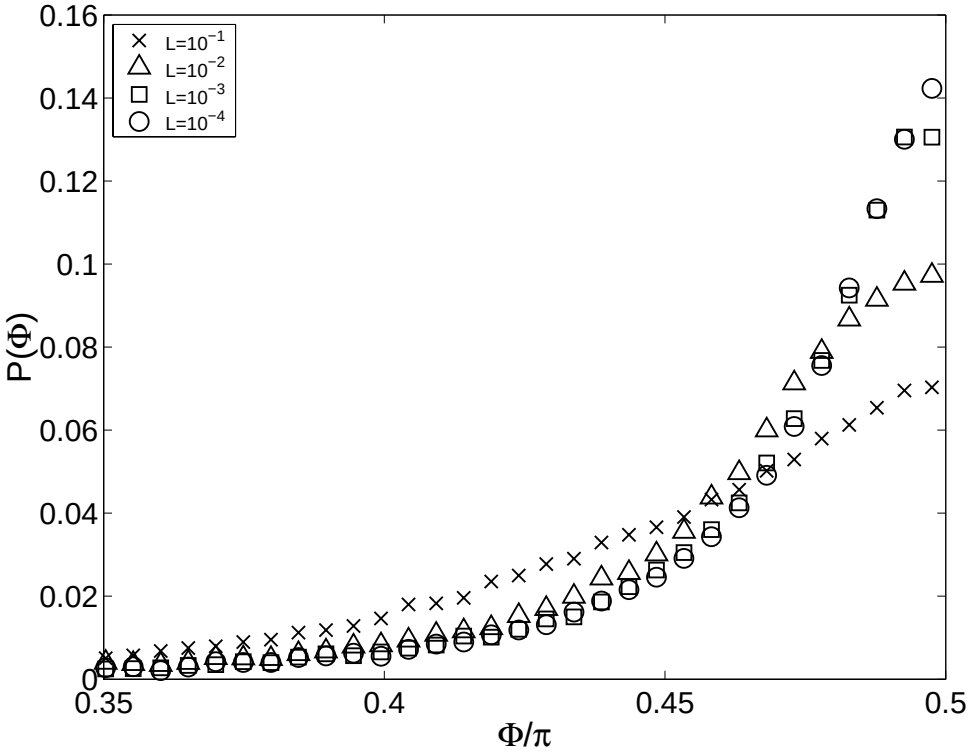

Figure 4.13: Distribution of local advection orientations for various Lewis numbers ranging from $L = 10^{-4}$ to $L = 10^{-1}$.

at regions of the flow occupied by defects.

Chapter 5

Propagation of perturbations in spiral defect chaos

5.1 Introduction

This chapter addresses the problem of how a perturbation, initially localized in space, propagates through a state exhibiting spiral defect chaos. Knowledge of how these perturbations, or "hot spots," spread, as well as their dynamics, are of considerable importance to the development of successful strategies for the control of chaos in spatially-extended systems [42]. Consequently, there have already been theoretical work to address this problem. However, these previous studies focussed primarily on simple models, such as a one-dimensional reaction-diffusion model [99], a system of coupled one-dimensional logistic maps [40], and two-dimensional coupled map lattices [98]. In addition, there has also been efforts to study these "hot spots" experimentally [75]. For example, one could use optical heating to locally perturb a particular region of a convection cell, and then look at the differences between the images of the initial convection planform and the planform affected by the perturbations. The modal structure of the dynamics that evolves from such a perturbation can then be further extracted, and the growth rates of such modes calculated.

In this chapter, a computational approach to this problem of "hot spots" propagation is described. The approach is then used to study two particular problems. First, the propagation of a perturbation initially localized at the core of one of the many

spirals in a state exhibiting spiral defect chaos is studied. Second, the propagation of a localized perturbation in a pre-chaotic stripe texture is studied. Admittedly, a more complete analysis of the propagation of perturbations can be performed. However, these are left for the future because of the expensive cost associated with integrating the perturbation equations [see Eqs. (5.2)–(5.4) below]. So, for now, only these two applications are described.

5.2 Definitions

While it is possible to define the perturbations to a state in terms of the difference between two states with initial conditions differing slightly in only a localized region, this definition will not be used in this dissertation, because the differences may eventually grow to be of a substantial magnitude, thus causing numerical difficulties. Instead, consider infinitesimal perturbations on a state, i.e., let the primitive variables describing Rayleigh-Bénard convection, namely the velocity, temperature, and pressure fields, $(\mathbf{u}, T, p)$, be infinitesimally perturbed,

$$(\mathbf{u}, T, p) \rightarrow (\mathbf{u}, T, p) + \eta(\delta\mathbf{u}, \delta T, \delta p), \tag{5.1}$$

where η is an infinitesimally small constant. Then, substituting these new perturbed state variables into the Boussinesq equations, Eqs. (1.5)–(1.7), the resulting equations at $\mathcal{O}(\eta)$ are

$$\begin{aligned}
\sigma^{-1}\left(\partial_t + \mathbf{u}\bullet\nabla\right)\delta\mathbf{u}(x,y,z,t) &= -\nabla\delta p + \nabla^2\delta\mathbf{u} + R\delta T\hat{z} - \delta\mathbf{u}\bullet\nabla\mathbf{u}, &(5.2)\\
\left(\partial_t + \mathbf{u}\bullet\nabla\right)\delta T(x,y,z,t) &= \nabla^2\delta T - \delta\mathbf{u}\bullet\nabla T, &(5.3)\\
\nabla\bullet\delta\mathbf{u} &= 0. &(5.4)
\end{aligned}$$

The terms at $\mathcal{O}(\eta^2)$ are considered negligible. Eqs. (5.2)–(5.4) is a set of linear equations that describe the evolution of the perturbations $(\delta\mathbf{u}, \delta T, \delta p)$. They are to be evolved concurrently with the Boussinesq equations.

Because the material walls of the cell are assumed to be no-slip, the velocity perturbation field satisfies

$$\delta\mathbf{u} = \mathbf{0}, \quad \text{on all material walls.} \tag{5.5}$$

Because the temperature field is constant on the top and bottom plates, the temperature perturbation field satisfies

$$\delta T\left(x, y, z = \mp\frac{1}{2}, t\right) = 0. \tag{5.6}$$

Finally, because the lateral walls are assumed to be perfectly insulating,

$$\widehat{n} \bullet \nabla\delta T = 0, \quad \text{on lateral walls,} \tag{5.7}$$

where $\widehat{n}$ is the unit vector perpendicular to the lateral walls at a given point. The pressure perturbation field δp has no associated boundary condition since it does not satisfy a dynamical equation. The linearized perturbation equations are discretized and integrated using the `boxcode` in a manner similar to that of the Boussinesq equations as described in Chap. 2.

In this chapter, only the temperature field will be initially perturbed. The initial velocity and pressure perturbations are set to zero,

$$\delta\mathbf{u}(t = 0) = \mathbf{0}, \quad \delta p(t = 0) = 0. \tag{5.8}$$

It is found that, should the initial perturbation be in any one of the other fields apart from the temperature field, the propagation of the perturbations in that field will yield the same behavior as that of the temperature perturbations.

5.3 Results

Eqs. (5.2)–(5.4) are evolved concurrently with the Boussinesq equations, Eqs. (1.5)–(1.7), for the following parameters: the reduced Rayleigh number for fully-developed spiral defect chaos at $\epsilon = 1.0$ and for a pre-chaotic stripe texture at $\epsilon = 0.15$, the Prandtl number $\sigma = 1$, and a rectangular cell of aspect ratio $\Gamma = 20$. The initial condition used for the temperature perturbation field is

$$\delta T(x, y, z, t = 0) = \exp\left[-\frac{(x - x_0)^2 + (y - y_0)^2 + z^2}{6\Delta^2}\right], \tag{5.9}$$

where $\Delta = 0.25$ is a small constant to ensure that the perturbation is initially localized. In Sects. 5.3.1–5.3.2, the location (x_0, y_0) is chosen to be at a spiral core. In Sect. 5.3.3, it is chosen to be at the center of a convection roll. At time $t = 0$, the temperature, velocity, and pressure fields correspond to an asymptotic state of spiral defect chaos, i.e., one that has been evolved from random thermal perturbations up to a time of $\mathcal{O}(\Gamma^2)$. Because the focus is only on cells of large aspect ratio, $\Gamma \gg 1$, the z-dependence of the perturbation fields are found to be essentially constant. As such, the z-dependence will be dropped in subsequent discussions and the perturbation fields, e.g., $\delta T(x, y, t)$ will be considered as functions of two-dimensional horizontal space and time.

5.3.1 Long time evolution of perturbations to spiral defect chaos

In this section, the perturbations are initially localized at the core of one of the spiral arms in a spiral defect chaotic planform at the reduced Rayleigh number $\epsilon = 1.0$ and the Prandtl number $\sigma = 1$. The perturbations are then allowed to evolve according to Eqs. (5.2)–(5.4). This evolution of the temperature perturbation field $\delta T(x, y, t)$ at the mid-plane $z = 0$ is shown in Fig. 5.1 for long times up to $t = 200$.

It can be seen that, while the magnitude of the perturbation grows with time (as is to be expected for a chaotic state), the location at which the perturbation

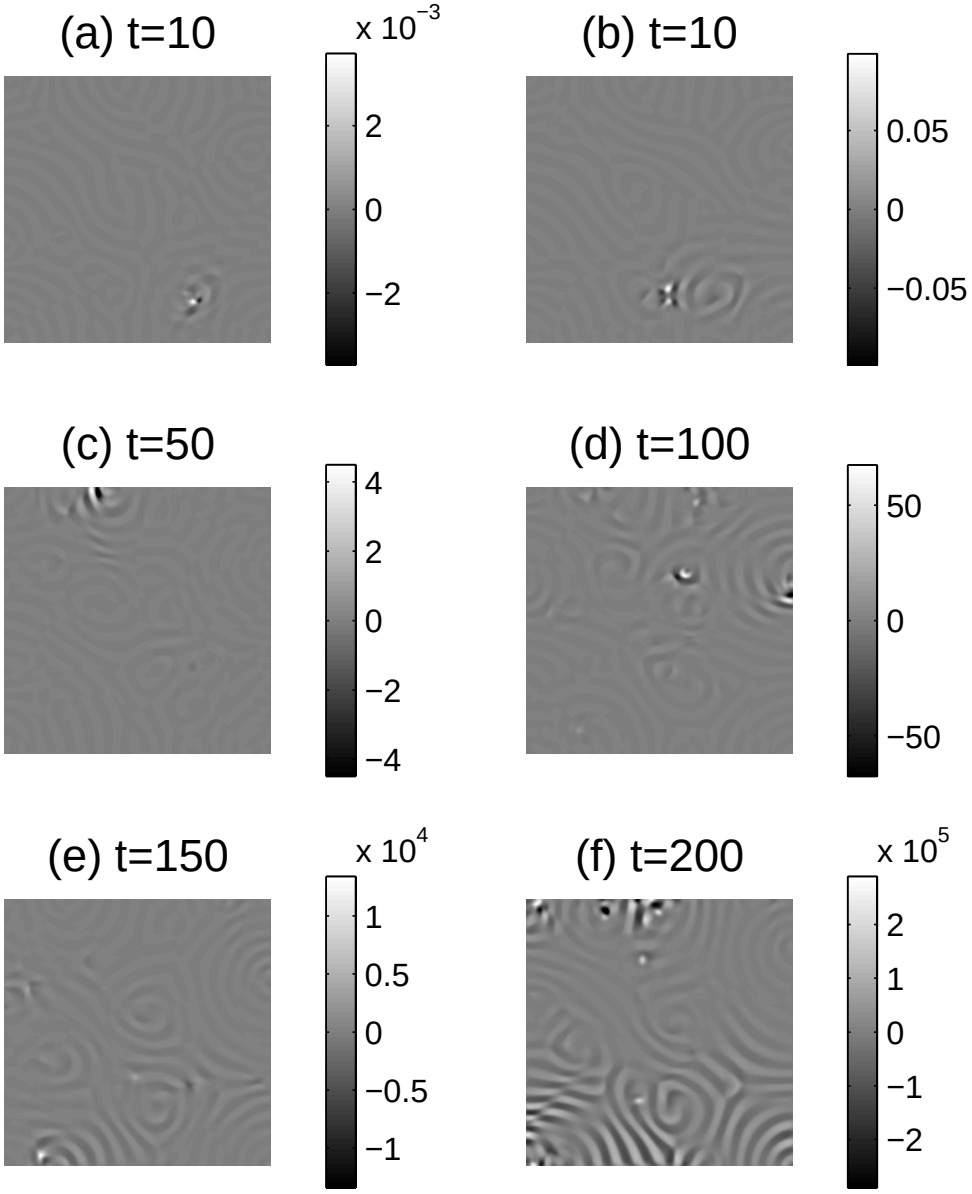

Figure 5.1: Long time evolution of the temperature perturbation field $\psi(x, y, z = 0, t)$ in spiral defect chaos for various times t. The reduced Rayleigh number is $\epsilon = 1.0$ and the Prandtl number $\sigma = 1$. Black and white colors denote negative and positive perturbations, respectively.

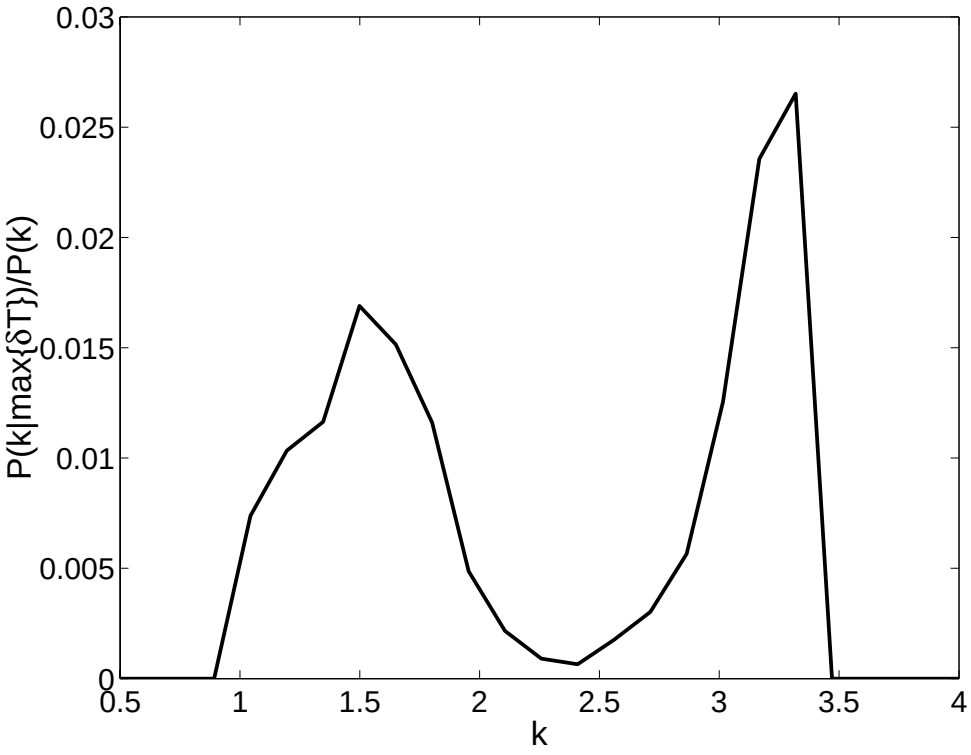

Figure 5.2: Distribution of wave numbers at locations of maximal perturbation at time $t = 50$. The mean wave number at this time is $\langle k \rangle \approx 2.2$. The dominance of the distribution at wave numbers far away from the mean suggests that the locations of maximal perturbation are occupied by defects.

attains a maximum changes with time, "hopping" from one region of the planform to another. More importantly, these locations of maximal perturbation are occupied by defects. This is illustrated more quantitatively in Fig. 5.2, which plots the distribution of wave numbers at these locations of maximal perturbation. It is seen that the maximal perturbations are distributed predominantly at wave numbers that are far away from the mean of $\langle k \rangle \approx 2.2$, corresponding to the occurrence of defects. Thus, defects serve as nucleation sites for the perturbations. An initial perturbation spreads out around a defect structure, and when this spreading perturbation reaches another defect structure, the perturbation begins to grow rapidly around that defect structure.

Using the techniques of Chap. 4, the spreading of the thermal perturbation field can be quantified by its mean square displacement $V(t)$ and center of mass $\langle r \rangle$, using

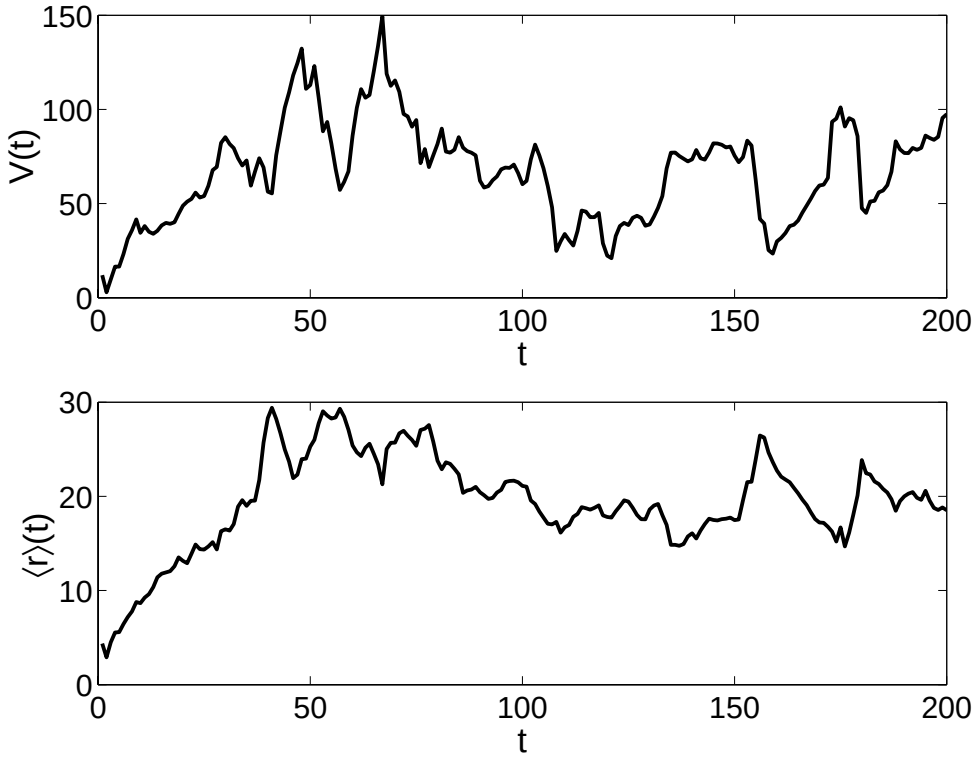

Figure 5.3: Mean square displacement $V(t)$ (top) and center of mass $\langle r \rangle(t)$ (bottom) of the thermal perturbation field in a spiral core when the reduced Rayleigh number $\epsilon = 1.0$ and the Prandtl number $\sigma = 1$.

Eqs. (4.8) and (4.9), respectively, but with $\psi(x, y, t)$ replaced by $\delta T(x, y, t)$. The mean square displacement and the center of mass of the temperature perturbation field are plotted in Fig. 5.3. It is seen that both the mean square displacement and the center of mass grows with time for short times $t \lesssim 50$, but fluctuates after that. Thus, least squares fits do not yield good power laws, and so, it cannot be concluded if the spreading is described by normal diffusion or anomalous diffusion. This problem can be overcome in the future by calculating the spreading over many more different instances of the initial condition, thus resulting in better statistics for the mean square displacement. These calculations are numerically expensive, but can be performed simultaneously in parallel. Thus, advances in the development of grid and cluster computing technologies should prove to be useful.

Finally, to verify that the growth of the perturbation is indeed chaotic, Fig. 5.4

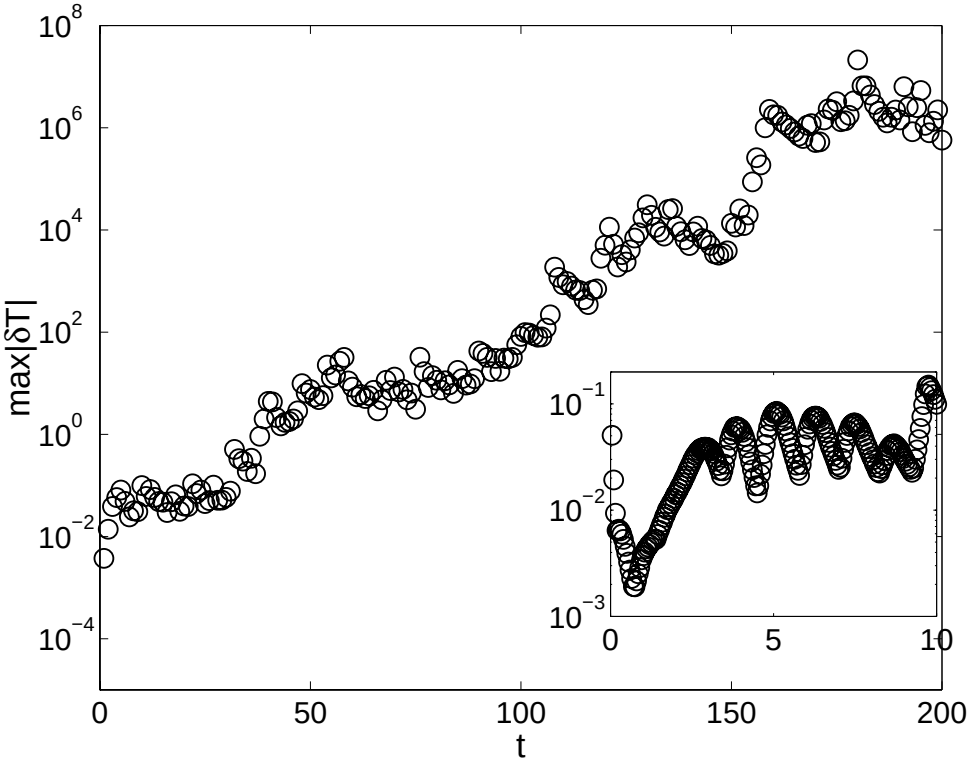

Figure 5.4: Maximal magnitude of the thermal perturbation applied to a spiral core, as shown in Fig. 5.5, vs. time t. The inset shows the growth at early times, and clearly exhibits an oscillatory behavior.

plots the maximal magnitude of the temperature perturbation as a function of time. It can be seen that the perturbation grows exponentially. However, the inset of Fig. 5.4 shows that, on top of this trend of exponential growth, there exists at short times an oscillatory behavior with a period of approximately one diffusion time unit. The next section discusses the origin of this oscillatory behavior in the perturbations.

5.3.2 Perturbations to spiral core in spiral defect chaos

In this section, the short-time behavior of the oscillatory behavior in the perturbations in the spiral core is studied. First, Fig. 5.5 shows the short-time evolution of the temperature perturbation in the vicinity of the initial spiral core. It is found that this oscillation occurs only at the spiral core, not throughout the planform. This

is illustrated in the next figure, Fig. 5.6, which plots the thermal perturbation at three locations (located by the cross and the two triangles in the inset planform) as a function of time. Oscillations are observed in the perturbation $\delta T(x = x_0, y = y_0, t)$ at the spiral core (crosses). However, oscillations are not observed at the two other locations near to, but not located at, the spiral core (dashed and dotted lines, for the location marked by the down- and up-pointing triangles, respectively). Spiral core oscillations have in fact been observed in Swift-Hohenberg models of spiral defect chaos [26]. However, because this oscillation occurs at small length scales, the Swift-Hohenberg modeling of the fluid behavior is not necessarily reproduced correctly. This section thus provides evidence that this spiral core oscillation is indeed a real effect, and not an artifact of the Swift-Hohenberg modeling. Thus, to sum up, the dynamics of the spiral core is locally chaotic, and the cause of this chaos is an oscillatory instability.

5.3.3 Perturbations to pre-chaotic stripe textures

In this section, the perturbations are localized initially at the center of a convection roll that is part of a texture of straight and parallel stripes. The reduced Rayleigh number is $\epsilon = 0.15$ and the Prandtl number is $\sigma = 1$. In Fig. 5.7, the evolution of the temperature perturbation field $\delta T(x, y, t)$ at the mid-plane $z = 0$ is shown for various times t.

The temperature perturbation is seen to spread rapidly outwards with time. Initially, the spreading is isotropic, with the perturbation field spreading outwards in an approximately circular manner. However, at later times, this spreading becomes anisotropic, spreading into an approximate "X"-shape. The presence of this convex shape in the anisotropic spreading, instead of a more common concave elliptical shape, is still not understood. It is postulated to be caused by the presence of curvature in the convection rolls in the texture far away from the cell center. Thus, regions parallel to the roll are being "invaded" more quickly then regions perpendicular to the rolls in regions with curvature. However, despite the presence of curvature, the anisotropy

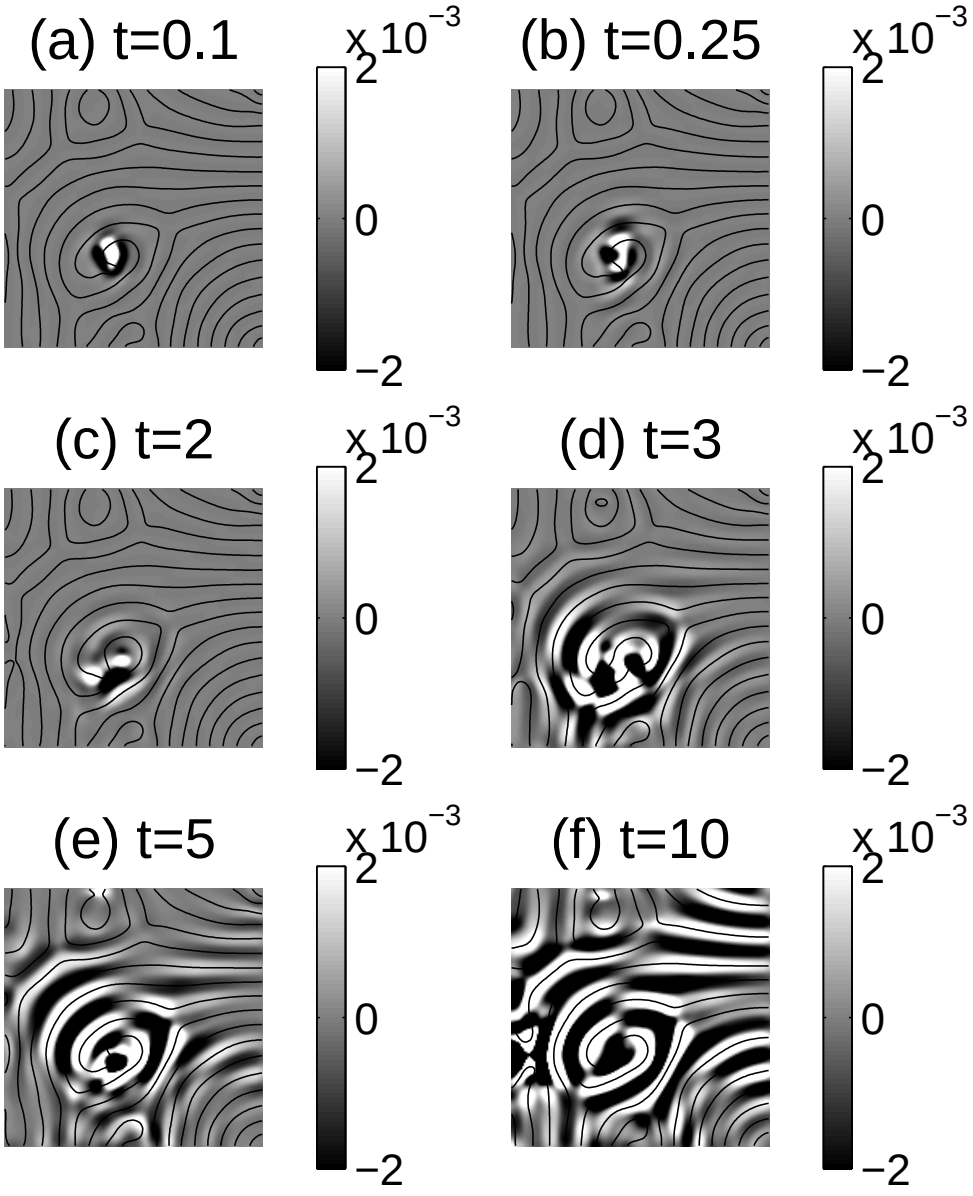

Figure 5.5: Evolution of the temperature perturbation field $\psi(x, y, z = 0, t)$ in spiral defect chaos for various times t. Note that only the bottom right quarter of the whole convection planform is shown. The reduced Rayleigh number is $\epsilon = 1.0$ and the Prandtl number $\sigma = 1$. Black and white colors denote negative and positive perturbations, respectively.

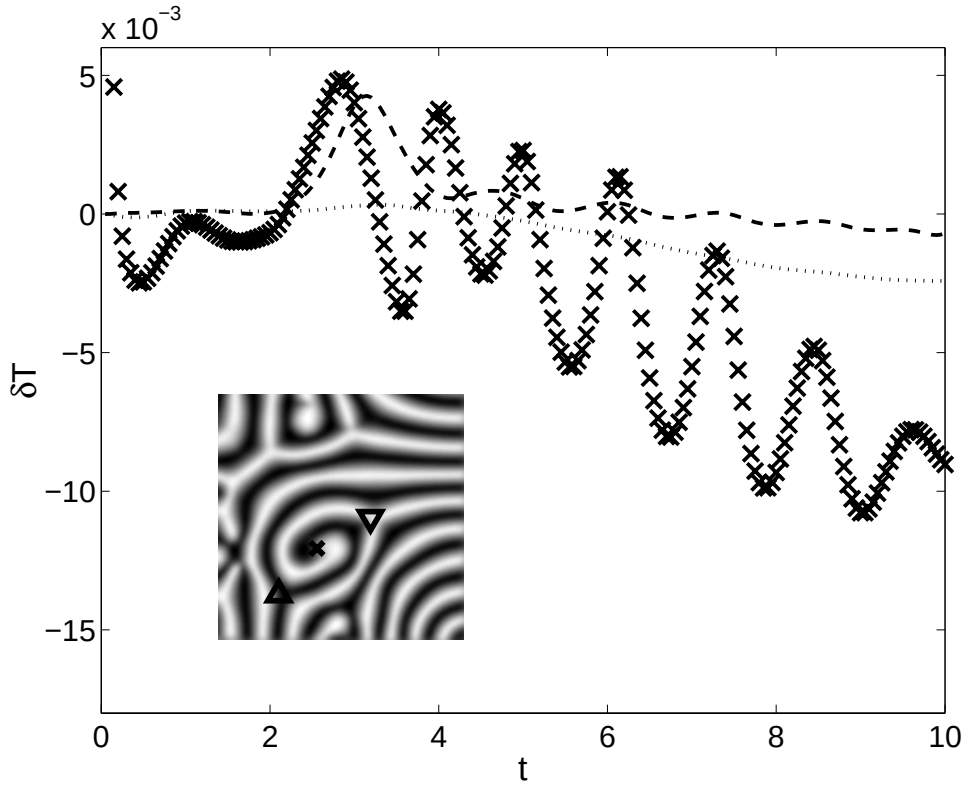

Figure 5.6: Thermal perturbations vs. time t at the spiral core (crosses) and at two other locations near to the spiral core (up-pointing triangle and dotted line, and down-pointing triangle and dashed line).

can still be understood in terms of the diffusion of the phase variable.

The idea of phase diffusion is as follows. Consider a set of ideal straight and parallel convection rolls near threshold. They can then be described by the state

$$A(x) = A\exp(ikx) \tag{5.10}$$

for some amplitude A and some wave number k. Now, consider a small perturbation to the state $A(x)$,

$$A(x) = (A + \delta A)\exp(ikx + i\delta\phi) \tag{5.11}$$

with δA and $\delta\phi$ being perturbations in the amplitude variable A and the phase variable ϕ, respectively. Substituting Eq. (5.11) into the amplitude equation [27] valid near

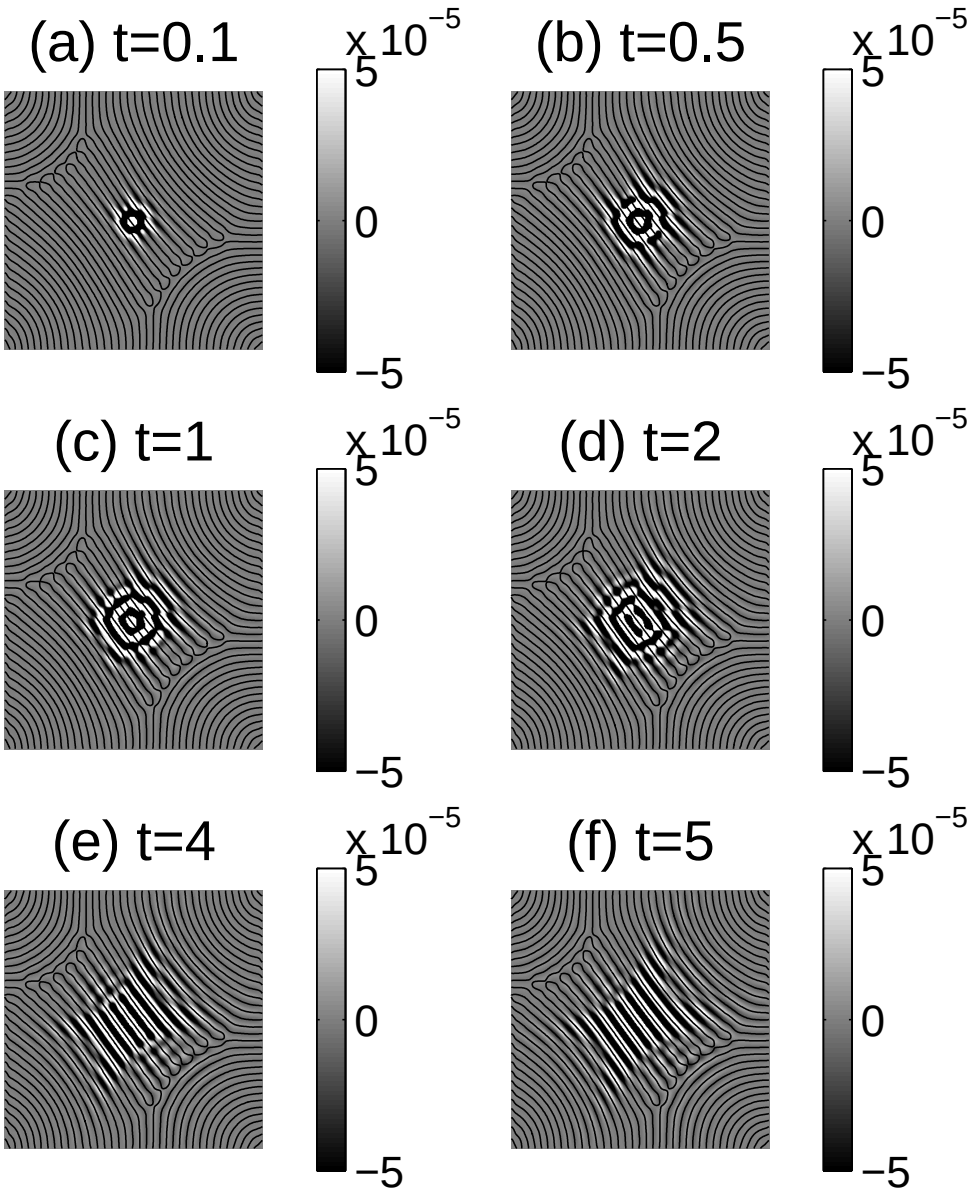

Figure 5.7: Evolution of the temperature perturbation field $\psi(x, y, z = 0, t)$ for various times t.

threshold then yields the phase diffusion equation [71],

$$\partial_t \delta\phi = D_\parallel(k)\partial_{xx}\delta\phi + D_\perp(k)\partial_{yy}\delta\phi, \tag{5.12}$$

where the diffusivities $D_\parallel$ and $D_\perp$ are functions of the reduced Rayleigh number ϵ and wave number k,

$$D_\parallel = \frac{\xi_0^2}{\tau_0}\frac{\epsilon - 3\xi_0^2 k^2}{\epsilon - \xi_0^2 k^2}, \tag{5.13}$$

and

$$D_\perp = \frac{\xi_0^2}{\tau_0} k k_c, \tag{5.14}$$

with constants $\xi_0^2 = 0.148$, $\tau_0^{-1} = 19.65\sigma/(\sigma + 0.5117)$, and $k_c = 3.117$ the critical wave number at the onset of convection in an infinite domain [27].

In Fig. 5.8, the mean square displacement $V(t)$ of the spreading thermal perturbation field is computed and plotted using Eq. (4.8) of the previous chapter. A least squares fit to the power law $\sim t^\gamma$ yields an exponent $\gamma = 1$, suggesting that the perturbations are spreading by normal diffusion. To verify that this diffusion is indeed the phase diffusion, the displacements corresponding to diffusion with diffusivities corresponding to both parallel and perpendicular diffusion are plotted (dashed and dash-dotted lines, respectively). It can be seen that the mean square displacement $V(t)$ for the temperature perturbation field is well described by diffusion with an effective diffusivity that is the average of the two phase diffusivities, $(D_\parallel + D_\perp)/2$.

5.4 Conclusions

In this chapter, the propagation of perturbations is studied in two scenarios, in spiral defect chaos and in pre-chaotic stripe textures. In the former case, the defects are found to be nucleation centers for the perturbations. In addition, an oscillatory core instability is discovered. In the latter case, the propagation is explained in terms of the diffusion of the phase variable of the stripe state. The effective diffusivity is calculated to be the arithmetic mean of the parallel and perpendicular phase diffusivities.

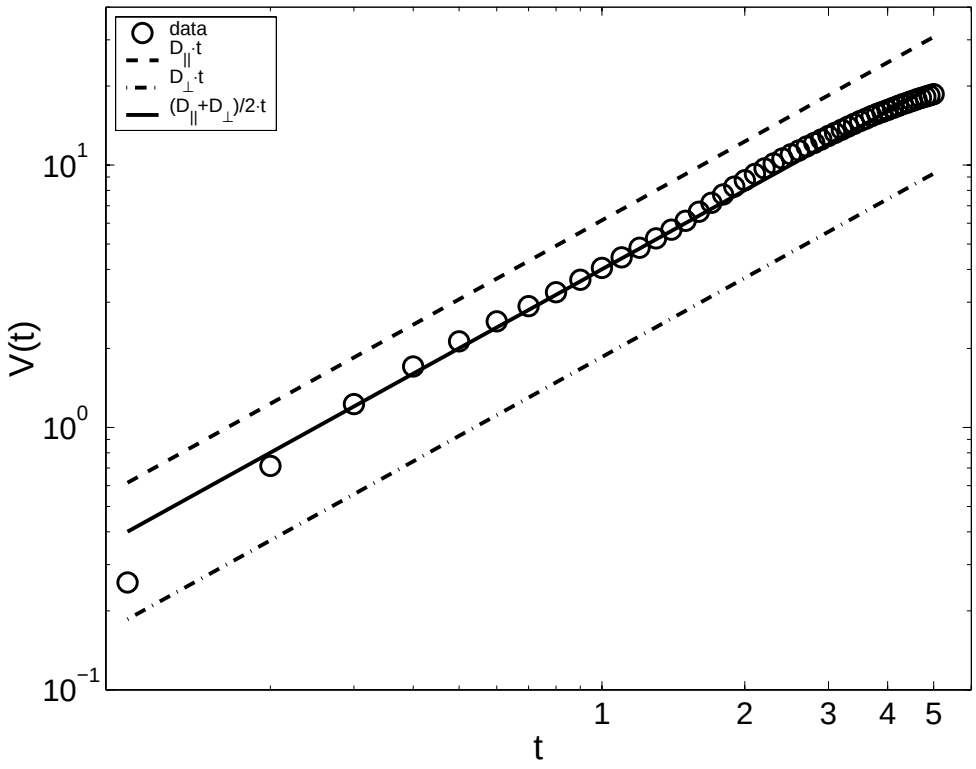

Figure 5.8: Mean square displacement $V(t)$ (circles) of the thermal perturbation field in stripe textures when the reduced Rayleigh number $\epsilon = 0.15$ and the Prandtl number $\sigma = 1$. The mean square displacements corresponding to both parallel and perpendicular diffusion are plotted (dashed and dash-dotted lines, respectively). The solid line is the mean square displacement $V(t)$ with diffusivity that is the average of $D_\parallel$ given by Eq. (5.13) and $D_\perp$ given by Eq. (5.14).

Chapter 6

Conclusions

In summary, three problems that relate to the formation and the dynamics of spatiotemporal chaos, specifically spiral defect chaos, arising in Rayleigh-Bénard convection are investigated in this dissertation.

In Chap. 3, the formation of spiral defect chaos is explained in terms of the generation of the nonlocal mean flow. This is achieved through the construction of a *gedanken* fluid whose velocity field is modified to have zero mean. It is found that, in the absence of the mean flow, spiral defect chaos collapses to a stationary pattern comprising textures of stripes with angular bends. The quenched patterns are shown to have statistical properties that differ from those of spiral defect chaos. For example, the quenched patterns have mean wave numbers that approach those uniquely selected by focus-type singularities, which, in the absence of the mean flow, lie at the zigzag instability boundary. The quenched patterns also have larger correlation lengths and are comprised of rolls with less curvature. In addition, mean flow is also shown to contribute to the commonly observed phenomenon of rolls terminating perpendicularly into lateral walls. In the absence of the mean flow, rolls begin to terminate into lateral walls at an oblique angle. This obliqueness increases with the Rayleigh number.

In Chap. 4, the spreading of a passive tracer concentration in a Rayleigh-Bénard convection flow exhibiting spiral defect chaos is studied. It is found that, in the presence of advection by spiral defect chaos, the spreading can be characterized by normal diffusion. The enhancement in the tracer diffusivity follows two regimes.

When the molecular diffusivity of the tracer concentration is small, the enhancement is proportional to the Péclet number. When the molecular diffusivity is large, the enhancement is proportional to the square root of the Péclet number. This difference is explained in terms of the dependence of the transport on the local wave numbers. It is found that tracer concentrations with small molecular diffusivity experience enhanced longitudinal diffusion and suppressed lateral diffusion at regions of the flow occupied by defects.

In Chap. 5, the propagation of perturbations is studied in two scenarios, in spiral defect chaos and in pre-chaotic stripe textures. In the former case, the defects are found to be nucleation centers for the perturbations. In addition, an oscillatory core instability is discovered. In the latter case, the propagation is explained in terms of the diffusion of the phase variable of the stripe state. The effective diffusivity is calculated to be the arithmetic mean of the parallel and perpendicular phase diffusivities.

Finally, this dissertation focuses almost exclusively on spiral defect chaos as an example for spatiotemporal chaos, and exclusively on Rayleigh-Bénard convection as a model capable for generating and sustaining spatiotemporal chaos. It could have been helpful to study a second instance of spatiotemporal chaos, such as domain chaos that arise in rotating Rayleigh-Bénard convection. Results obtained for spiral defect chaos could then be checked to see if they apply in domain chaos, thus presenting an opportunity to check for universal features. In addition, this dissertation makes use of direct numerical simulations almost exclusively. Unfortunately, the limitations of computing speed and memory means that simulations cannot achieve system sizes as large as those used in experiments. Thus, when performing simulations, one always has to worry about the lack of "clean" statistics. It is hope that advances in computational science, such as the development of grid and cluster computing technologies, will alleviate these problems.

Bibliography

[1] G. Ahlers. Low-temperature studies of the Rayleigh-Bénard instability and turbulence. *Physical Review Letters*, 33:1185–1188, 1974.

[2] G. Ahlers and R. P. Behringer. Evolution of turbulence from the Rayleigh-Bénard instability. *Physical Review Letters*, 40:712–716, 1978.

[3] H. Aref. Stirring by chaotic advection. *Journal of Fluid Mechanics*, 143:1–21, 1983.

[4] S. W. Armfield. Finite difference solutions of the Navier-Stokes equations on staggered and non-staggered grids. *Computers in Fluids*, 29(1):1–17, 1991.

[5] W. Arter and A. C. Newell. Numerical simulation of Rayleigh-Bénard convection in shallow tanks. *Physics of Fluids*, 31:2474–2485, 1988.

[6] M. Assenheimer and V. Steinberg. Rayleigh-Bénard convection near the gas-liquid critical point. *Physical Review Letters*, 70(25):3888–3891, June 1993.

[7] M. Assenheimer and V. Steinberg. Transition between spiral and target states in Rayleigh-Bénard convection. *Nature*, 367:345–347, January 1994.

[8] J. B. Bell, P. Colella, and H. M. Glaz. A second-order projection method for the incompressible Navier-Stokes equations. *Journal of Computational Physics*, 85:257–283, 1989.

[9] P. Bergé. Chaos and turbulence in Rayleigh-Bénard convection. *Physica Scripta*, 40:381, 1989.

[10] E. Bodenschatz, W. Pesch, and G. Ahlers. Recent developments in Rayleigh-Bénard convection. *Annual Review of Fluid Mechanics*, 32:709–778, 2000.

[11] T. Bohr, M. H. Jensen, G. Paladin, and A. Vulpiani. *Dynamical Systems Approach to Turbulence*. Cambridge University Press, Cambridge, 1998.

[12] E. F. F. Botta, K. Dekker, Y. Notay, A. van der Ploeg, C. Vuik, F. W. Wubs, and P. M. de Zeeuw. How fast the Laplace equation was solved in 1995. *Applied Numerical Mathematics*, 24:439–455, 1997.

[13] J. C. Buell. *Wavenumber selection in steady Rayleigh-Bénard convection*. PhD thesis, University of California at Los Angeles, 1986.

[14] J. C. Buell and I. Catton. Wavenumber selection in large-amplitude axisymmetric convection. *Physics of Fluids*, 29:23–30, 1986.

[15] F. H. Busse. Non-linear properties of thermal convection. *Reports on Progress in Physics*, 41:1929, 1978.

[16] R. V. Cakmur, D. A. Egolf, B. B. Plapp, and E. Bodenschatz. Bistability and competition of spatiotemporal chaotic and fixed point attrators in Rayleigh-Bénard convection. *Physical Review Letters*, 79(10):1853–1856, 1997.

[17] R. Camassa and S. Wiggins. Chaotic advection in a Rayleigh-Bénard flow. *Physical Review A*, 43(2):774–797, January 15 1991.

[18] R. Camassa and S. Wiggins. Transport of a passive tracer in time-dependent Rayleigh-Bénard convection. *Physica D*, 51:472–481, August 1991.

[19] S. Chandrasekhar. *Hydrodynamic and Hydromagnetic Stability*. Oxford University Press, Oxford, 1961.

[20] K.-H. Chiam. Nonlinear and scaling behaviors in human electroencephalograms and spontaneously bursting neuronal networks. Senior thesis, University of Michigan (unpublished), 1996.

[21] K.-H. Chiam, M. C. Cross, and H. S. Greenside. Mean flow and spiral defect chaos in Rayleigh-Bénard convection. *Physical Review E*, 67:056206, May 2003.

[22] K.-H. Chiam, M. C. Lai, and H. S. Greenside. Efficient algorithm on a non-staggered mesh for simulating Rayleigh-Bénard convection in a box. Accepted by *Physical Review E*, 2003.

[23] V. Croquette, P. Le Gal, A. Pocheau, and R. Gugliemetti. Large-scale flow characterization in a Rayleigh-Bénard convective pattern. *Europhysics Letters*, 1(8):393–399, April 15 1986.

[24] M. C. Cross. Boundary-conditions on the envelope function of convective rolls close to onset. *Physics of Fluids*, 25(6):936–941, 1982.

[25] M. C. Cross. Phase dynamics of convective rolls. *Physical Review A*, 27:490–498, 1983.

[26] M. C. Cross. Theoretical modelling of spiral chaos in Rayleigh-Bénard convection. *Physica D*, 97:65–80, 1996.

[27] M. C. Cross and P. C. Hohenberg. Pattern formation outside of equilibrium. *Review of Modern Physics*, 65(3):851–1112, July 1993.

[28] M. C. Cross and P. C. Hohenberg. Spatiotemporal chaos. *Science*, 263(5153):1569–1570, March 18 1994.

[29] M. C. Cross and A. Newell. Convection patterns in large aspect ratio systems. *Physica D*, 10:299–328, 1984.

[30] W. Decker, W. Pesch, and A. Weber. Spiral defect chaos in Rayleigh-Bénard convection. *Physical Review Letters*, 73(5):648–651, 1994.

[31] R. E. Ecke. Spiral defect chaos in Rayleigh-Bénard convection: defect populatoin statistics. *Physica A*, 239:174–188, 1997.

[32] R. E. Ecke, Y. Hu, R. Mainieri, and G. Ahlers. Excitation of spirals and chiral symmetry breaking in Rayleigh-Bénard convection. *Science*, 269:1704–1707, 1995.

[33] D. A. Egolf, I. V. Melnikov, and E. Bodenschatz. Importance of local pattern properties in spiral defect chaos. *Physical Review Letters*, 80(15):3228–3231, 1998.

[34] D. A. Egolf, I. V. Melnikov, W. Pesch, and R. E. Ecke. Mechanisms of extensive spatiotemporal chaos in Rayleigh-Bénard convection. *Nature*, 404(6779):733–736, April 13 2000.

[35] P. F. Fischer. An overlapping Schwarz method for spectral element solution of the incompressible Navier-Stokes equations. *Journal of Computational Physics*, 133(1):84–101, May 1997.

[36] P. F. Fischer and J. S. Mullen. Filter-based stabilization of spectral element methods. *Comptes Rendus de l'Académie des Sciences Paris, Série I, Analyse Numérique*, 332:265–270, 2001.

[37] C. A. J. Fletcher. *Computational Techniques for Fluid Dynamics*, volume I of *Springer Series in Computational Physics*. Springer-Verlag, Berlin, second edition, 1991.

[38] A. V. Getling. *Rayleigh-Bénard Convection: Structures and Dynamics*. World Scientific, Singapore, 1998.

[39] J. P. Gollub and M. C. Cross. Nonlinear dynamics: Chaos in space and time. *Nature*, 404(6779):710–711, April 13 2000.

[40] P. Grassberger. Information content and predictability of lumped and distributed dynamical systems. *Physica Scripta*, 40:346, 1989.

[41] H. S. Greenside, M. C. Cross, and W. M. Coughran, Jr. Mean flows and the onset of chaos in large-cell convection. *Physical Review Letters*, 60:2269–2272, 1988.

[42] R. O. Grigoriev. *Symmetry and Localized Control of Extended Chaotic Systems*. PhD thesis, California Institute of Technology, 1999.

[43] P. C. Hohenberg and B. I. Shraiman. Chaotic behavior of an extended system. *Physica D*, 37:109–115, July 1989.

[44] Y. Hu, R. Ecke, and G. Ahlers. Convection for Prandtl numbers near 1: dynamics of textured patterns. *Physical Review E*, 51(4):3263–3279, 1995.

[45] Y. Hu, R. E. Ecke, and G. Ahlers. Transition to spiral-defect chaos in low Prandtl number convection. *Physical Review Letters*, 74(3):394, 1995.

[46] M. C. Lai, K.-H. Chiam, M. C. Cross, and H. S. Greenside. Simulating complex dynamics in intermediate and large-aspect-ratio convection systems. In *18th Symposium on Energy Engineering Sciences*. Argonne National Laboratory, 2000. Preprint available at `http://arXiv.org/nlin.PS/000508`.

[47] X.-J. Li, H.-W. Xi, and J. D. Gunton. Nature of roll to spiral defect chaos transition. *Physical Review E*, 57:1705–1716, February 1998.

[48] J. Liu and G. Ahlers. Spiral-defect chaos in Rayleigh-Bénard convection with small Prandtl numbers. *Physical Review Letters*, 77(15):3126–3129, 1996.

[49] John Z. Lou and Robert Ferraro. A parallel incompressible flow solver package with a parallel multigrid elliptic kernel. *Journal of Computational Physics*, 125:225–243, 1996.

[50] M. Louie. *Numerical Study of Pattern Forming Processes in Models of Rotating Rayleigh-Bénard Convection*. PhD thesis, California Institute of Technology, 2001.

[51] Y. Maday, A. T. Patera, and E. M. Rønquist. An operator-integration-factor splitting method for time-dependent problems: Application to incompressible fluid flow. *Journal of Scientific Computing*, 5(4):310–337, 1990.

[52] P. Manneville. *Dissipative Structures and Weak Turbulence*. Academic Press, Boston, MA, 1990.

[53] P. McCarty and W. Horsthemke. Effective diffusion coefficient for steady two-dimensional convective flow. *Physical Review A*, 37:2112, 1988.

[54] D. W. McLaughlin, G. C. Papanicolaou, and O. R. Pironneau. Convection of microstructure and related problems. *SIAM Journal on Applied Mathematics*, 45:780, 1985.

[55] A. Monin and A. Yaglom. *Statistical Fluid Mechanics*. MIT Press, Cambridge, MA, 1977.

[56] S. W. Morris, E. Bodenschatz, D. S. Cannell, and G. Ahlers. Spiral defect chaos in large aspect ratio Rayleigh-Bénard convection. *Physical Review Letters*, 71(13):2026–2029, September 27 1993.

[57] S. W. Morris, E. Bodenschatz, D. S. Cannell, and G. Ahlers. The spatiotemporal structure of spiral defect chaos. *Physica D*, 97:164–179, 1996.

[58] A. C. Newell, T. Passot, and M. Souli. Convection at finite Rayleigh numbers in large-aspect-ratio containers. *Physical Review Letters*, 64(20):2378–2381, 1990.

[59] A. C. Newell, T. Passot, and M. Souli. The phase diffusion and mean drift equations for convection at finite Rayleigh numbers in large containers. *Journal of Fluid Mechanics*, 220:187–252, 1990.

[60] E. Ott. *Chaos in Dynamical Systems*. Cambridge University Press, Cambridge, 1993.

[61] R. K. Pathria. *Statistical Mechanics*. Butterworth-Heinemann, Oxford, 1996.

[62] D. J. Patil, B. R. Hunt, E. Kalnay, J. A. Yorke, and E. Ott. Local low dimensionality of atmospheric dynamics. *Physical Review Letters*, 86(26):5878–5881, June 25 2001.

[63] M. R. Paul, K.-H. Chiam, M. C. Cross, P. F. Fischer, and H. S. Greenside. Pattern formation and dynamics in Rayleigh-Bénard convection: Numerical simulations of experimentally realistic geometries. Accepted by *Physica D*, 2003.

[64] M. R. Paul, M. C. Cross, and P. F. Fischer. Power-law behavior of power spectra in low Prandtl number Rayleigh-Bénard convection. *Physical Review Letters*, 87(15):154501, October 2001.

[65] M. R. Paul, M. C. Cross, and P. F. Fischer. Rayleigh-Bénard convection with a radial ramp in plate separation. *Physical Review E*, 66(4):046210, October 2002.

[66] M. Perić, R. Kessler, and G. Scheuerer. Comparison of finite–volume numerical methods with staggered and colocated grids. *Computers and Fluids*, 16:389–403, 1988.

[67] B. Pesaran. *Analysis of Neuronal Dynamics in Behaving Animals*. PhD thesis, California Institute of Technology, 2002.

[68] W. Pesch. Complex spatiotemporal convection patterns. *Chaos*, 6(3):348–357, 1996.

[69] A. Pocheau and V. Croquette. Dislocation motion: a wavenumber selection mechanism in Rayleigh-Bénard convection. *Journal de Physique*, 45:35–48, 1984.

[70] A. Pocheau, V. Croquette, P. Le Gal, and C. Poitu. Convective pattern deformations under mean flow-stress. *Europhysics Letters*, 3(8):915–920, April 15 1987.

[71] Y. Pomeau and P. Manneville. Stability and fluctuations of a spatially periodic convective flow. *Journal of Physics Letters*, 40:L–609, 1979.

[72] R. Ramshankar, D. Berlin, and J. P. Gollub. Transport by capillary waves. Part I. Particle trajectories. *Physics of Fluids A*, 2(11):1955–1965, November 1990.

[73] R. Ramshankar and J. P. Gollub. Transport by capillary waves. Part II. Scalar dispersion and structure of the concentration field. *Physics of Fluids A*, 3(5):1344–1350, May 1991.

[74] M. N. Rosenbluth, H. L. Berk, I. Doxas, and W. Horton. Effective diffusion in laminar convective flows. *Physics of Fluids*, 30:2636, 1987.

[75] M. Schatz. Private communication. 2003.

[76] R. Schmitz, W. Pesch, and W. Zimmermann. Spiral defect chaos: Swift-Hohenberg model versus Boussinesq equations. *Physical Review E*, 65(3):037302, March 2002.

[77] S. K. Scott. *Chemical Chaos*. Oxford University Press, Oxford, 1993.

[78] S. Setayeshgar. *Turing Pattern Formation in the Chlorine Dioxide-Iodine-Malonic Acid Reaction-Diffusion System*. PhD thesis, California Institute of Technology, 1998.

[79] M. F. Shlesinger, G. M. Zaslavsky, and U. Frisch, editors. *Lévy Flights and Related Topics in Physics*. Springer, 1995.

[80] B. I. Shraiman. Diffusive transport in a Rayleigh-Bénard convection cell. *Physical Review A*, 36(1):261–267, July 1987.

[81] B. I. Shraiman and E. D. Siggia. Scalar turbulence. *Nature*, 405(6787):639–646, June 8 2000.

[82] E. D. Siggia and A. Zippelius. Pattern selection in Rayleigh-Bénard convection near threshold. *Physical Review Letters*, 47:835–838, 1981.

[83] T. H. Solomon and J. P. Gollub. Chaotic particle transport in time-dependent Rayleigh-Bénard convection. *Physical Review A*, 38:6280, 1988.

[84] T. H. Solomon and J. P. Gollub. Passive transport in steady Rayleigh-Bénard convection. *Physics of Fluids*, 31(6):1372–1379, June 1988.

[85] T. H. Solomon, E. R. Weeks, and H. L. Swinney. Observation of anomalous diffusion and Lévy flights in a two-dimensional rotating flow. *Physical Review Letters*, 71(24):3975–3978, December 1993.

[86] T. H. Solomon, E. R. Weeks, and H. L. Swinney. Chaotic advection in a 2-dimensional flow - Lévy flights and anomalous diffusion. *Physica D*, 76:70–84, 1994.

[87] S. H. Strogatz. *Nonlinear Dynamics and Chaos*. Addison-Wesley, Reading, MA, 1994.

[88] P. Swarztrauber and R. Sweet. Efficient FORTRAN subprograms for the solution of elliptic partial differential equations. Technical report, NCAR, 1975.

[89] P. N. Swarztrauber and Roland A. Sweet. The direct solution of the discrete Poisson equation on a disk. *SIAM Journal on Numerical Analysis*, 10(5):900–907, 1973.

[90] J. Swift and P. C. Hohenberg. Hydrodynamic fluctuations at the convective instability. *Physical Review A*, 15:319–328, 1977.

[91] W. Y. Tam and H. L. Swinney. Mass transport in turbulent Couette-Taylor flow. *Physical Review A*, 36(3):1374–1381, 1987.

[92] J. C. Tannehill, D. A. Anderson, and R. H. Pletcher. *Computational Fluid Mechanics and Heat Transfer*. Taylor and Francis, New York, second edition, 1997.

[93] H. Tomita and K. Abe. Numerical simulation of the Rayleigh-Beénard convection of air in a box of large aspect ratio. *Physics of Fluids*, 11(3):743–745, 1999.

[94] L. S. Tsimring. Spiral dynamics in pattern-forming systems: mean-flow effects. *Physica A*, 249:125–133, February 1998.

[95] Y. Tu and M. C. Cross. Chaotic domain structure in rotating convection. *Physical Review Letters*, 69(17):2515–2518, October 1992.

[96] H. M. Tufo and P. F. Fischer. Terascale spectral element algorithms and implementations. In *Proceedings of the ACM/IEEE SC99 Conference on High Performance Networking and Computing*. IEEE Computer Society, 1999.

[97] A. M. Turing. The chemical basis of morphogenesis. *Philosophical Transactions of the Royal Society B (London)*, 237:37–72, 1952.

[98] W. van der Water and T. Bohr. Critical properties of lattices of diffusively coupled quadratic maps. *Chaos*, 3(4):747–756, 1993.

[99] J. A. Vastano and H. L. Swinney. Information transport in spatiotemporal systems. *Physical Review Letters*, 60(18):1773–1776, May 1988.

[100] J. Wesfreid, Y. Pomeau, M. Dubois, C. Normand, and P. Bergé. Critical effects in Rayleigh-Bénard convection. *Journal de Physique*, 1978.

[101] H.-W. Xi and J. D. Gunton. Spatiotemporal chaos in a model of Rayleigh-Bénard convection. *Physical Review E*, 52(5):4963–4975, 1995.

[102] H.-W. Xi, J. D. Gunton, and J. Viñals. Spiral defect chaos in a model of Rayleigh-Bénard convection. *Physical Review Letters*, 71(13):2030–2033, 1993.

[103] H.-W. Xi, X.-J. Li, and J. D. Gunton. Direct transition to spatiotemporal chaos in low Prandtl number fluids. *Physical Review Letters*, 78(6):1046–1049, 1997.